

AD-A119 066

NAVAL RESEARCH LAB WASHINGTON DC
PROCEEDINGS OF THE FIRST WORKSHOP ON NONDESTRUCTIVE EVALUATION --ETC(U)
JUN 82 O P ARORA, H H CHASKELIS, N K BATRA

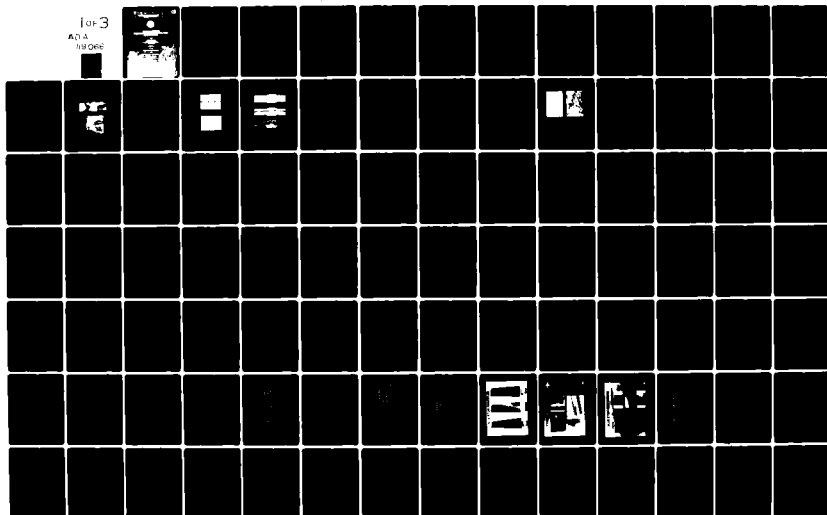
F78 11/6

UNCLASSIFIED

DTNSRDC/SME-CR-14-82

NL

1 of 3
AD-A
NUMBER



AD A110-116

SECURITY CLASSIFICATION OF THIS PAGE (When Data Entered)

REPORT DOCUMENTATION PAGE		READ INSTRUCTIONS BEFORE COMPLETING FORM
1. REPORT NUMBER DTNSRDC-SME-CR-14-82	2. GOVT ACCESSION NO. AD-A119066	3. RECIPIENT'S CATALOG NUMBER
4. TITLE (and Subtitle) PROCEEDINGS OF THE FIRST WORKSHOP ON NONDESTRUCTIVE EVALUATION (NDE) OF TITANIUM ALLOYS		5. TYPE OF REPORT & PERIOD COVERED Proceedings
7. AUTHOR(s) O. P. Arora, H. H. Chaskelis, and N. K. Batra		6. PERFORMING ORG. REPORT NUMBER
9. PERFORMING ORGANIZATION NAME AND ADDRESS Naval Research Laboratory Washington, DC 20375		8. CONTRACT OR GRANT NUMBER(s)
11. CONTROLLING OFFICE NAME AND ADDRESS Office of Naval Research Arlington, Virginia 22217		10. PROGRAM ELEMENT, PROJECT, TASK AREA & WORK UNIT NUMBERS Element# 61153-N-RR-022- 01-01-1AF Work# 58-1272-01
14. MONITORING AGENCY NAME & ADDRESS (if different from Controlling Office) David W. Taylor Naval Ship Research and Development Center Annapolis, MD 21402		12. REPORT DATE June 1982
		13. NUMBER OF PAGES 234
		15. SECURITY CLASS. (of this report) UNCLASSIFIED
		15a. DECLASSIFICATION/DOWNGRADING SCHEDULE
16. DISTRIBUTION STATEMENT (of this Report) Approved for public release; distribution unlimited.		
17. DISTRIBUTION STATEMENT (of the abstract entered in Block 20, if different from Report)		
18. SUPPLEMENTARY NOTES		
19. KEY WORDS (Continue on reverse side if necessary and identify by block number) NDE Titanium Ultrasonics Welds		
20. ABSTRACT (Continue on reverse side if necessary and identify by block number) These proceedings cover briefly some of the state-of-the-art NDE techniques which may have potential applications to characterization of the Titanium Alloys and Weldments for oxygen contaminations. Most of the potentially applicable techniques covered are ultrasonics techniques, though there is some discussion of other techniques such as acoustic emission, x-rays, photoacoustic microscopy and computed tomography. There is also some discussion of signal-processing techniques which may be useful for characterization of oxygen-contaminated Ti.		

DD FORM 1 JAN 73 1473

EDITION OF 1 NOV 65 IS OBSOLETE
S/N 0102-014-6601

SECURITY CLASSIFICATION OF THIS PAGE (When Data Entered)

CONTENTS

	PAGE
PREFACE	v
1. Ultrasonic Elasticity Measurements of Titanium Welds and Plate G.V. Blessing	1
2. Titanium Alloy Acoustic Data Sanford R. Buxbaum and Robert E. Green, Jr.	15
3. Detection of Interstitial Gas By Internal Friction and Modulus Methods B.R. Tittmann	37
4. Methods For Determining Interstitial Oxygen In Titanium Alloys --- Transparency Synopsis J.M. LaGrotta	69
5. Defect Characterization In Titanium Alloy Using Ultrasonic Spectroscopy Laszlo Adler and Dale Fitting	81
6. Nondestructive Evaluation of Bulk Residual Stresses Using Ultrasonic Techniques Kamel Salama	99
7. Assessment of Weld Quality Using Acoustic Emission And Phase-Sensitive Ultrasonic Methods -- Transparency Synopsis Richard S. Williams	107
8. In-Process Weld Monitoring By Acoustic Emission and Infrared Imaging W. Lichodziejewski	127
9. Photoacoustic Microscopy R.L. Thomas, L.D. Favro, P.K. Kuo, L.I. Inglehart and J.J. Pouch	149
10. Computed Tomography For Inspection Of Industrial Objects Richard Kruger	161
11. Random Signal Correlation And Split - Spectrum Processing E.S. Furgason, N.M. Bilgutay, B.B. Lee and V.L. Newhouse	169
12. ALN 4000 Ultrasonic Pipe Inspection System Anthony N. Mucciardi	191
13. Attendees and Distribution List	227

PREFACE

A workshop was held on 9-10 December 1980 in Orlando, Florida to acquaint interested NDE scientists with the nature and magnitude of problems associated with the Nondestructive Evaluation of Titanium weldments, related to defects and interstitial gas contamination. The workshop was attended by approximately forty-five professionals representing various industries, universities, research organization and Government agencies. The proceedings consist of edited transcripts of most of the papers presented at the workshop. It provides a basis for NDE technology which may be applicable to characterizing defects and contaminations in Titanium Alloys.

A second workshop was held on 2-4 February 1982 in Orlando, Florida to assess the results of several studies aimed at detecting oxygen contamination in Ti weldments and plate samples. The proceedings of this workshop will be published at a later date.

We wish to thank the participants and especially the authors for providing the manuscripts. Special appreciation is given to Dr. Vincent A. Del Grosso and Mr. Henry H. Chaskelis for organizing these workshops and Dr. Hans Vanderveldt for his continued interest and interaction in this area.

Bruce MacDonald
Om Arora



Accession For	
NTIS GRA&I	<input checked="checked" type="checkbox"/>
DTIC TAB	<input type="checkbox"/>
Unannounced	<input type="checkbox"/>
Justification	
By	
Distribution/	
Availability Codes	
Avail and/or	
Dist	Special

A

ULTRASONIC ELASTICITY MEASUREMENTS OF TITANIUM WELDS AND PLATE

G. V. Blessing

*Ultrasonic Standards Group
National Bureau of Sids.
Washington, D.C.*

Ultrasonic shear and longitudinal waves are used to evaluate the material properties of titanium weld and plate alloy. Wave speeds are used to measure the materials' elasticity and anisotropy, and the wave amplitude is used to measure relative levels of scattering in the weld and plate regions. Results obtained on a "good" or representative weld are compared with oxygen contaminated specimens.

INTRODUCTION

Titanium (Ti) alloy weldments are subject to interstitial gas contamination during fabrication, which adversely affects their mechanical properties and in turn degrades structural performance. While the contamination levels which cause a problem are not well established, a need definitely exists to nondestructively detect small quantities of interstitial gas. This report presents the initial results obtained in an attempt to relate the elasticity of Ti 6211^a alloy weldments measured ultrasonically to varying degrees of sample contamination. Baseline elasticity data was obtained on "good" or representative weld and plate material, as was the relative scattering amplitude of the ultrasonic waves. Feasibility for this approach has been demonstrated by other researchers [1,2].

EXPERIMENTAL

Samples

Ultrasonic shear and longitudinal velocity measurements were made on seven oxygen (O) contaminated weld specimens, on an uncontaminated weld, and on plate material. The seven double-Vee butt welds were fatigue crack test specimens, fabricated with varying contamination levels by intermittent atmospheric exposure of the weldments. By this process, a concentration of interstitial O is expected at the surface of the approximately dozen weld beads in a given weldment. Relative contamination levels were judged in-situ by the bead coloration upon exposure. Subsequent metallurgical examination by both bulk chemical analysis and surface microprobe techniques revealed a limited correlation of O level with sample coloration ■■■.

^aTi 6211 is an alpha stabilized alloy with 6Al-2Nb-1Ta-0.8Mo percent atomic weights.

Table I compare O content data for the raw material, and for the series of four attempted levels of contamination. The bulk chemical analyses indicate an expected, consistently larger O content in the welds as compared to the raw material, with a contamination range approaching 500 ppm. The surface microprobe measurements, on the other hand, indicate a very limited increase in O, and for only two of the weld series.

TABLE I

Table I Oxygen Content in Ti 6211 Alloy for Raw Material and Four Weldment Series. Numerical Values are ppm by weight [REDACTED].

Material	Bulk Chemical Analysis	Surface Nuclear Microprobe	Coloration Judgment
Base Plate	700	803	---
Weld Wire	730	---	---
Weld Series 1	860	783	Straw
2	780	770	Yellow-Blue
3	980	860	Blue
4	1190	915	Gray

The seven specimens for ultrasonic measurements, taken from the four weld series, were machined flat in the weld region. The specimens were fatigued prior to their ultrasonic evaluation. However, in most cases the cracks were located at the plate-weld boundary, and in no case were they judged to interfere with the velocity measurements. A cross section of the uncontaminated weld, of larger dimensions than the contaminated specimens but otherwise the same double-Vee fabrication, is shown in Fig. 1. The 1, 2, and 3 directions respectively identify the bead, the in-plane normal to the bead, and the plate normal directions. A large component of epitaxial grain growth in the 3 direction may be observed across the bead boundaries. After etching, the weld bead heat affected zones, caused by partial melting of the previous weld line during successive passes, appear as white cusps due to their contrasting phase structure. This weld region was subsequently cut from the specimen, and machined parallel and flat for the ultrasonic velocity measurements. A dry density measurement yielded a value of 4.46 gm/cm^3 , in reasonable agreement with 4.44 gm/cm^3 calculated from the atomic weight percentages of alloy constituents.

Ultrasonic Technique

Longitudinal and shear wave velocities were obtained from time-of-flight measurements using the pulse echo overlap technique illustrated in Fig. 2. A resolution of one part in 10^4 for delta time exceeded the sample dimensional uniformity, and allowed for velocity measurements with a nominal precision of $\pm 0.1\%$ for longitudinal waves, and $\pm 0.2\%$ for shear waves. In general, several measurements were made across a given specimen geometry to evaluate material homogeneity. The longitudinal measurements were made by immersion using a 25 mm water path length, and the shear by direct contact using a high viscosity couplant. The longitudinal waveform was a 3 to 4 cycle tuned pulse at 10 MHz, and the shear a 1-1/2 cycle broadband pulse at 5 MHz. Both transducer elements were ceramic, the longitudinal of diameter 6mm and the shear 13mm.

RESULTS

First, a detailed evaluation of longitudinal and shear wave velocities in the uncontaminated weld will be presented. This will be followed by the velocities obtained on the plate and two reference materials for alloy comparison and system calibration, and then on the series of contaminated welds. Finally, signal amplitude scans (C-scans) of the uncontaminated weld and plate sample will be presented.

Uncontaminated Weld

Table II summarizes the velocity results for the uncontaminated or representative weld with wave propagation k in the three principal directions defined in Fig. 1. The first data column presents the longitudinal velocity $\langle V_L \rangle_n$ averaged across the sample, where n is the number of measurements made. The second column is the percent variation observed for each propagation direction as the 6mm diameter transducer was discretely scanned across the sample surface. Two values of (extremum) shear velocities $\langle V_S \rangle_n$ are given as a function of k in the next column, corresponding to a particular polarization ϵ or particle displacement. The extremums were observed to occur for ϵ parallel to the respective principal directions, indicating a (not unexpected) material symmetry in those directions. The last column gives the percent elastic anisotropy determined from the ratio of the shear moduli^b for each propagation direction. While V_S was not measured at different positions across the sample surface, one would expect the percent variation to be comparable or greater than that observed for V_L . In fact, the repeatability of the V_S measurement was itself limited to $\pm 0.5\%$ in some instances, showing a sensitivity to both repeat positioning and polarization orientation.

^bShear Modulus = Density $\times V_S^2$

TABLE II

Table II Ultrasonic Velocity Data (in mm/ μ s) as a Function of Propagation Direction \underline{k} and Polarization $\underline{\epsilon}$ for the Uncontaminated Weld.

\underline{k}	V_L	% Variation	$V_S (\underline{\epsilon})$	% Anisotropy
$\underline{1}$	$\langle 6.150 \rangle_6$	0.08	$\langle 3.168 \rangle_2 (\underline{2})$ $\langle 3.200 \rangle_2 (\underline{3})$	2
$\underline{2}$	$\langle 6.158 \rangle_4$	0.15	$\langle 3.168 \rangle_4 (\underline{1})$ $\langle 3.173 \rangle_4 (\underline{3})$	1/3
$\underline{3}$	$\langle 6.153 \rangle_6$	0.05	$\langle 3.183 \rangle_3 (\underline{1})$ $\langle 3.174 \rangle_3 (\underline{2})$	1/2

The large velocity variations for propagation in a given direction, reflecting material inhomogeneity, prevent us from making a detailed comparison of the elasticity as a function of direction. Qualitatively we can say that the longitudinal velocity, which is dominated by the compressional elasticity, varies little as a function of direction. The shear velocity (and therefore modulus) varies much more, as a function both of propagation and polarization direction, with a maximum anisotropy occurring for \underline{k} parallel to the $\underline{1}$ direction. Much of the shear data can be coherently explained by assuming a unidirectional symmetry model with the direction of maximum stiffness to lie in the $(\underline{1}, \underline{3})$ plane, near to the $\underline{3}$ direction. This assumption for the weld texture is consistent with metallurgical examinations which reveal a large component of epitaxial grain growth in the $\underline{3}$ direction, and with an expected component of dendritic growth along the bead ($\underline{1}$) direction.

Reference Materials

It is of interest to compare the weld elasticity with the raw plate material and with another titanium alloy. The data for Ti 6211 and Ti 6Al4V plate is given in Table III for wave propagation perpendicular to the plane of the plate. In addition, velocity values obtained in a single crystal of X-cut quartz are presented as reference points for system accuracy and subsequent measurement precision. The longitudinal data shows an approximate one percent increase in compressional modulus for the plates compared to the weld. In Ti 6211 both the stiffer shear component and the anisotropy are greater in the plate than in the weld. One plate specimen (attached to weld 16) revealed an anisotropy of 6.5% which illustrates itself by the double-echo pattern of Fig. 3. The separation of the incident shear energy (\underline{k} perpendicular to the rolled plate) into two distinct modes of wave propagation is easily observed, revealing substantial plate texturing. Finally, wave velocities measured parallel to the plane of Ti 6211 plate yielded values comparable to those in Table III.

TABLE III

Table III Ultrasonic Velocity Data (in mm/ μ s) for Wave Propagation Perpendicular to the Plate.

Material	V_L	% Variation	V_S	% Anisotropy
Ti 6211 Plate	$\langle 6.196 \rangle_6$	0.13	$\langle 3.179 \rangle_2 (1)$ $\langle 3.220 \rangle_2 (2)$	2.6
Ti 6Al4V Plate	$\langle 6.191 \rangle_2$	---	3.190 (1) 3.194 (2)	0.2
Quartz X-cut	$\langle 5.752 \rangle_4$	---	3.299 (slow mode)	---

Contaminated Welds

Table IV lists the longitudinal velocities obtained on the seven contaminated welds for wave propagation in the $\underline{3}$ direction. The specimens have two digit descriptors, the first corresponding to the weld series and the second to the particular sample cut from the parent series. While a measurement precision of 0.06% is able to differentiate a relatively low velocity value for specimen 22, the large variations observed within each sample preclude ascribing much significance to that difference. The results were similar for the shear velocities (0.1% measurement precision) given in Table V: no correlation of wave speed with weld series could be observed.

Table IV Ultrasonic Longitudinal Velocities (in mm/ μ s) in Contaminated Welds for \underline{k} Parallel to $\underline{3}$.

Specimen	$\langle V_L \rangle_6$	% Variation
16	6.180	0.5
22	6.167	0.3
24	6.178	0.1
35	6.181	0.2
36	6.180	0.2
45	6.180	0.1
46	6.180	0.2

Table V Ultrasonic Shear Velocities (in mm/us) in Contaminated Welds for k Parallel to 3 and for Polarization Directions 1 and 2.

Specimen#	$V_S(1)$	$V_S(2)$	% Anisotropy
16	3.211	3.193	1.5
22	3.216	3.188	1.0
24	3.214	3.187	1.1
35	3.216	3.192	1.5
36	3.216	3.197	0.9
45	3.215	3.198	0.9
46	3.215	3.190	1.1

Amplitude Scans

In addition to the velocity measurements, a series of pulse-echo backwall reflection scans (C-scans) were made on the reference weld-plate specimen. Wave propagation was in the 1 direction of Fig. 1, which shows cross-sectional view of Ti-6211 weld plates. A 10 MHz transducer focused at 300 mm in water was used for enhanced lateral resolution. Two significant features in the three representative C-scans of Fig. 4 deserve attention. The first is a greater attenuation of ultrasound in the plate than in the weld, which contrasts sharply with the situation commonly observed in austenitic steels. For example, while the plate region has become nearly opaque to ultrasound at the -34 dB gain setting the weld region remains identifiable. The second feature is the large range in signal amplitude for both the plate and weld regions. A total range of about 30 dB from initial ultrasonic penetration to complete transmission was observed at this frequency and sample thickness.

Relative amplitude measurements were also made for wave propagation at discrete positions in the 3 direction. Again the plate was observed to have a much larger attenuation than the weld, by about a factor of two.

CONCLUSIONS

Ultrasonic shear and longitudinal wave velocity measurements on a "good" or representative Ti 6211 weldment revealed an anisotropy due to preferential grain growth, implying an elastic axis of symmetry to lie between the bead direction and a perpendicular to the plane of the welded plates. A comparison with the plate elasticity showed slightly less stiffness (approximately one percent) and a smaller anisotropy. The elastic anisotropy due to texturing in the rolled plate was very noticeable, in one case exceeding six percent.

Perhaps the greatest challenge to the ultrasonic inspection of Ti 6211 alloy is the material variability or inhomogeneity that exists on the scale of ultrasonic wavelengths normally employed. For example, sound speed differences that might be readily detected with available measurement precision, and related to sample contamination levels, were in fact overwhelmed by variations within the samples themselves at 5 and 10 MHz. No correlation of weld sound speed with the limited O contamination levels could be observed for the sample set provided. However, inconsistent contamination level analyses raises a question for sample veracity. One note of encouragement is the observation that the contaminated weld sound speeds were consistently larger than that for the representative or uncontaminated weld. This is expected on the basis of Ti hardening by interstitial O stabilization of the metal's alpha phase. Finally, amplitude measurements by direct contact and immersion C-scan revealed an appreciably greater attenuation in the plate than in the weld for ultrasonic wavelengths on the order of 0.5 mm.

RECOMMENDATIONS

A primary recommendation for future work is to generate a well characterized sample set possessing a large range of contamination levels, especially to include the worst case level. In addition to the approach taken here, the temperature and frequency dependence of ultrasonic wave propagation may be worth pursuing. For example, elevated temperature studies may reveal a greater sensitivity of the sound speed to gaseous contamination as the matrix elasticity is reduced. Secondly, using a lower frequency (larger wavelength) would serve to desensitize the elasticity measurements to the effects of large grains and texturing while remaining sensitive to interstitial gas content.

ACKNOWLEDGEMENT

The author wishes to acknowledge fruitful discussions with Prof. R. E. Green, Jr. of Johns Hopkins University, and Dr. N. N. Hsu of the National Bureau of Standards. This work was supported by the Naval Research Laboratory, Code 5831, Washington, D. C.

REFERENCES

1. N. Hsu and H. Conrad, "Ultrasonic Wave Velocity Measurements on Titanium-Oxygen Alloys", Scripta Metallurgica 5 (1971) pp. 905-908.
2. O. Buck, D. O. Thompson, N. E. Paton, J. C. Williams, "The Relation Between Internal Friction Spectra and the Athermal $\beta \rightarrow \omega$ Transformation in Ti-V, Ti-V-O, and Ti-V-H Alloys" Proc. of the Fifth Intern. Conf. on Internal Friction and Ultrasonic Attenuation in Crystalline Solids, Aachen, Germany, (27-30 Aug. 1973) pp. 451-458.



Fig. 1. Two magnifications of a cross sectional view of a representative Ti 6211 weld-plate sample, etched to reveal epitaxial grain growth across the weld bead boundary and plate texture.

ULTRASONIC SYSTEM

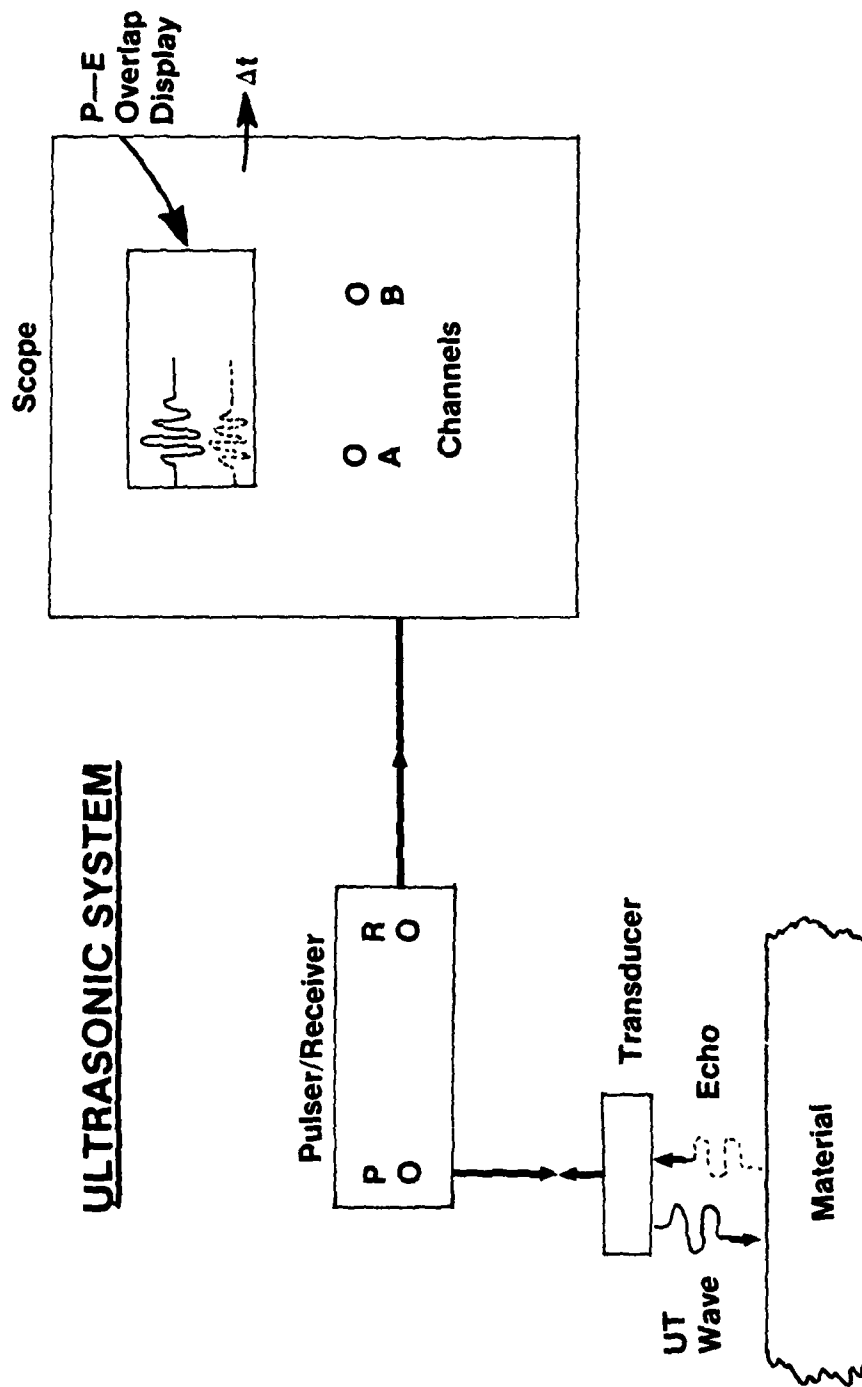


Fig. 2. Ultrasonic velocity measurement system utilizing the pulse echo overlap technique by means of an oscilloscope delta time feature.

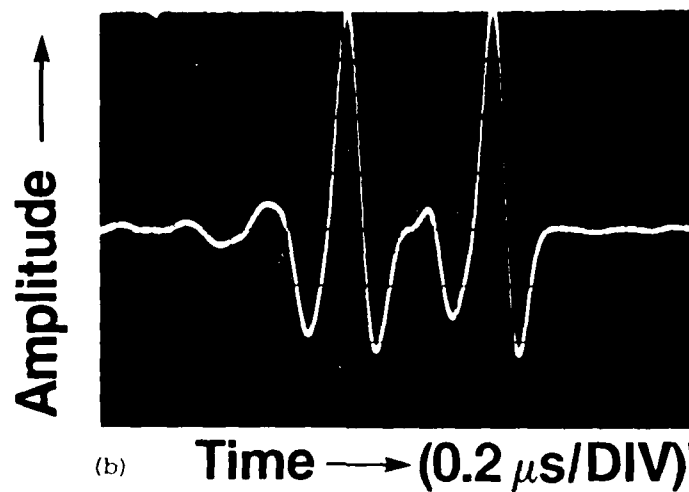
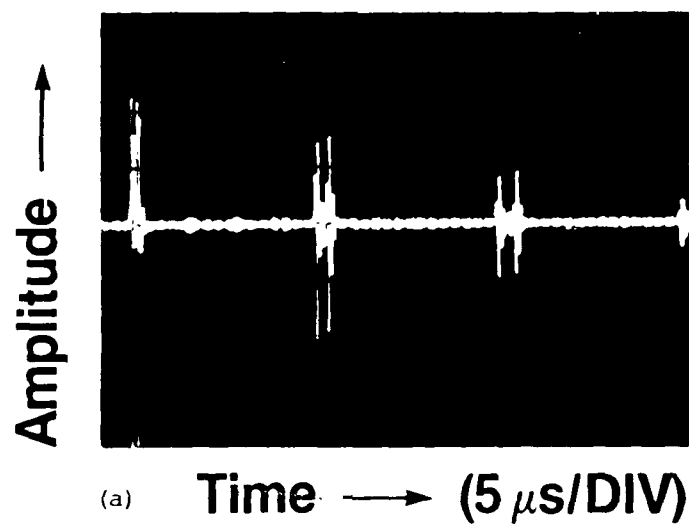


Fig. 3. (a) A double echo train of shear waves caused by texturing in a Ti 6211 plate sample. (b) An expanded view of the first echo pair (inverted).

RELATIVE
GAIN
LEVELS

-12dB



-22dB



-34dB



Fig. 4. A series of C-scans at three discrete gain levels for the weld-plate specimen of Fig. 1, with an outline of the weld region superimposed on the third trace.

TITANIUM ALLOY ACOUSTIC DATA

Sanford R. Buxbaum and Robert E. Green, Jr.

*Materials Science and Engineering Department
The Johns Hopkins University
Baltimore, Maryland 21218*

The use of weldments of titanium alloys in structural applications requires the development of reliable nondestructive methods for inspecting the mechanical integrity of the weld region. Since one of the primary nondestructive inspection techniques is ultrasonics, it is expedient to determine the usefulness and limitations of ultrasonic inspection for these materials. In the present work various ultrasonic tests were conducted on a series of test specimens of titanium alloy weldments and base plate material. Ultrasonic velocity and attenuation measurements were made in the low megahertz frequency range using both longitudinal and shear waves. Both the ultrasonic velocity and attenuation were observed to be lower in the weld region than in the base metal. Changes in the velocity and attenuation were correlated to the microstructural variations in the weld region and base metal. Rockwell hardness measurements were also made across the specimen surfaces and comparison made with the ultrasonic results.

Introduction

The safe in-service use of titanium alloy weldments requires the development of reliable nondestructive methods for inspecting the mechanical integrity of the weld region. Unfortunately, current nondestructive evaluation technology has not proven adequate. Since one of the primary nondestructive inspection techniques is ultrasonics, it is expedient to determine the usefulness and limitations of ultrasonic inspection for the materials in question. In the present work, various ultrasonic tests were conducted in a series of test specimens of titanium alloy weldments and base plate material. Ultrasonic wave velocity and attenuation measurements were made in the low-megahertz frequency range using both longitudinal and shear waves. Elastic moduli were subsequently calculated from the ultrasonic wave velocities and measured densities. Both the ultrasonic wave velocity and attenuation were observed to be lower in the weld region than in the base metal. Information provided by x-ray diffraction analysis helped to account for the observed wave velocity behavior. Changes in the attenuation were correlated to the microstructural variations in the weld region and base metal. Hardness measurements were also performed across the specimen surfaces and comparison made with ultrasonic results.

Metallography

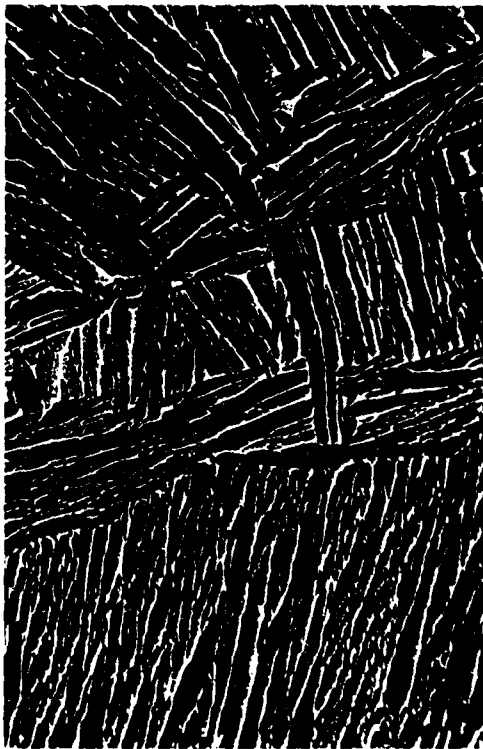
The material used in the present investigation was titanium 6211, which is a near alpha alloy. As-rolled plate of this alloy has high toughness, moderate strength, good weldability, and good resistance to sea water and hot salt corrosion. Metallographic specimens were taken from sections cut from the weld region and from the base metal. After mounting, the specimens were ground on successively finer silicon carbide papers down to 600 grit, and then polished on lapidary wheels using 15 micron and 0.05 micron compounds. A two step etching technique was used to reveal microscopic detail. In the first step the polished specimen was briefly swabbed with a 2 ml HF, 98 ml water solution. This etched the alloy and stained the α phase. The second step, swabbing with a 1 ml HF, 2 ml HNO_3 , 97 ml water solution, removed the stain, leaving a light field of α phase material in which the β phase appeared as finely dispersed dark lines when viewed through an optical microscope.

The microstructures observed in the base plate metal are broken up and show texturing due to rolling. Prior beta phase grain boundaries are decorated by the α phase, because the grain boundaries are the first regions to transform during

cooling. Narrow platelet formations characterize the microstructure of the alpha phase; the remaining β phase is interspersed between the acicular alpha platelets.

The weld region exhibits a very different microstructure from the base plate metal. Acicular alpha and alpha prime (martensitic-type structure) has formed on preferred planes in the prior beta crystals. The alpha platelets are narrower, straighter, and more sharply defined in the weld region than in the base metal. This is probably a result of the faster cooling rates present during welding. The boundaries of the large, equiaxed prior β grains are decorated by alpha metal as in the base plate. Figure 1 illustrates the microstructural differences between weld metal and base metal. The photomicrographs in Figs. 1(a) and 1(b) were taken with the aid of a scanning electron microscope.

Welding plate sections of titanium requires multiple welding passes. A polished and etched cross-section of a typical weld shows the weld passes clearly delineated. The narrow regions of delineation have a microstructure that is different from that of the rest of the weld and the base metal. Typical microstructures of such a region reveal very little detail and appear to be primarily alpha phase with small amounts of beta phase very finely dispersed. The region can easily be followed around a weld bead when the specimen is viewed under a metallographic microscope. It is



(a) Base Metal
Mag = 1000X
10 μ m



(b) Weld Region
Mag = 1000X
10 μ m

Fig. 1. Comparison of Microstructures of Base Metal and Weld Region

suspected that these regions are caused by high localized oxygen content. An alternative explanation could involve the thermal history to which each weld pass was subjected.

Velocity and Attenuation Measurements

The specimens used for ultrasonic examination were fabricated from welded specimens and were representative of the titanium alloy material. Flat, parallel faces were machined on the specimen prior to performing both ultrasonic measurements and hardness measurements. A high degree of parallelism of specimen faces was required to minimize diffraction errors caused by divergence of the ultrasonic pulse as it propagates back and forth through the specimen.

Pulse-echo overlap techniques were used to measure the wave velocities. In the pulse-echo overlap technique, the specimen is pulsed with ultrasound and the subsequent echoes are monitored. The travel time or periodicity between two of these echoes is measured. If successive echoes are chosen, the travel distance is twice the specimen thickness. Hence, one knows the travel distance and the travel period and can calculate the wave velocity. In the system used, shown schematically in Fig. 2, the inverse of the period, or the frequency, was measured.

Referring to Fig. 2, the continuous wave (cw) oscillator provided an adjustable, continuous sync signal,

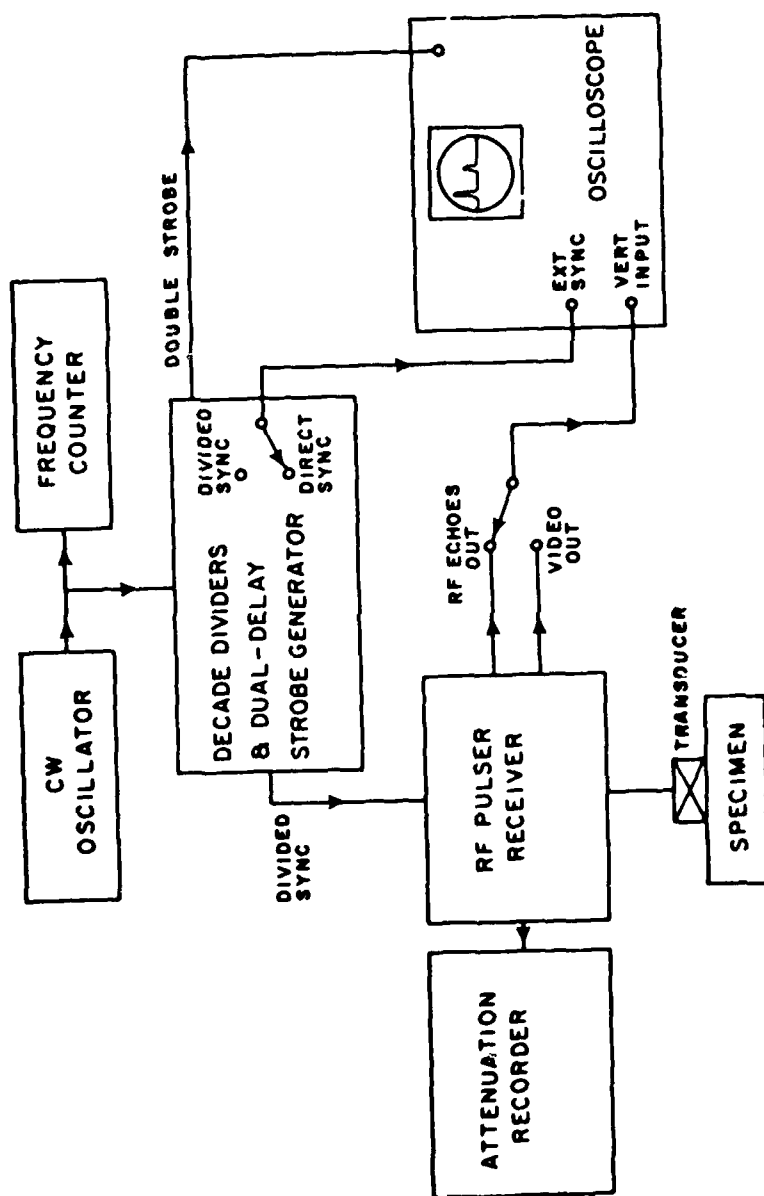


Figure 2. Ultrasonic Wave Velocity and Attenuation Measurement System

the frequency of which was characteristic of the wave speed and thickness of the specimen under consideration. The frequency of the signal was measured and displayed by the frequency counter. The decade divider and dual delay strobe generator divided the frequency of the sync signal by selected powers of ten so that it was suitable for triggering the pulser-receiver and provided the strobed intensification required for the pulse-echo overlap technique. In the divided sync mode, one is able to tune the pulse-echo train, which is displayed on the oscilloscope screen. The direct mode enables one to overlap two echoes due to the persistence of the scope display. The pulser-receiver and transducer pulse the specimen with ultrasound and detect the subsequent echoes. Both commercial ceramic and quartz single crystal transducers along with appropriate couplants were used in the research. Using a double pulse null technique, radio frequency (rf) echoes were overlapped on the oscilloscope screen by adjusting the output of the cw oscillator. When successive rf echoes were properly overlapped, the frequency output of the cw oscillator multiplied by the travel distance between echoes, or twice the specimen thickness, gave the sound wave velocity. The video output was used to properly align the strobes from the attenuation recorder before making the attenuation reading in units of decibels (dB's). The attenuation recorder includes a time gate permitting selection of any two echoes from the

received wave train, an automatic gain control to stabilize the amplitude of the echoes, and circuitry to obtain the logarithm of the ratio of the selected echo amplitudes.

Longitudinal wave velocity was measured at various locations along several welded samples. Data for two of these welds are shown in Fig. 3 and 4. The sound wave travel path is indicated by the specimen thickness. Wave velocity was lowest in the center of the weld where the ultrasound primarily passed through weld metal. The velocity difference from weld metal to base metal was about one percent. Peaks in the velocity versus distance curve occurred just outside the weld zone. Further from the weld the velocity decreased slightly as it returned to the unaffected base plate value. In the thinner specimens tested, the peaks in velocity occurring just outside the weld zone were either less pronounced or not present at all. An explanation of the behavior seen in Figs. 3 and 4 requires consideration of both varying microstructures and varying oxygen content throughout the weld. X-ray diffractometer measurements (to be presented later) can qualitatively account for part of the observed velocity data.

The goal of this research was to be able to characterize the weld region in a welded titanium specimen. Figure 5 represents an initial attempt at this. As the transducer was

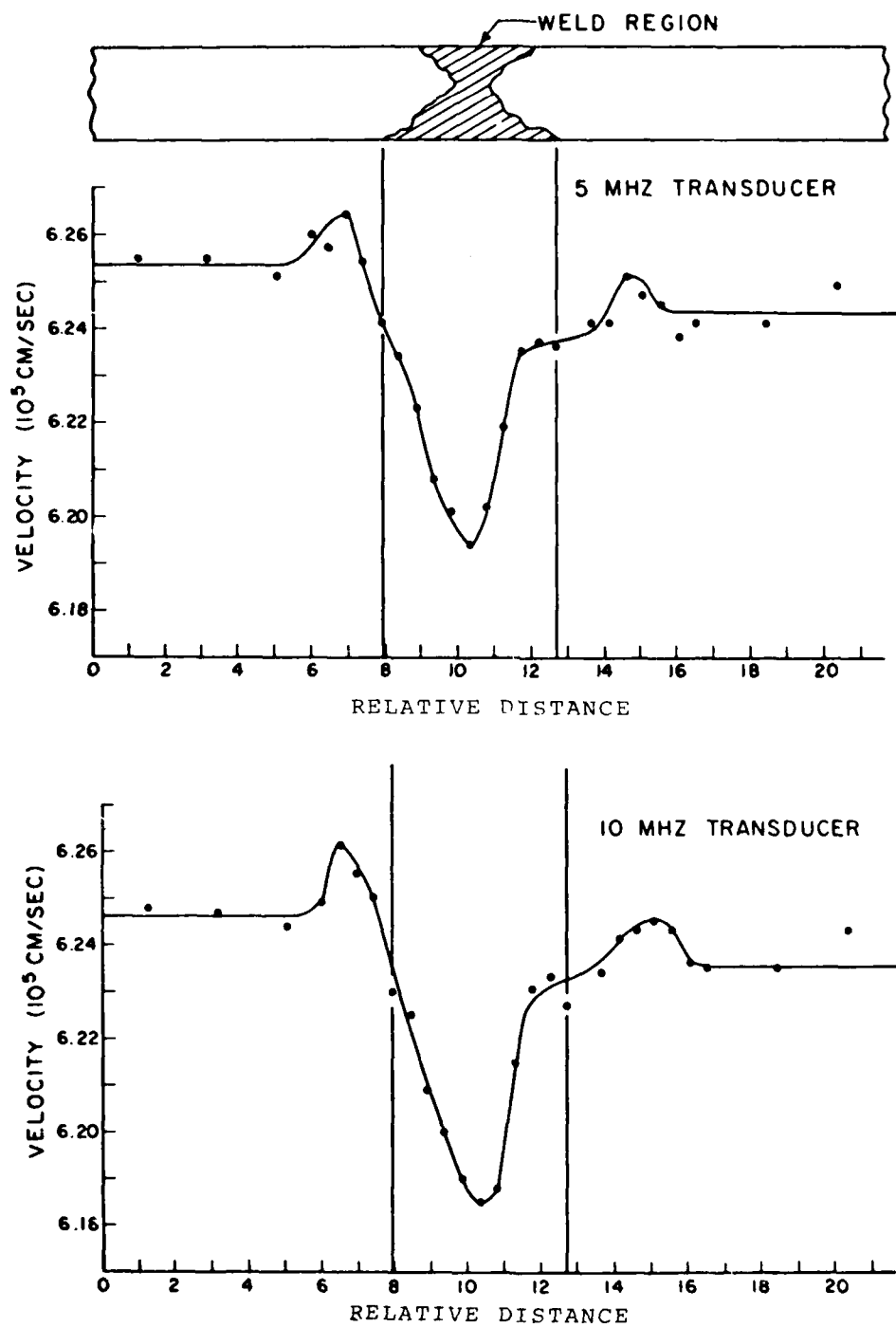


Figure 3. Longitudinal Wave Velocity vs. Transducer Location along the Specimen

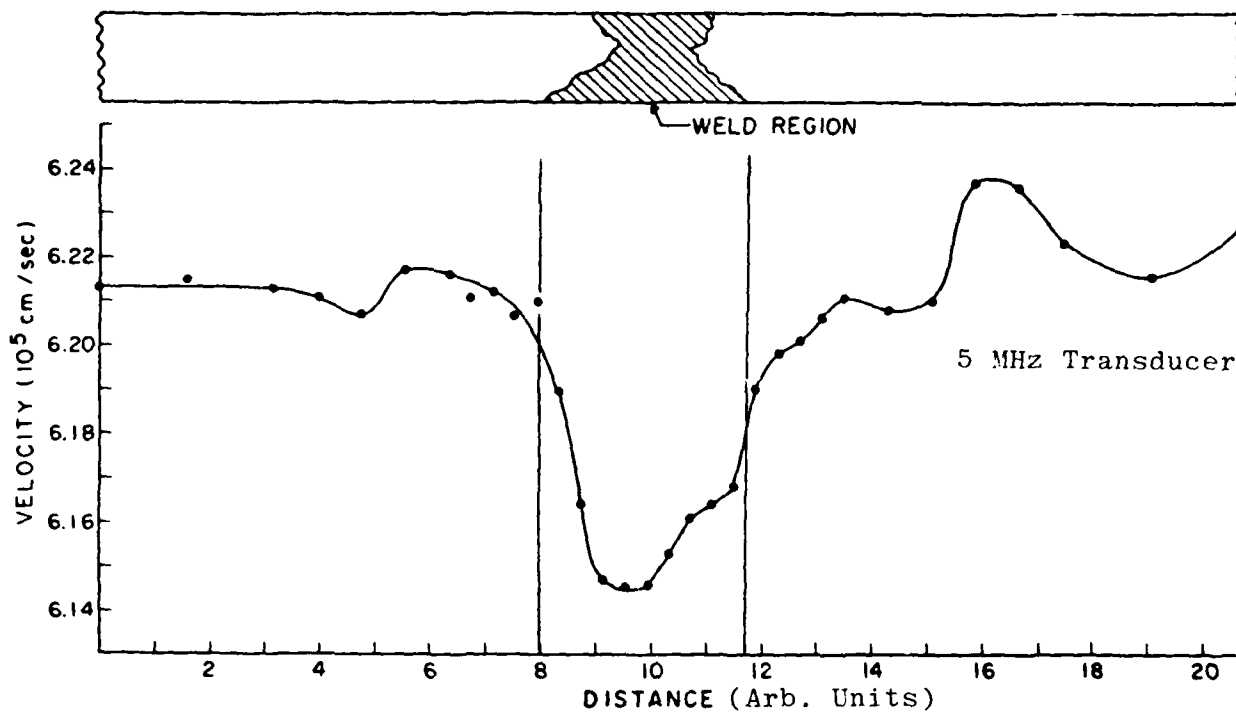


Figure 4. Longitudinal Wave Velocity vs. Transducer Location along the Specimen

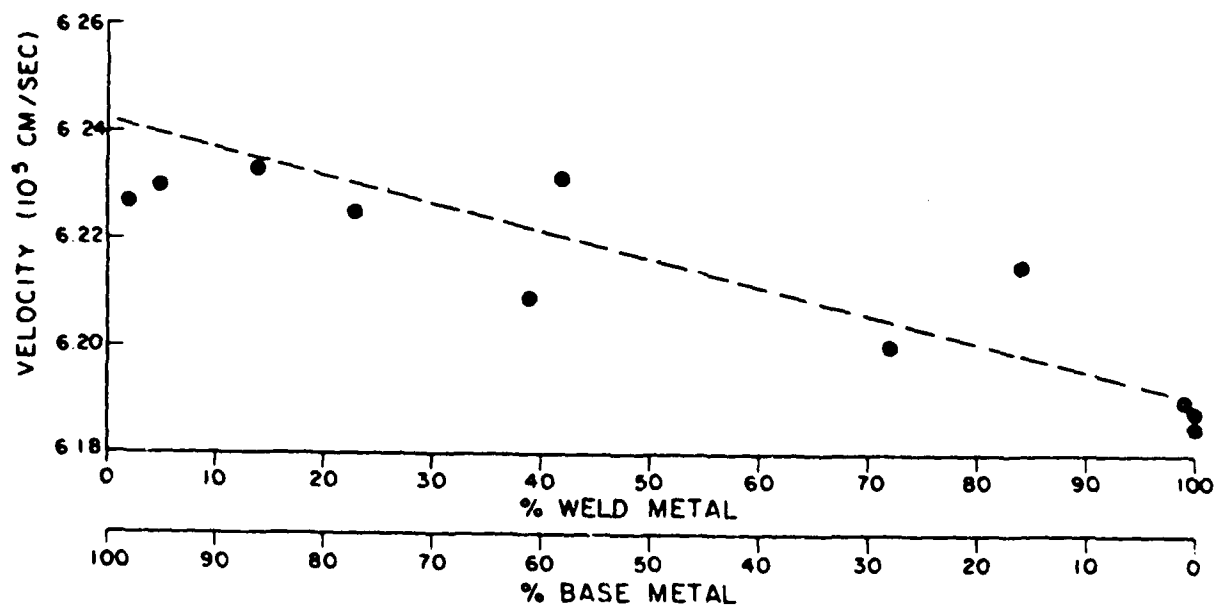


Fig. 5. Longitudinal Wave Velocity vs. % Weld Metal

moved across the weld shown in Fig. 3, the ultrasound propagated through some combination of weld and base metal. The wave velocity was plotted versus percentage weld metal or, conversely, base metal. Additional scans of this type need to be run, especially with smaller diameter transducers to reduce averaging effects.

Shear wave velocity measurements were also made at various locations on welded Ti 6211 samples in order to both evaluate the anisotropy and calculate the effective elastic moduli of the material in question. Salol (benzoic acid, 2 hydroxy, phenyl ester - an organic crystalline solid at room temperature that melts to a clear liquid at 43°C) was found to be the best couplant for the shear wave, Y-cut quartz transducers. However, the use of salol made it difficult to obtain reproducible bonds and reproducible transducer - specimen axis orientations. For these reasons, shear wave attenuation measurements were not made. The shear wave velocity measurements were complicated by the fact that phase shifts of 180° between successive echoes might or might not occur, depending on transducer location and bond character. In general, phase shifts were more likely to occur in the weld zone than in the base metal.

The anisotropy of the base metal and of the weld region was studied by measuring the shear wave velocities for

various angles between the particle displacements and the specimen axis (defined as the axis parallel to the rolling direction in the base metal and perpendicular to the direction of the weld passes). The specimen used for these tests was the same one for which data is presented in Fig. 3. Sound wave velocities were measured at two locations on the specimen, one in the base metal removed from the weld and one in the center of the weld zone. Both locations exhibited anisotropy with respect to shear wave propagation. The anisotropy of the base metal was on the order of a few percent.

Effective elastic moduli were calculated (Table I) for a welded specimen using longitudinal and shear wave velocity data and density measurements. As shown above, shear wave velocity determinations indicated definite texturing on the Ti 6211 specimens, especially on the rolled base plate. However, the isotropic assumption was made in order to easily calculate the elastic moduli (hence, use of the term "effective elastic moduli"). For consistency shear wave velocities were determined with particle displacements parallel to the specimen axis. Density was found to be greater in the weld region than in the base metal. This difference was considered in calculating the moduli.

Shear wave velocities were measured (particle displacements parallel to specimen axis) and elastic moduli

Table 1. Effective Elastic Moduli

MODULI	WELD REGION	BASE METAL
$\mu^* (10^{12} \text{ dynes/cm})$	0.453	0.456
$\lambda^* (10^{12} \text{ dynes/cm})$	1.257	1.266
$E^* (10^{12} \text{ dynes/cm})$	1.238	1.248
ν^*	0.368	0.368
$Kc^* (10^{12} \text{ dynes/cm})$	1.563	1.578

subsequently calculated at various locations along the welded specimen depicted in Fig. 3. Longitudinal wave velocity, shear wave velocity, shear modulus, Young's modulus, and Poisson's ratio are all plotted as a function of the distance along the specimen in Fig. 6. Note that the shear wave velocity (1) exhibits a local maximum in the weld whereas the longitudinal wave velocity exhibits a minimum and (2) exhibits local maxima outside the weld region similar to those observed for the longitudinal wave velocity. The variations in the elastic moduli track those of the shear wave velocity more closely than those of the longitudinal wave velocity. Poisson's ratio is practically constant, regardless of the location on the specimen.

Ultrasonic attenuation was also monitored at various locations along welded Ti 6211 specimens. Data for the same specimen shown in Fig. 3 are presented in Fig. 7. It appears that the peaks in the attenuation versus distance curve approximately correspond to points of inflection in the velocity versus distance curve. The general trend in attenuation is shown by the curve drawn through the data points. Attenuation is significantly higher in the base metal than in the weld metal, probably because the base metal is a rolled product. There is greater scatter of ultrasound at grain boundaries subjected

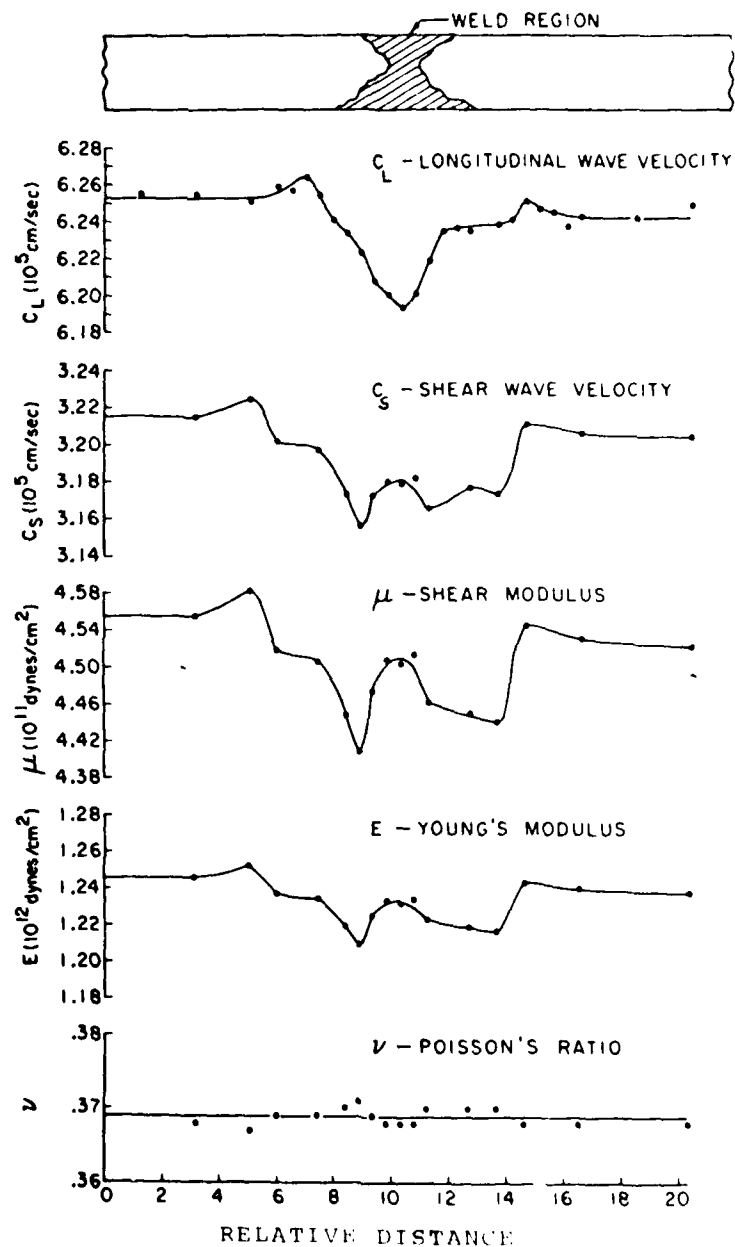


Figure 6. C_L , C_S , μ , E and ν vs. relative distance along Welded Specimen

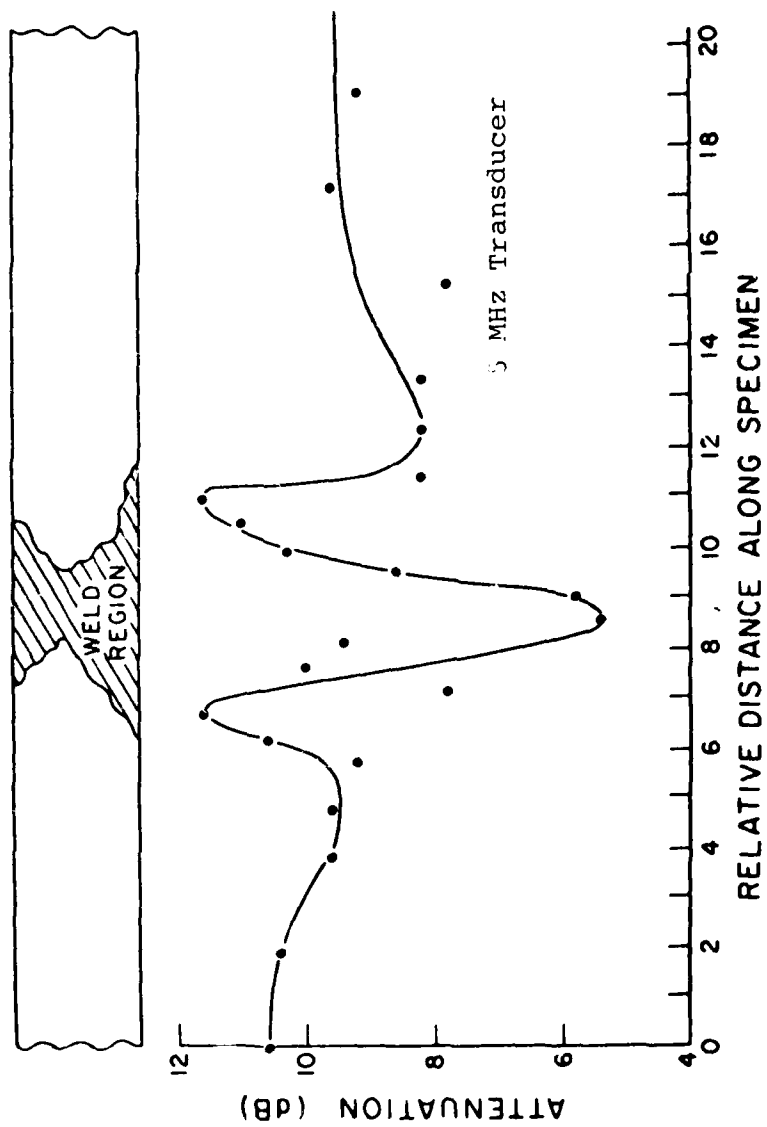


Figure 7. Attenuation vs. Distance Along a Welded Titanium Specimen

to the severe plastic deformation induced by rolling. The high values of attenuation that occur just inside the weld region could be due to scattering from the weld metal/base metal interface, possibly accentuated by microcracking.

X-Ray Measurements

As mentioned before, the Ti 6211 alloy is a near alpha alloy containing primarily alpha phase (HCP) metal with some beta phase (BCC) metal. The sound wave velocity should be lower in the beta phase, because it has a more open crystal structure than the alpha phase. Hence, the decreased sound velocity observed in the weld region could possibly be caused by an increased amount of beta phase metal present in the weld region. X-ray diffractometer measurements were performed to test this hypothesis.

Initial diffractometer scans indicated that the BCC (110) and the HCP (101) peaks could be used to qualitatively assess changes in the relative amounts of alpha phase and beta phase material. Subsequent scans clearly demonstrated that the weld region of the specimen tested contained more beta phase metal than the base plate. These results, along with consideration of the thermal history of the weld zone, support the hypothesis presented above. The rapid cooling rates present during welding should result in more retained, high temperature beta phase metal and, hence, lower sound wave velocities.

Hardness Measurements

Rockwell C hardness measurements were made along a welded 6211 specimen in accordance with ASTM Standard E18. A diamond-tipped "Brale" indenter with a 150 kgm load was used. Since Ti 6211 continued to exhibit plastic flow after the application of the major load, the dial indicator continued to move after the operating lever stopped. For this reason, the operating lever was brought back to its latched position at an elapsed time of 30 seconds between application and removal of load.

The results of the hardness measurements performed are presented in Fig. 8 and are similar to the results obtained from velocity and attenuation measurements on thick-section welds. The weld region was softer than the unaffected base metal. Just outside the weld, in the heat affected zone, the hardness was clearly higher than that of the base metal. Absorption of interstitial oxygen, nitrogen, and hydrogen (alpha stabilizers) during welding could account for this behavior. Solid solution strengthening due to the presence of these interstitials would increase the hardness. The microstructures observed in this region of high hardness lend some validity to this proposed hardening mechanism.

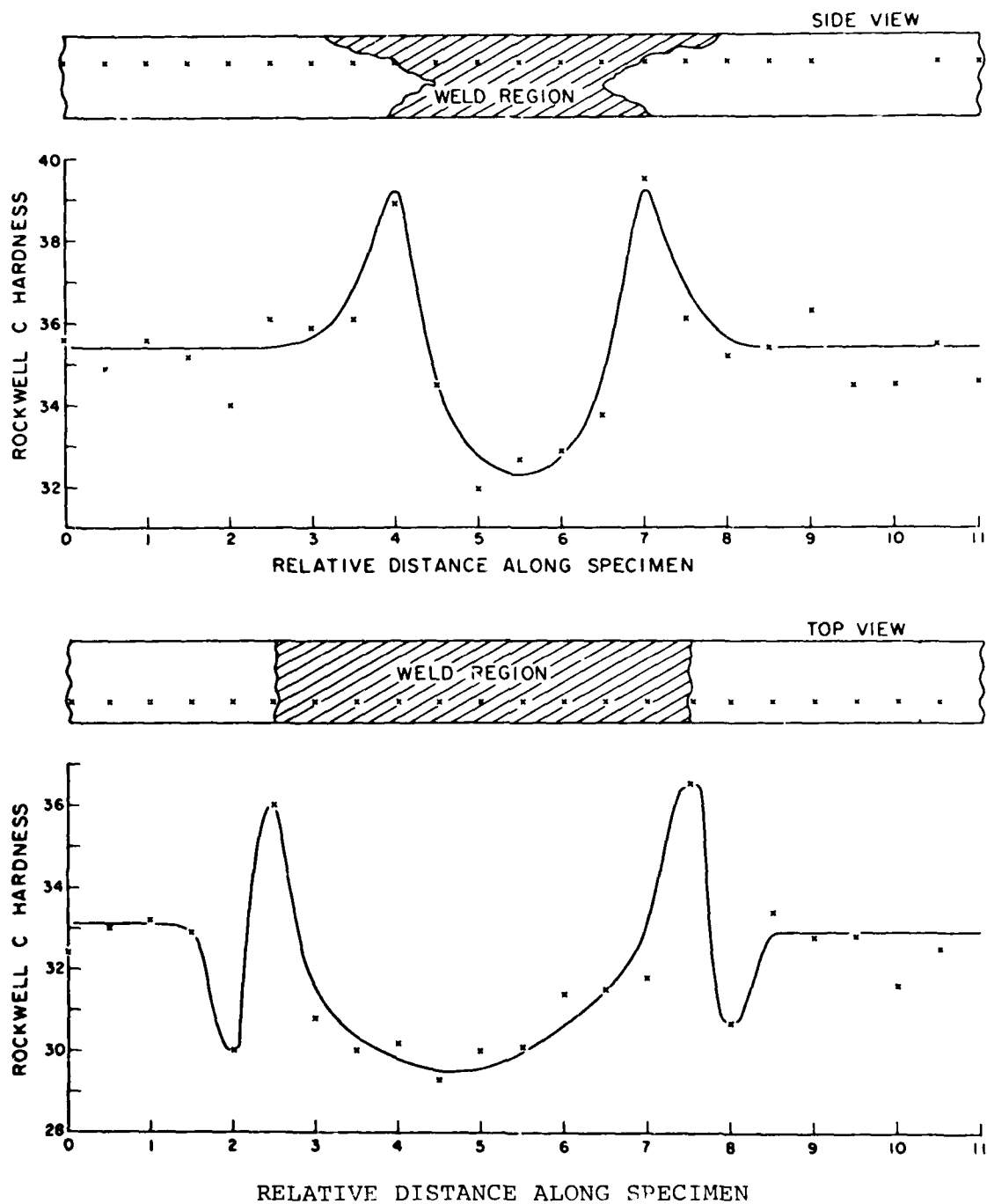


Figure 8. Rockwell C Hardness vs. Relative Distance along a Welded Titanium Specimen

Conclusions

The data accumulated from acoustical, mechanical, X-ray diffractometer, and metallographic evaluations of Ti 6211 weldments form a consistent picture. Both the velocity and attenuation were observed to be lower in the weld region than in the base metal. Initial attempts at correlating the acoustic data with the weld profile were promising. Additionally, changes in the velocity and attenuation were correlated with compositional and microstructural variations in the weld region and base metal. Rockwell hardness measurements, made as a function of position across the specimen surfaces, compared favorably with the ultrasonic measurements.

DETECTION OF INTERSTITIAL GAS BY INTERNAL FRICTION AND MODULUS METHODS

B. R. Tittmann

*Rockwell International Science Center
Thousand Oaks, California 91360*

The Science Center has maintained a group of experts in titanium metalurgy for more than 10 years. A significant part of the effort has been to characterize the influence of controlled amounts of N, O, and H on properties and microstructure of Ti alloy. Equipment is available for doping of Ti alloys with O and N (by remelting with appropriate quantities of oxides and nitrides) and for introduction of specified quantities of hydrogen (using a Sieverts apparatus). Standard samples contaminated with known amounts of interstitials can be interrogated for mechanical properties (hardness, strength, toughness) and physical properties (acoustic modulus, damping, electrical conductivity, etc.).

In one study on Ti-V alloys unexpectedly large effects of oxygen and hydrogen on the low temperature internal friction peaks associated with a thermal $\beta \rightleftharpoons \omega$ transformation have been observed using combined damping and modulus measurements and cold stage electron microscopy. The measurements show that O suppresses the omega start temperature, whereas H raises it. It is speculated that not only the size of the dopants but also their electronic state contribute to changes occurring in metastable β alloys (1).

In another related study, the effect of H and temperature on the strength and modulus of beta-phase Ti alloys has been studied. The effect of H on Ti-18 Mo alloy is to decrease the Young's modulus above ~ 150 K and increase the modulus below this temperature. The effects of H on the tensile strength of the alloy follow the same trends as the modulus. These observations have been explained in terms of an electronic interaction between H and the host lattice (2).

- (1) O. Buck, D. O. Thompson, N. E. Paton and J. C. Williams, Proc. of Fifth International Conference on Internal Friction and Ultrasonic Attenuation in Solids (Edited by D. Lenz and K. Lucke) Springer Verlag Berlin, 1975, p. 951.
- (2) N. Paton and O. Buck, Proc. of Conference of Hydrogen on Behavior of Materials, AIME, New York, 1976, p. 83.

1.0 INTRODUCTION

In alloys containing IV-B elements, Ti, Zr, Hf and V-B or VI-B elements, such as V, Nb, or Mo in suitable amounts, the high temperature bcc allotropic form can be retained in a metastable state by quenching to room temperature from the single phase bcc field [1]. The resulting bcc phase can undergo a series of decomposition reactions depending on the alloy composition and reaction temperature. Such reactions lead to the formation of two types of martensite and several metastable phases [2]. Decomposition of metastable bcc Ti alloys has been discussed in several recent papers [3-7] both from an experimental and a theoretical point of view with particular emphasis on the formation of the athermal $\beta \rightleftharpoons \omega$ transformation. It has been postulated [5] that this athermal $\beta \rightleftharpoons \omega$ transformation can be explained by a two-dimensional ordering of linear one-dimensional defects, with each defect consisting of a $1/3$ vacancy and a $1/3$ interstitial in a vernier-like fashion [8]. The possibility that such defects not only form the nuclei of the phase transformation, but are also responsible for electron diffraction [3,9] and neutron diffraction effects well above the transformation temperature [10], as well as internal friction [6,11] and anomalous diffusion [12] in such alloys, has been pointed out.

Recently, using cold stage electron microscopy and selected area electron diffraction, Paton and Williams [13] have shown that an increase in oxygen content markedly reduces the $\beta \rightleftharpoons \omega$ transformation temperature. These authors have suggested that this observation is consistent with an interaction of interstitial oxygen atoms with the linear defects mentioned above.

The internal friction spectrum of high purity metastable β phase alloys was studied before by Nelson et al [14], Doherty and Gibbons [11], and more recently by Sommer et al [6]. In general, two very strong internal friction peaks are observed in these alloys, both of which can be attributed to thermally-activated processes. Experiments performed at 20 kHz [6] show that the low-temperature peak (P_L) occurs at about 30K (or below) while the high-temperature peak (P_H) occurs at about 120-140K. The process responsible for P_L has not been identified in all details thus far. The only explanation is due to Nelson et al [4] who speculate that possibly a Jahn-Teller-type distortion [15] could be responsible for this relaxation process. P_H is probably caused by a relaxation process in the β phase; this process has been connected with the $\beta \rightleftharpoons \omega$ transformation [6,11,15]. The height of P_H passes through a maximum with increasing solute concentration with the maximum occurring at an alloy composition whose

ω_3 , the start temperature for ω formation, corresponds to a temperature at which P_H occurs. In an earlier paper, De Fontaine and Buck [5] discussed the connection between the linear one-dimensional defects, mentioned above, and the $\beta \rightleftharpoons \omega$ transformation. They also suggested that these defects would act as an elastic dipole oriented along $\langle 111 \rangle$ which can give rise to an internal friction peak although the exact mechanism is unspecified at the present time [5].

The purpose of the present paper is to review recent studies [6,17] at the Science Center on the influence of systematic variations in substitutional solute concentration on the internal friction spectrum of Ti alloys and then to examine the effect of oxygen and hydrogen content since at least the former of these has been shown to later independently the $\beta \rightleftharpoons \omega$ transformation temperature [13]. Cold stage electron microscopy and electron diffraction studies have been conducted to support the internal friction results. The effect of H and temperature on the strength and modulus of beta-phase Ti alloys has also been studied.

II. INTERNAL FRICTION AND MODULUS IN Ti-V ALLOYS

A. Experimental Procedures

The internal friction and modulus measurements were performed on titaniumvanadium alloys in the form of cylindrical bars 12.5 cm long and 6 mm in diameter. The bars were mounted with three set screws at their center of gravity with both ends free; their resonant frequency in the fundamental mode was about 20 kHz and the maximum strain amplitude about 2×10^{-7} . The apparatus used has been described in detail earlier [18]. Measurements were made over a temperature range from about 20 to 300K. Hydrogenation of a Ti-30V specimen and oxygenation of a Ti-20V specimen were accomplished by heating them up to about 900°C in a micro-Sieverts apparatus containing a known quantity of oxygen or hydrogen. Following charging, the samples were rapidly cooled by withdrawing the furnace from the glass Sieverts apparatus tube and cooling the tube containing the samples to room temperature by a cold air stream. The cooling rate obtained by this procedure was found to be sufficiently rapid to retain the β -phase in Ti-30V but the Ti-20V specimen had to be homogenized at 900°C in argon for about 24 hours and then quenched into ice water.

All measurements discussed in the following were taken during warm-up at a rate of about 0.3K/min. Measurements were also taken during cool-down, but they are less complete than the warm-up measurements since the internal friction was so large that the power input into the drive coil exceeded the heat extraction capability of the heat exchanger, resulting in cessation of cooling at a temperature just above the peak temperature. In those cases, the measurements were interrupted until a temperature of 20K was reached.

Thin foils of several high-purity and oxygenated or hydrogenated alloys were prepared standard techniques. They were examined in the cooling stage of a Phillips 300 electron microscope at temperatures from room temperature down to about 100K.

B. Results

Typical results of internal friction and Young's modulus measurement in high-purity Ti-20V and Ti-30V alloys are shown in Fig. 1. P_H dominates the internal friction spectrum of Ti-20V, whereas P_L dominates the spectrum of Ti-30V. This figure shows that a large modulus defect accompanies the damping peaks in both alloys. The peak height δ_{\max} of P_L and P_H as a function of V concentration over the range 20V to 50V are exhibited in Fig. 2 from which it can be seen that the maximum damping is associated with P_H and occurs in the vicinity of 24V; a value of 3×10^{-2} has been established as lower limit for this maximum. Figure 2 also shows that P_L starts to grow as soon as P_H starts to disappear. Above 30V, P_L drops below 20K which is out of the temperature range of the present experiment.

The effects of oxygen concentration on the internal friction of a Ti-20V alloy are shown in Fig. 3(a). The starting material had a residual concentration of about 0.08 at % O (≈ 0.027 wt% O). The internal friction measurements are consistent with the results shown in Fig. 1, with the addition of a shoulder in the damping curve at the high temperature side of P_H . Additionally, the low temperature modulus (Fig. 3(b)) is somewhat smaller than shown in Fig. 1. This can be ascribed to a slight variation in V concentration

between the two alloys since the modulus is a very sensitive function of V over this concentration range. Increasing the oxygen concentration over the base line level results in a pronounced decrease in the height of P_H (Fig. 3(a)). Concomitant with the decrease in P_H , P_L becomes detectable, although it is not possible at the present time to give a functional relation of its height with oxygen concentration (see also Fig. 3(a)). The modulus measurements (Fig. 3(b)) reflect the damping measurements in that both P_H and P_L are accompanied by modulus defects; quantitative statements cannot be made at present regarding the relation between modulus and oxygen concentration.

Very pronounced changes in the internal friction spectrum accompany hydrogen charging Ti-30V (residual hydrogen content in these alloys is about 0.03 at% H = 6 wt ppm H). These results are illustrated in Figs. 4(a) and (b): Fig. 4(a) shows that the height of P_H increases with increasing hydrogen concentration. Simultaneously, the height of P_L decreases and disappears completely at hydrogen concentrations above 0.5 at% H. The absolute height of P_H for 5 at% H cannot be given because the power inputs required to measure exceed the machine capacity, but it can be estimated from the modulus defect at 120K (Fig. 4(b)). Such an estimate leads to a value for 5 at% H about five times larger than δ_{\max} for 1 at% H, or a value of about 3.5×10^{-2} . The modulus defect due to P_L disappears with increasing H concentration, whereas that due to P_H increases. Additionally, the temperature coefficient of the modulus above P_H becomes negative in the sample containing 5 at% H. The connection between the magnitude of P_H and the omega start temperature, ω_s , is best illustrated with the aid of Fig. 2, where the height of P_H for the

binary Ti-V alloys is a maximum when ω_s is close to the temperature at which P_H occurs (140K at 20 kHz). If ω_s is above or below 140K, then the magnitude of P_H decreases. Thus the effect of adding O or H on ω_s in Ti-V alloys can be determined by measuring P_H . In the Ti-20V, adding oxygen lowers P_H and from this it can be inferred that ω_s was lowered. On the other hand, adding hydrogen to the Ti-30V raised P_H and ω_s .

The correctness of these deductions was checked by using cold stage transmissin electron microscopy. The microscopy and diffraction studies showed that the addition of oxygen depresses ω_s . No ω phase was observable at temperatures as low as 100K for the alloy Ti-20V + 0.42 at% O. This is in contrast to observations on the starting material which contained 0.08 at% O and had an ω_s just below room temperature. Limited microscopy results showed that addition of hydrogen raises ω_s of Ti-30V.

C. Discussions

The results obtained in this work generally verify earlier observations on the internal friction spectra of high-purity Ti-V alloys and earlier electron diffraction studies of structural changes [13] in oxygenated Ti-V alloys. No systematic studies on the influence of hydrogen on either the internal friction spectrum or structure of Ti-V alloys have been reported previously; therefore, no comparison with earlier work is possible.

Four specific observations have been made:

1. The internal friction measurements indicate that the omega start temperature, ω_s , is strongly affected by the presence of oxygen and hydrogen; oxygen suppresses ω_s in Ti-20V whereas hydrogen raises ω_s in Ti-30V. This is schematically indicated in Fig. 5 which shows the manner in which O and H shifts ω_s in Ti-V alloys.
2. The low temperature peak, P_L , seems to grow only when the high temperature peak disappears. This has been found in high-purity Ti-V alloys of variable V content (see Fig. 2), as well as in hydrogenated Ti-30V (see Fig. 6) and in oxygenated Ti-20V (as indicated by the results presented in Fig. 3).
3. The internal friction results on peak, P_H , and limited electron microscopy results are in mutual agreement and, therefore, support the suggestion that the same mechanism which causes streaking in the diffraction patterns also causes the peak P_H .
4. The effects of oxygen and hydrogen on Young's modulus are unexpectedly large.

As has been pointed out before [14], the high temperature peak, P_H , can be explained by assuming that the compressional part of the linear displacement defect forms an elastic dipole in a $\langle 111 \rangle$ close-packed direction. It is suggested that an external stress would modify the population of $\langle 111 \rangle$ defects in preferred directions, thereby giving rise to energy dissipation.

At the same time, this defect can be locked into ω positions by the cooperative motion of similar defects on neighboring $\langle 111 \rangle$ rows, thereby forming the nuclei for the athermal ω phase. Combined electron transmission and internal friction experiments indicate that the dissipation process operates to the maximum extent at a temperature just above that where the ω -phase actually appears, since such a temperature corresponds to the greatest population of linear displacement defects [6].

A complete explanation of the doping experiments presented above is not possible at present because of the complexity of the subject. However, it should be recalled that earlier studies [18] have shown that the β -phase becomes more stable as the electron:atom ratio increases. Such increases in stability are accompanied by a reduction in the ω_s temperature. The present results suggest that size and/or electronic effects of oxygen and hydrogen can contribute to the changes occurring in these alloys. For the concentrations studied here, oxygen and hydrogen exist in the bcc lattice as an interstitial solid solution; but the two atom types probably occupy different sites in the Ti-V lattice.

The effects of hydrogen on the internal friction spectrum of Ti-30V could then be rationalized by assuming that the hydrogen becomes a negatively charged ion (acceptor) or possibly forms a negatively-charged VH complex. Thus the addition of H would have the same effects as a reduction in V concentration. Indeed, the results in Figs. 2 and 6 show that the height of P_H in Ti-30V + 5 at% H compares favorably to the height of P_H in a high-purity alloy of composition close to Ti-24V. The size of the H ion should be small so that

it fits well into an interstitial site without generating a stress field, since H does not increase the yield stress σ_y significantly [19].

If the above line of reasoning is applied to rationalize the effect of oxygen on the internal friction spectrum of Ti-V alloys, it is obvious, as will be shown below, that electronic effect alone cannot account for the observation that oxygen suppresses the $\beta \rightleftharpoons \omega$ transformation [13]. It is proposed that the observed effects of oxygen are the combined result of an electronic and an elastic interaction of oxygen with the bcc Ti-V matrix. Assuming that the oxygen forms a positively charged ion (donor), the addition of O would have the same effect as an increase in the V concentration. In light of the results presented in Figs. 2 and 3, the height of P_H in Ti-20V + 0.42 at% O compares favorably to the height of P_H in high purity Ti-30V. It is hard to imagine, however, that such a small O addition changes the e/a ratio as much as is expected from the change in V content. The observation [19] that small additions of O increase σ_y significantly, suggests a large misfit of the O ion in the Ti-V lattice. Its associated stress field interacts with the stress field of the linear displacement defect, thus suppressing the formation of the ω phase. However, the presence of electronic effects should not be neglected since they are supported by the earlier work of Sass [20] who found that the metastable bcc phase could only be retained on quenching a Ti-75% Zr alloy if it was contaminated by oxygen. This suggests that oxygen acts like a donor, thus increasing the electron concentration in Ti-Zr alloys in a manner similar to the addition of V, Mo, Cr, and other known β -stabilizing elements.

It should be mentioned that the present authors are aware that the assumption of a positively charged O ion is in contradiction to arguments which predict a negatively charged ion based on the electronegativity difference [21] of O with respect to Ti or V. As has been pointed out elsewhere [22] such arguments do not hold in very dilute alloys, and should therefore not be used in the present context.

III. THE EFFECT OF HYDROGEN AND TEMPERATURE ON THE STRENGTH AND MODULUS OF BETA PHASE Ti ALLOYS

A. Introduction

In the work on the Ti-30V Alloy, it was noted that the Young's modulus decreased with increasing H content at room temperature (300K), but at low temperature (below about 150K) the modulus increases with increasing H content. Since the decrease in yield strength and proportional limit with H was related to the decrease in Young's modulus, it might be expected, that at low temperature (<150K), where the modulus increases with H content, an increase in strength might be observed. Accordingly, in the temperature dependence of both the Young's modulus and the strength of the Ti-18Mo alloy were determined. In addition, the effect of H and temperature on the strength of a commercial beta phase Ti alloy Ti-3Al-8V-6Cr-4Mo-4Zr (Beta "C") were determined to investigate whether H might decrease the strength of complex commercial alloy in a manner similar to that found earlier for a simple binary model alloy [23].

B. Experimental

The Ti-18Mo alloy was prepared from starting materials containing 1400 ppm total (O + N). Tensile samples were not rolled to sheet ~ 1 mm thick, while samples for Young's modulus and internal friction measurements were arc cast and swaged to a diameter of 6.3 mm with a length of 125 mm. Specimens were chemically polished in a solution containing 40% HNO₃, 30% HF

and 20% H_2SO_4 and then charged with H in a Sieverts apparatus for 15 mins at 1073K. The amount of H introduced into the specimen was determined by the pressure change in the system and was subsequently verified on selected specimens by vacuum extraction. The Beta "C" alloy was obtained in the form of ~ 1 mm thick sheet and the same H charging procedure was used. After charging at 1073K, specimens were cooled rapidly by forced air cooling of the quartz furnace tube; and this cooling rate was sufficient to retain the bcc beta phase in both alloys. All the H introduced was retained in solid solution.

Tensile properties were determined in an Instron machine at an initial strain rate of $2.3 \times 10^{-4} \text{ s}^{-1}$ using a sensitive extensometer. Low temperature tests (150, 240K) were conducted in dry nitrogen gas. Tests below 150K were not possible on because of the risk of damage to the extensometer. Proportional limit and 0.2% offset yield strength were determined, and samples were strained 3% for subsequent examination of selected samples by transmission electron microscopy. Thin foils were prepared by an ion milling technique to eliminate difficulties encountered with spontaneous relaxation in foils prepared by conventional electropolishing [24].

C. Results and Discussion

Tensile test results on the Ti-18Mo alloy showed that at 300K and 240K both the proportional limit and the 0.2% offset yield strength decreased with increasing H content. When plotted as a function of \sqrt{c} as in Fig. 7 this decrease was linear, in good agreement with results at 300K reported earlier [23].

Also plotted in Fig. 7 are tensile data obtained at 150K and although the 0.2% offset yield strength decreases with increasing H content, the proportional limit is essentially invariant with H content.

Comparison of the strength data with those of Young's modulus and internal friction provides an interesting comparison. A plot of Young's modulus as a function of temperature and hydrogen concentration is shown in Fig. 8. Below 150K the modulus increases with increasing H concentration, whereas above this temperature the modulus decreases with increasing H content. These are the same trends as noted in Fig. 7 for the proportional limit data where at 150K the strength was essentially invariant with H concentration as was the modulus.

This correlation between modulus and strength was previously rationalized [23] in terms of the critical shear stress for slip, τ , on the Young's modulus, E , as

$$\tau \approx \frac{Eb}{6\pi R}$$

where R is the average spacing between the pinning points and b is the Burgers vector. This rationale seems well justified by the present results where both modulus and proportional limit are essentially independent of H concentration at 150K but decrease H concentration above this temperature. Unfortunately, measurements of proportional limit at 100K could not be made with available equipment but on the basis of the modulus data the strength would be expected to increase with increasing H concentration.

A complication arises in interpretation of the low temperature data because of the formation of the athermal omega phase in the alloys studied [13,3]. Omega phase would be expected to increase the strength of the Ti-18Mo alloy [25] and H is thought to increase the propensity for omega phase formation. Thus an increase in strength with increasing H concentration at low temperature might be attributed to omega phase formation.

Typical results of internal friction measurements as a function of temperature and hydrogen concentration are shown in Fig. 9. The results are very similar to the ones obtained on hydrogen charged Ti-30V. At about 130K a large internal friction peak is observed which increases with increasing hydrogen concentration. In the vicinity of the maximum the internal friction at the higher H concentrations is so large, that the power amplifiers of the apparatus became saturated. The internal friction peak is accompanied by a large modulus defect which increases with increasing H concentration. At temperatures below the internal friction maximum the modulus (Fig. 9) increases with increasing H concentration, whereas at high temperatures it decreases with increasing H. This modulus defect and internal friction peak has been connected with the athermal $\beta \rightleftharpoons \omega$ transformation of metastable bcc alloys. The two-dimensional ordering of linear one-dimensional defects with each defect consisting of a 1/3 vacancy and a 1/3 interstitial in a vernier-like fashion gives rise to an energy dissipation, which is a maximum at temperature just above the ω_s temperature. The same type of defect forms the nuclei of the phase transformation and is responsible for electron [3] and neutron diffraction effects [26]. The essential point here is that H

increases the temperature at which the internal friction peak is first observed, and increases its magnitude.

Similar measurements have been made on the influence of H on the strength of a commercial beta phase Ti alloy Ti-3Al-8V-6Cr-4Mo-4Zr (Beta "C"). Both proportional limit and 0.2% offset yield strength results at room temperature are shown in Fig. 10 and it is apparent that the strength increases with H concentration rather than decreases, as is the case with the Ti-18% Mo alloy. Although measurements of modulus and internal friction have not been made for the Beta "C" alloy, it is probable that this difference in behavior is accounted for by the decreased stability of the Beta "C" alloy in comparison to the Ti-18Mo alloy. A higher ω_s temperature in the former alloy would promote the formation of the ω phase on addition of hydrogen, thus giving rise to an increase in strength, rather than the decrease noted with the Ti-18Mo alloy.

Transmission electron microscopy of foils prepared from the Ti-18Mo alloy was conducted to investigate the influence of H on slip mode. It was found that hydrogen reduced the slip band width by inhibiting cross slip, as shown in Fig. 11. This increased tendency toward planar slip with hydrogen has also been observed for other metallic systems, an example being a Ni-30% Cu alloy [26]. It is of interest to note that at high hydrogen concentrations ($> \sim 2000$ ppm) slip band concentration was visible macroscopically on the surface of the sheet tensile samples, usually at one end of the gauge section. At low temperatures this was sufficiently intense that it gave rise to premature failure at ~ 2 -3% strain, whereas the strain to failure without

hydrogen would have been of the order of 18%. These results, however, are in contrast to the effect of oxygen on slip morphology in beta titanium alloys where oxygen tends to promote wavy slip [27].

The effect of H on the Ti-18Mo alloy is to decrease the Young's modulus above $\sim 150\text{K}$ and increase the modulus below this temperature. The effects of hydrogen on the strength of the alloy follow the same trends as the modulus. These observations have been explained in terms of an electronic interaction between H and the host lattice [23], and the present results would tend to confirm that explanation. Solid solution softening, in conjunction with the lattice parameter expansion, which occurs here [23], is difficult to account for on other grounds. Solid solution softening of bcc metals has been postulated by Beachem [28], but is limited solid solubility. The present results are made possible by the extensive solubility of H in beta Ti alloys.

REFERENCES

1. R. I. Jaffee in "Progress in Metal Physics," Vol. VII, Pergamon Press, London, 1958, p. 65.
2. J. C. Williams in "Titanium Science and Technology," Vol. 3, R. I. Jaffee and H. M. Burte, Eds., Plenum Press, 1973, p. 1433.
3. D. De Fontaine, N. E. Paton and J. D. Williams, *Acta Met.* 19, 1153 (1971).
4. N. E. Paton and J. C. Williams, *Proc. II Int. Conf. on Strength of Metals and Alloys*, American Soc. for Metals, 1970, p. 108.
5. D. De Fontaine and O. Buck, *Phil. Mag.* 27, 967 (1973).
6. A. W. Sommer, S. Motokura, K. Ono and O. Buck, *Acta Met.* 21, 489 (1973).
7. J. C. Williams, D. De Fontaine, and N. E. Paton, *Met. Trans.* 4, 2701 (1973).
8. H. R. Paneth, *Phys. Rev.* 80, 708 (1950).
9. S. L. Sass, "Proceedings of the Conference on the Local Structural Order and Decomposition of Titanium, Uranium, and Zirconium-Base B.C.C. Solid Solutions," Organized by S. L. Sass, Cornell University, New York, 1972 (unpublished).
10. D. T. Keating, J. D. Axe, and S. C. Moss, "Proceedings of the Conference on the Local Structural Order and Decomposition of Titanium, Uranium and Zirconium-Base B.C.C. Solid Solutions," Organized by S. L. Sass, Cornell University, New York, 1972 (unpublished).
11. J. E. Doherty and D. F. Gibbons, *Acta Met.* 19, 275 (1971).
12. A. D. LeClaire in "Diffusion in Body-Centered Cubic Metals," American Soc. for Metals, Metals Park, Ohio, 1965, p. 3.
13. N. E. Paton and J. C. Williams, *Scripta Met.* 7, 647 (1973).
14. C. W. Nelson, D. G. Gibbons, and R. F. Heheman, *J. Appl. Phys.* 37, 4677 (1966).
15. L. E. Orgel, "Introduction to Transition-Metal Chemistry: Ligand-Field Theory," John Wiley & Sons, New York, 1960.

16. O. Buck, D. O. Thompson, N. E. Paton and J. C. Williams, Proc. of Fifth International Conference on Internal Friction and Ultrasonic Attenuation in Solids (Edited by D. Lenz and K. Lucke) Springer Verlag Berlin, 1975, p. 951.
17. N. Paton and O. Buck, Proc. of Conference of Hydrogen on Behavior of Materials, AIME, New York, 1976, p. 83.
18. C. A. Luke, R. Taggart, and D. H. Polonis, Trans. Am. Soc. Metals 57, 143 (1964).
19. J. C. Williams and N. E. Paton, unpublished results.
20. S. L. Sass, Acta Met. 17, 813 (1969).
21. L. Pauling, "Nature of the Chemical Bond," Cornell Univ. Press, Ithaca, New York, 1959.
22. G. G. Libowitz and T. R. P. Gibb, J. Phys. Chem. 60, 510 (1956).
23. N. E. Paton, O. Buck and J. C. Williams, Scripta Met. 9, 687 (1975).
24. R. A. Spurling, C. G. Rhodes and J. C. Williams, Met. Trans. 5, 2597 (1974).
25. B. S. Hickman, AIME Trans. 245, 1329 (1969).
26. J. D. Frandsen, N. E. Paton and H. L. Marcus, Met Trans. 5, 1655 (1974).
27. N. E. Paton and J. C. Williams, Scripta Met. 7, 647 (1973).
28. C. D. Beachem, Met. Trans. 3, 437 (1972).

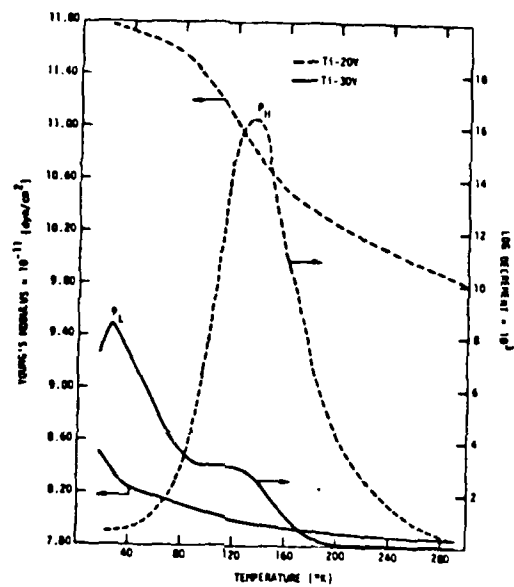


Fig. 1 Young's modulus and logarithmic decrement of Ti-20V and Ti-30V.

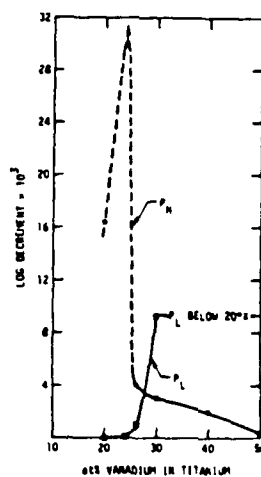


Fig. 2 The heights of the internal friction peaks P_L and P_H , respectively, as a function of alloy composition.

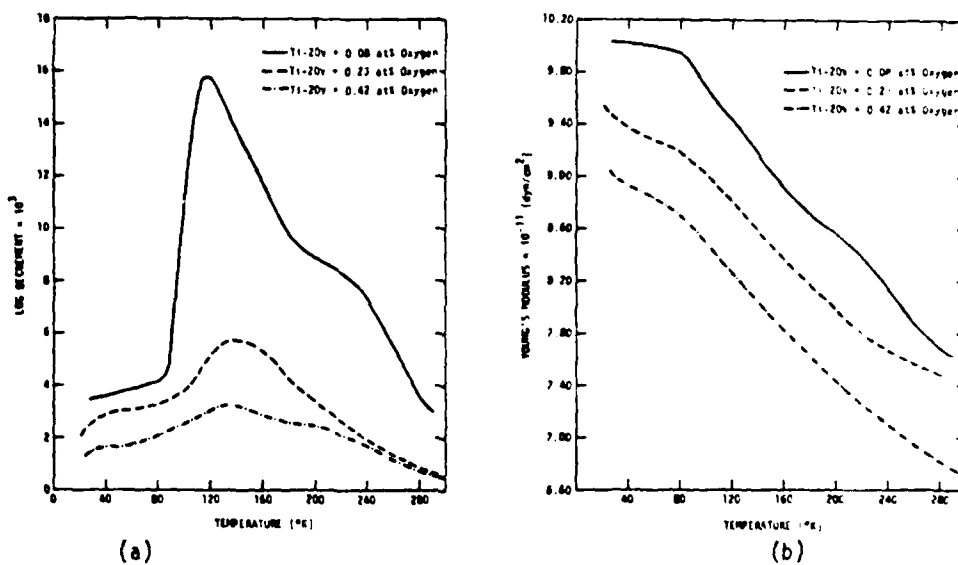


Fig. 3 (a) The logarithmic decrement, and (b) Young's modulus of Ti-20V as a function of temperature and oxygen content.

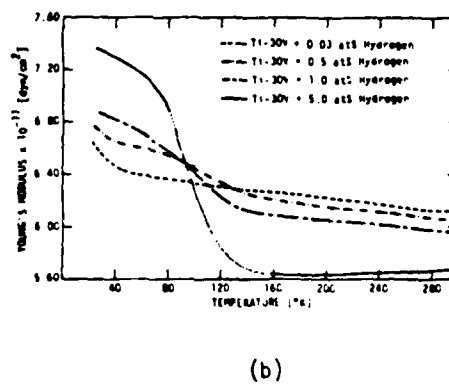
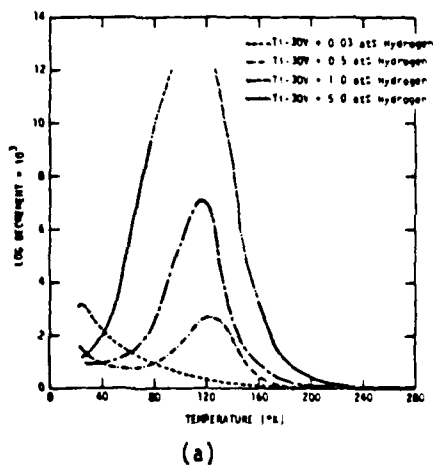


Fig. 4 (a) The logarithmic decrement, and (b) Young's modulus of Ti-30V as a function of temperature and hydrogen content.

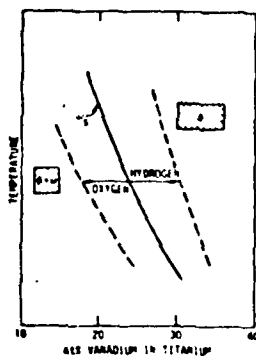


Fig. 5 The omega start temperature as a function of alloy composition (schematically).

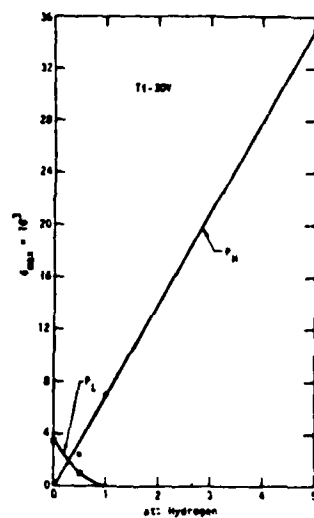


Fig. 6 The heights of the internal friction peaks P_L and P_H , respectively, for Ti-30V as a function of hydrogen content.

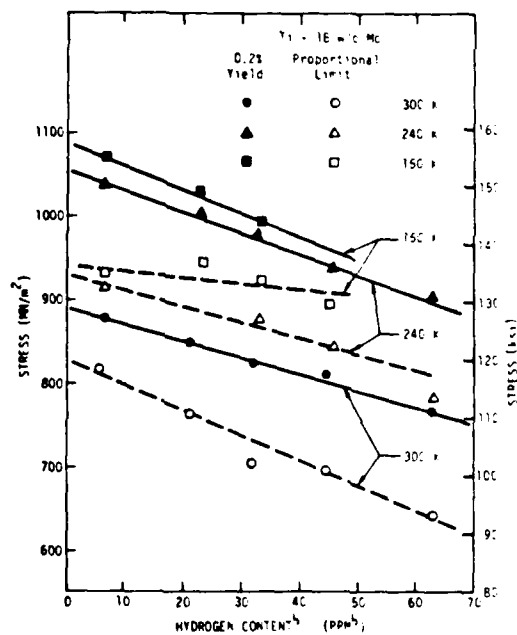


Fig. 7 Yield stress and proportional limit of Ti-18Mo-H alloys plotted versus square root of hydrogen concentration.

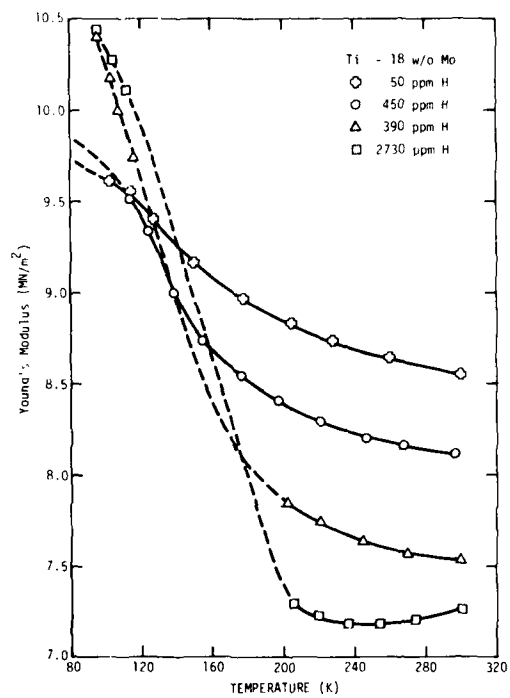


Fig. 8 Young's modulus of Ti-18Mo-H alloys plotted versus temperature.

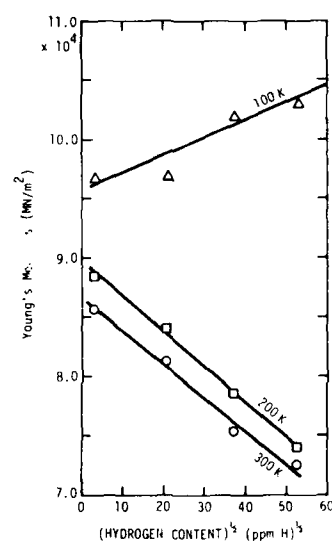


Fig. 9 Young's modulus data from Fig. 8 replotted versus square root hydrogen concentration.

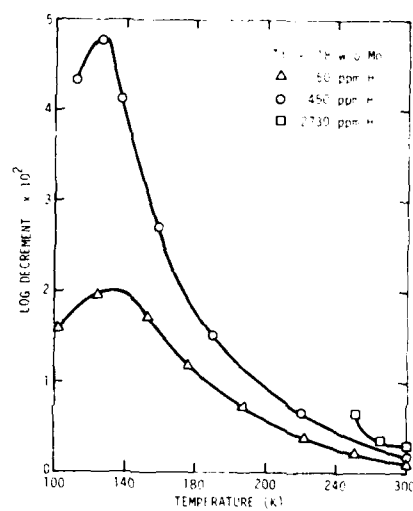


Fig. 10 Internal friction logarithmic decrement versus temperature at three different hydrogen concentration.

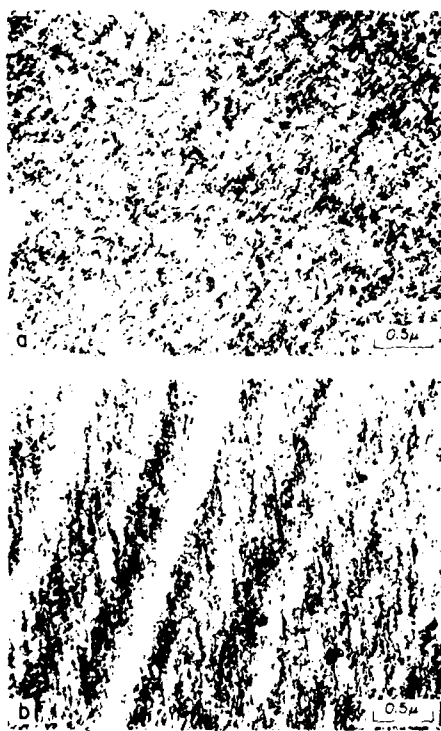


Fig. 11 Slip morphology in Ti-18Mo-H
alloys after 3% strain at
300K
(a) 50 ppm H₂
(b) 500 ppm H₂.

METHODS FOR DETERMINING INTERSTITIAL OXYGEN IN TITANIUM ALLOYS --- TRANSPARENCY SYNOPSIS

J. M. LaGrotta

*Pratt and Whitney Aircraft
Middletown, Connecticut*

A degradation in mechanical properties due to interstitial gas contamination in titanium sheet weldments is of concern. In particular, the detection and measurement of interstitial oxygen and other species entrapped by improper welding are subjects for future study. A number of potential nondestructive inspection procedures which can quantify or identify the presence of interstitial oxygen are presented. These procedures, based on chemical, X-ray, and acoustic phenomena, offer the potential for quantitative detection of interstitials on or near the surface and in the bulk material.

Fig. 1

TITLE

Three novel methods for determining interstitial gas concentrations in Ti alloys are discussed. The techniques used have been demonstrated in the laboratory; however, to date they have not been reduced to practice using the alloy of interest.

Fig. 2

APPROACHES

The three basic approaches are: anelastic damping, x-ray diffraction, and blue-etch anodize. The anelastic damping technique has been shown to be a reliable method for the measurement of interstitial in BCC Ti alloys. To date, an equivalent phenomena has not been identified in HCP alloys; however, some acoustic attenuation and velocity measurements presented at this workshop lend credence to the existence of a relationship.

Fig. 3

X-RAY DIFFRACTION

The work of Clark (1952), et al has shown a direct relationship between interstitial oxygen and nitrogen concentrations and a change in the c lattice parameter in HCP Ti. For the concentration ranges of interest, Dechamps, et al showed that this relationship is quadratic in form.

Fig. 4

X-RAY DIFFRACTION LIMITATIONS

The two primary limitations of an x-ray diffraction measurement to quantify interstitial gas contamination are: First, the technique is limited to measurement near the surface. This limitation does not appear to be significant since previous studies have indicated a nominally uniform contamination throughout the weld. Second, the impact of variations of other substitutional alloying elements has not been quantified for the alloy interest.

Fig. 5

BLUE-ETCH ANODIZE - PROCESS

The blue-etch anodize process consists of several steps: An initial cleaning in a degreasing solution (not shown); a pre-etching of the component (left); anodize (center); controlled stripping of the anodize (right) and a series of intermediate water washes (not shown). The technique is currently used on all Ti alloy components at P&WA. Some of the alloys to which blue-etch has been applied include commercially pure Ti, Ti 6-4, Ti 8-1-1, Ti 6-2-4-6, and others.

Fig. 6

BLUE-ETCH ANODIZE - CLASSICAL FORGING DEFECTS

Blue-etch anodize has been shown to be a very effective means for identifying traditional forging defects. These defects are usually associated with regions of high oxygen contamination.

Fig. 7

BLUE-ETCH ANODIZE - ALLOY SEGREGATION

Blue-etch anodize has been used to identify alloy segregation in Ti alloys. Some types of segregation that can be identified are alpha case, high aluminum content, beta segregation, and Type I alpha segregation.

Fig. 8

BLUE-ETCH ANODIZE - LIMITATIONS

Blue-etch anodize is a surface inspection technique. Current implementation requires immersion of components, although parts as large as 4 feet in diameter can be inspected. For very large components, an alternative swabbing technique would have to be developed. At the present time, the technique is comparative, and further effort is required to quantify the results.

NON-DESTRUCTIVE METHODS FOR INTERSTITIAL GAS DETECTION IN TITANIUM ALLOYS

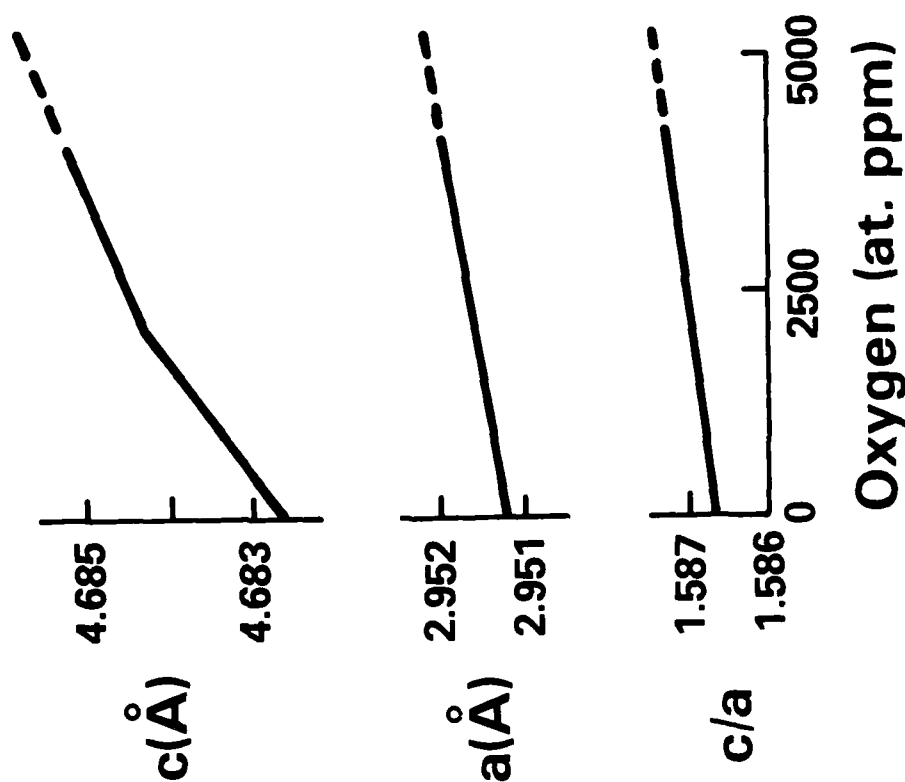
FIGURE 1

APPROACHES

- **Anelastic damping**
- **X-ray diffraction**
- **Blue etch anodize**

FIGURE 2

LATTICE PARAMETERS IN H.C.P. Ti WITH INTERSTITIAL O



After Dechamps et al.

FIGURE 3

X-RAY DIFFRACTION POTENTIAL LIMITATIONS

- Surface connected
- Impact of substitutional alloying elements unknown

FIGURE 4

BLUE ETCH PRINCIPLES



Etch



Anodize



Strip

FIGURE 5

TYPICAL DISCONTINUITIES

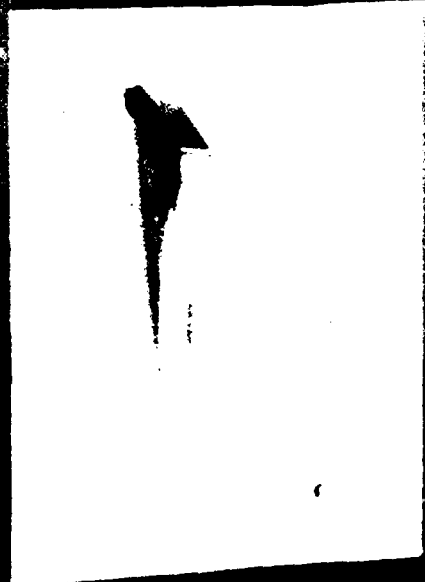
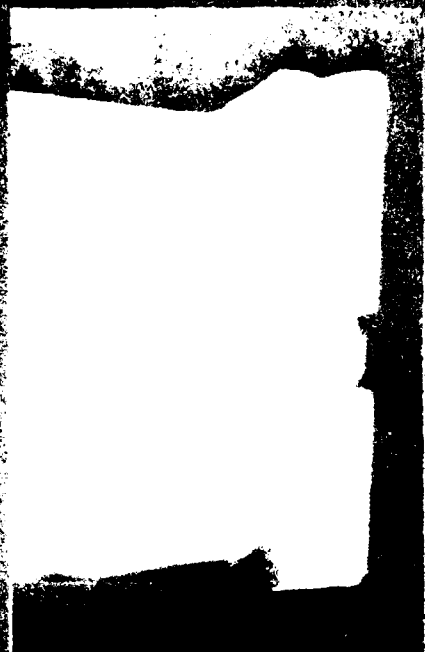


FIGURE 6

BLUE ETCH INDICATIONS

Normal

Alpha segregation

Type I

High Al

Alpha
phase

FIGURE 7

BLUE ETCH ANODIZE CURRENT LIMITATIONS

- **Surface connected**
- **Requires immersion of components**
- **Comparative method**

FIGURE 8

DEFECT CHARACTERIZATION IN TITANIUM ALLOY USING ULTRASONIC SPECTROSCOPY

Laszlo Adler and Dale Fitting

*Department of Welding Engineering
Ohio State University*

Ultrasonic spectroscopy is the study of ultrasonic waves resolved into their Fourier frequency components. In the applications of ultrasonic spectroscopy to Nondestructive Evaluation of defects, the amplitude and phase spectra of broadband ultrasonic waves scattered from the defect is strongly dependent on geometrical and surface characteristics of the defect. An ultrasonic spectroscopy system will be presented with experimental and theoretical results on characterization of cavities and cracks in titanium alloy.

EXPERIMENT

Experimental system. The present configuration of the Ultrasonic data acquisition and processing system is illustrated in Fig. 1. The SCR pulser produces a fast rise-time high voltage (162 volts) negative spike with an exponential return to zero. This wide band electrical pulse excites an untuned, highly damped ceramic transducer with center frequency of 10 MHz. The ultrasonic pulse (pulse length ~ 1 usec) which is produced contains a broad band of frequencies. Ultrasound scattered by the target is received by either (1) the transmitting transducer (pulse-echo) or (2) a receiving (identical) transducer (pitch-catch). The electrical pulse produced by this receiving transducer is amplified by a wide bandwidth gain stage. A stepless gate is used to select a portion of the received signal for further analysis. Signals falling outside the gated regions are highly attenuated. An oscilloscope displays both the entire receiver output and the section of waveform passed by the gate.

The frequency content of the gated waveform is presented on an analog spectrum analyzer. The gated pulse may also be captured and stored through use of the digital acquisition system. A transient recorder samples the ultrasonic signal at 100 MHz, and stores the amplitude at discrete times in its digital memory. The minicomputer controls the acquisition of the ultrasonic pulse and then transfers the digitally represented signal from the recorder to the minicomputer memory. The signal may also be permanently stored by recording it onto a magnetic tape. Processing of the ultrasonic signal (Fast Fourier Transform, correlation and

deconvolution) is performed on the minicomputer. An electrostatic plotter provides a visual display of pertinent information. For the Fourier Transform both amplitude and phase spectra can be calculated. The digitalized amplitude spectra is checked by the analog spectra throughout the experiment. This system is versatile to use for accurate measurements of velocity, attenuation of ultrasonic waves at various frequencies, and to obtain amplitude and phase spectra of scattered waves from single defect or from surfaces.

FLAW CHARACTERIZATION IN TITANIUM ALLOY

Experimental technique and procedure. The technique used to obtain information from flaws is shown in Fig. 2. The sample, which is a disk (2.5 x 10 cm) of titanium alloy with flat faces, is immersed in water. The transmitter launches a longitudinal wave to the liquid-solid interface at some angle. For nonnormal incidence both L and T waves are produced in the metal. The cavity can beinsonified either by the L wave or by the T wave with incident angle α . At the cavity the waves are scattered and mode converted. The scattered waves are received and analyzed separately due to their separation in arrival time.

A specially designed goniometer is used (Fig. 3) to mount the transmitter and the receiver. The position of both transmitter and receiver in polar angle can be changed separately. A special feature of the goniometer is its flexibility of keeping the polar angle fixed and varying the azimuthal angle. This latter feature is especially important for elliptical cracks because of the asymmetry in the scattered field along the different axes of ellipse.

Data correction. In order to analyze the experimental results based on the analytical prediction the effect of the transducer and the crack had to be separated. In a linear time invariant system this is done in the frequency domain by dividing the frequency response from a system by the so-called transfer function. In this problem the spectrum of the transmitted signal through the material (without the crack) is considered the transfer function. Fig. 4A shows the RF signal transmitted (normally) through a parallel flat smooth titanium (flawless) disk immersed in water. There is usable energy through the frequency range from 2 to 15 MHz. The amplitude spectrum shown on Fig. 4B is the transfer function of the system. The spectrum of the scattered wave is then divided by this transfer function.

3-Dimensional display of the experimental data. The diffracted waveforms have been processed, stored, and collected from different points in space and displayed in a 3D fashion to obtain an overall view of the diffracted field due to different cracks. Typical displays are shown on Fig. 5 where the diffracted amplitude vs. frequency and azimuthal angle by 15° intervals from major to minor axes is shown. The dimensions of the elliptical crack are $2500\mu \times 1250\mu$. The incident wave is normal to the crack. The polar angles were 52° and 60° . Another feature of the diffracted field is shown on Fig. 6. The amplitude is plotted vs. frequency and polar angle for three cases when the receiver is placed along the minor axis along 45° and along the major axis the polar angles change from 30° to 60° in 5° intervals. The elliptical crack's dimensions are $2500\mu \times 612\mu$. Although these 3D plots are very useful to obtain qualitative features of the diffracted field, the comparison between experiment and theory was carried out in 2-dimensional displays.

On Fig. 7 the experimental data are compared to theory for the $2500\mu \times 1250\mu$ elliptical crack. The data are displayed when the receiver is along the major axis. The receiver's position is such that the polar angle is 60° . The agreement with theory is very good for the periodicity but the measured amplitudes are lower at high frequencies than predicted by theory, without attenuation. With attenuation correction the agreement between theory and experiment is further improved.

CHARACTERIZATION OF WELDS

The flaw characterization process by ultrasonic spectroscopy requires the knowledge a priori of the wave propagation velocities and attenuation

coefficient. For an austenitic weld both these parameters are directional dependent caused by the preferred local orientation of elongated subgrains. Such a structure is shown on a macrograph on Fig. 8 for an austenitic stainless steel weld. The apparent symmetry in the macrostructure suggested to assume an Orthorhombic symmetry which describes the stress-strain relationship with 9 elastic constants. The relationship between ultrasonic velocity and elastic constants for Orthorhombic symmetry is shown on Table 1.

Table 1. Relationships Between Elastic Constants and Ultrasonic Propagation Velocity for Orthorhombic Symmetry

Propagation Direction	Elastic Stiffness Relations ^a
1 axis	$C_{11} = \rho V_{11}^2, C_{22} = \rho V_{22}^2, C_{33} = \rho V_{33}^2$
2 axis	$C_{11} = \rho V_{11}^2, C_{22} = \rho V_{22}^2, C_{33} = \rho V_{33}^2$
3 axis	$C_{11} = \rho V_{11}^2, C_{22} = \rho V_{22}^2, C_{33} = \rho V_{33}^2$
1 axis (Rotation around 3)	$C_{11} = l^2 m^{-1} [(l^2 C_{11} + m^2 C_{22} - \rho V_{11}^2)(l^2 C_{22} + m^2 C_{33} - \rho V_{11}^2)]^{1/2} - C_{22}$
2 axis (Rotation around 1)	$C_{22} = m^2 n^{-1} [(m^2 C_{11} + n^2 C_{22} - \rho V_{22}^2)(m^2 C_{22} + n^2 C_{33} - \rho V_{22}^2)]^{1/2} - C_{33}$
3 axis (Rotation around 2)	$C_{33} = n^2 l^{-1} [(n^2 C_{11} + l^2 C_{22} - \rho V_{33}^2)(n^2 C_{22} + l^2 C_{33} - \rho V_{33}^2)]^{1/2} - C_{11}$

^aThe first subscript on V indicates the direction of propagation and the second subscript indicates the polarization; e.g., V_{31} represents shear velocity propagating in the 3-direction and polarized along the 1-direction. Once the elastic constants are calculated from the relations above, the last three equations can be solved to calculate the variations of the velocities as a function of orientation.

A technique was developed to measure variation of velocities with direction in structured materials is shown on Fig. 9. A sample, which is a cylinder, is mounted from a goniometer which can be slowly rotated about its axis. The sound is transmitted through a fixed path from transmitter to receiver. The through transmitted signal is displayed on an oscilloscope and the variation of velocity is measured by measuring the shift of the transmitted signal. The system is calibrated for alignment using an aluminum cylinder. This technique detects velocity variation which is on the order of 1%.

Three cylindrical samples used to measure the velocity with orientation in weld materials is shown on Figure 10. The three samples are taken out such that their axis are along the 1, 2, 3, axis. respectively. By rotating the

samples about the axis one can obtain continuous data for longitudinal velocity as a function of orientation in the three orthogonal planes; e.g. by rotating the samples about 2 axis one can obtain not only V_{11} and V_{33} but also V_{33} (see Table 1) which is important to have in order to calculate the elastic constant. A cubical sample has been also taken out from the weld and contact longitudinal and shear measurements were also used to correlate with relative velocities determined from the cylindrical samples. Typical data for an electrosag single pass austenitic weld is shown on Fig. 11 in polar plots. The solid curve is theoretical and obtained by solving the equation from Table 1 for the velocities. The defect characterization in a weld material will be required to obtain information about the anisotropy of the weld before the technique described in previous sections can be applied successfully.

REFERENCES

1. Adler, Laszlo and Achenbach, Jan D., "Elastic Wave Diffraction by Elliptical Cracks: Theory and Experiment," Journal of Nondestructive Evaluation, 1(2), 87-99 (1980).
- Dewey, B.R., Adler, L., King, R.T., and Cook, K.V., "Measurements of Anisotropic Elastic Constants of Type 308 Stainless-steel Electrosag Welds," Experimental Mechanics, 17(11), 420-426 (Nov. 1977).

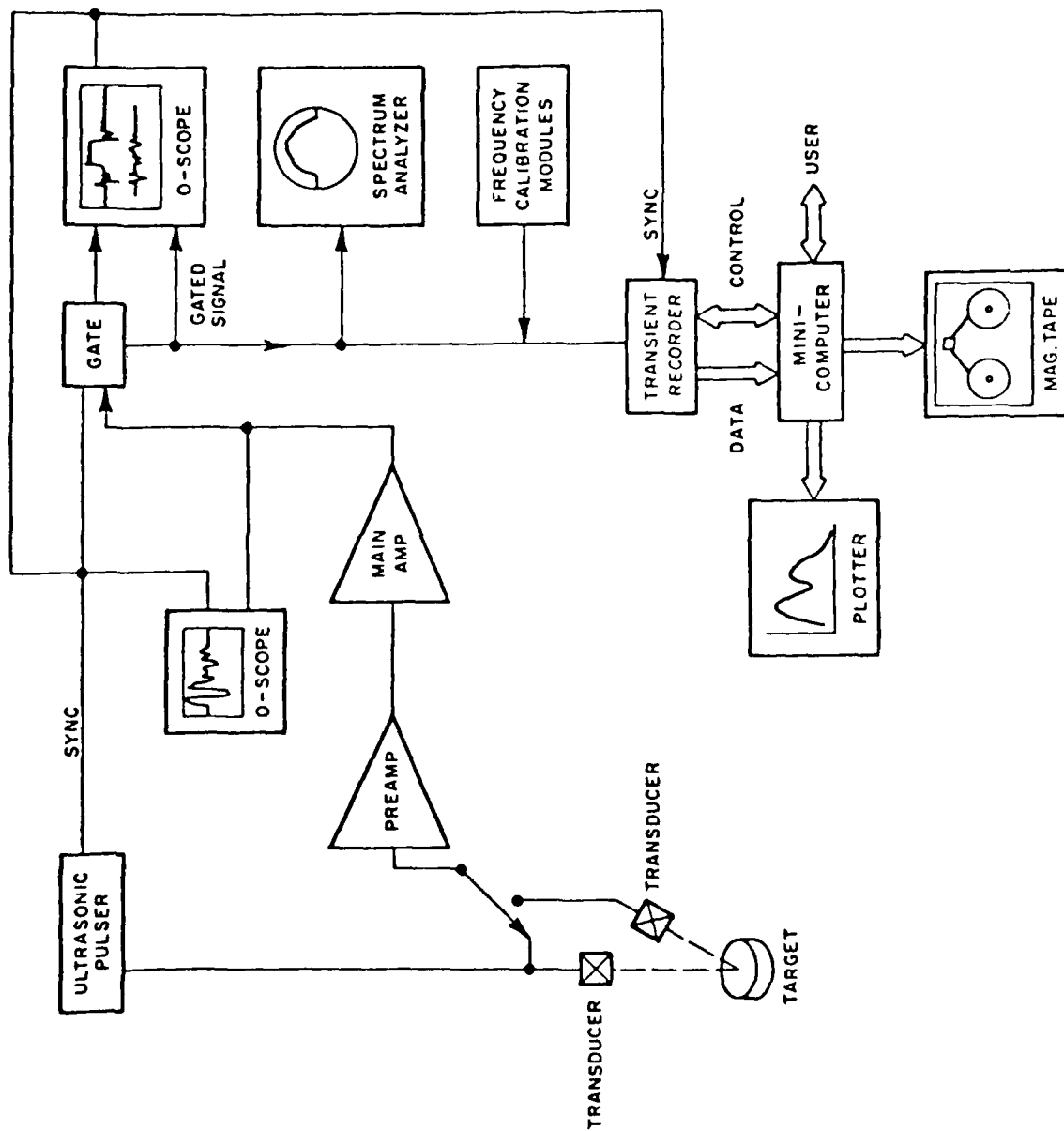


Figure 1. Experimental System.

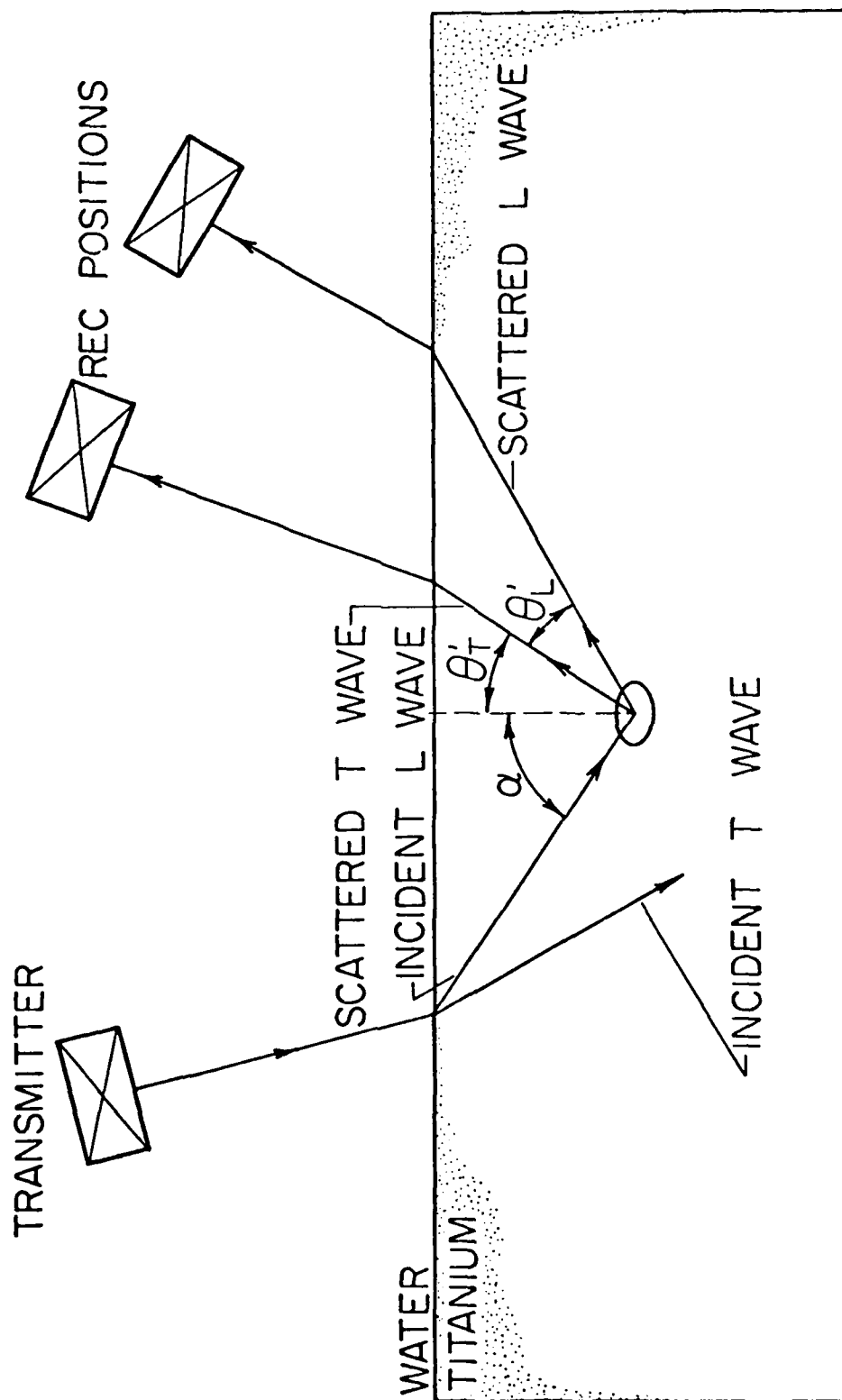


Figure 2. Experimental Technique.

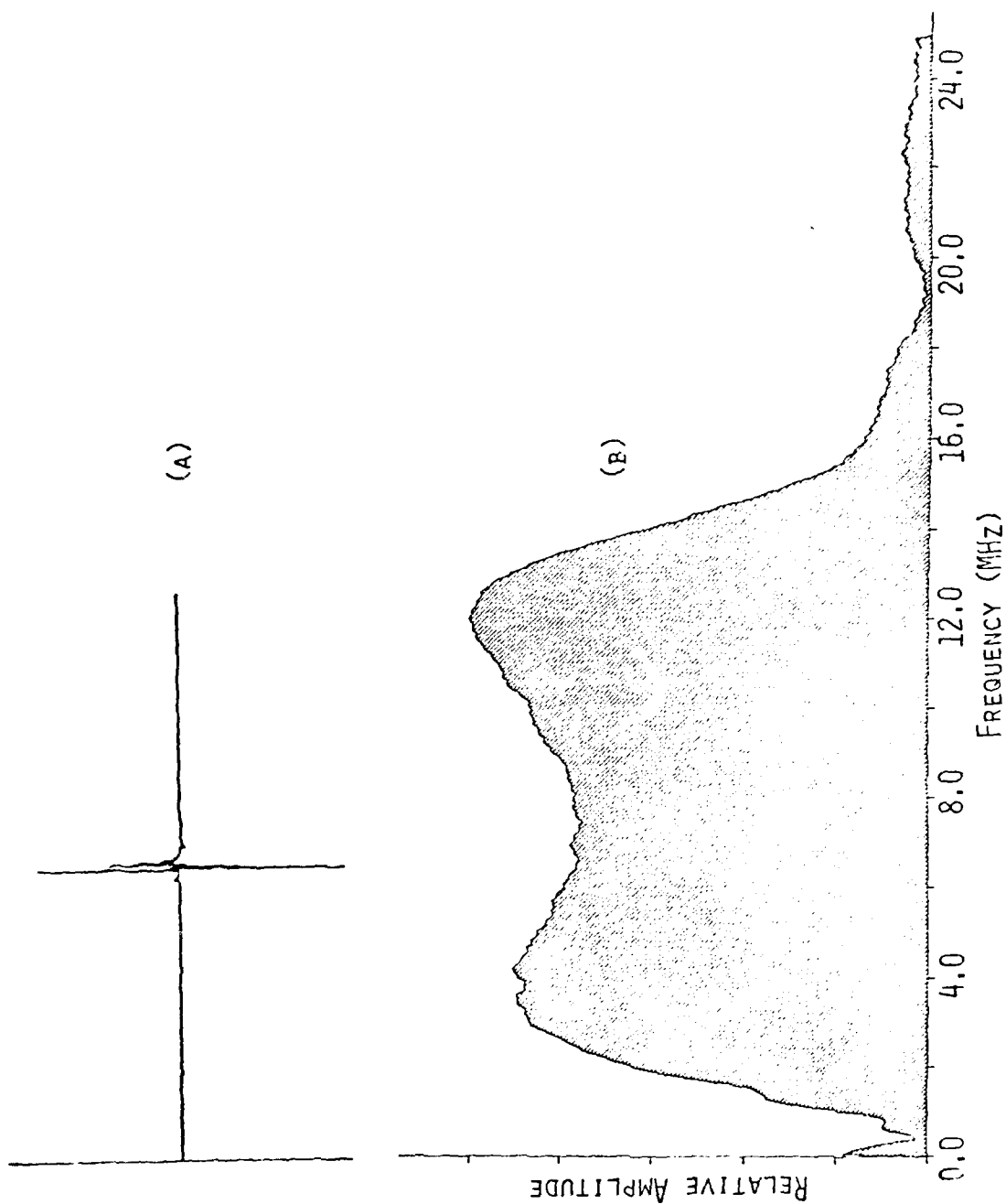


Figure 4. Transfer function. (A) RF signal; (B) Amplitude spectrum.

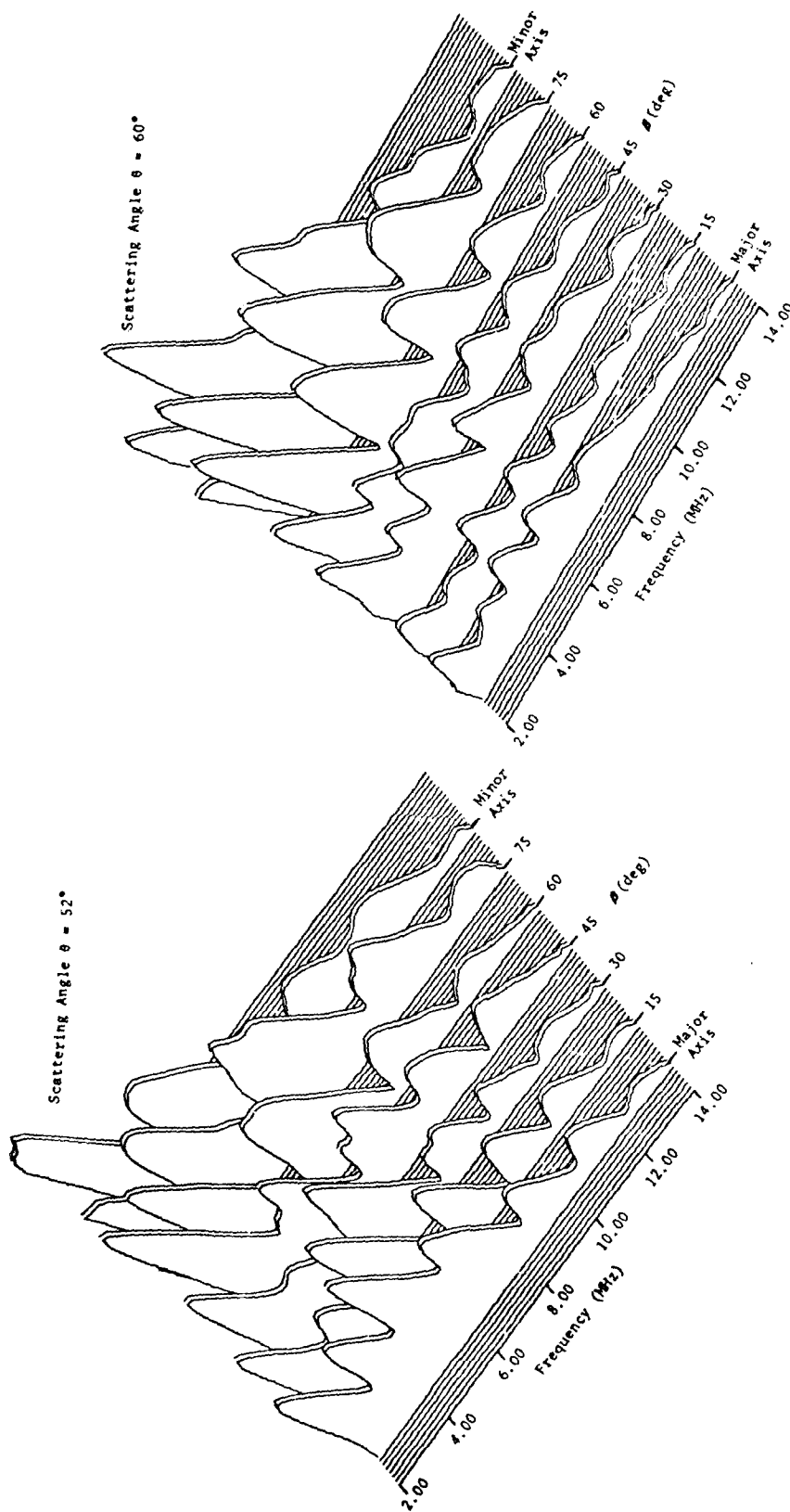


Figure 5.- Experimental amplitude spectra of normal incidence L wave scattered from a $2500\mu \times 1250\mu$ elliptical crack in titanium.

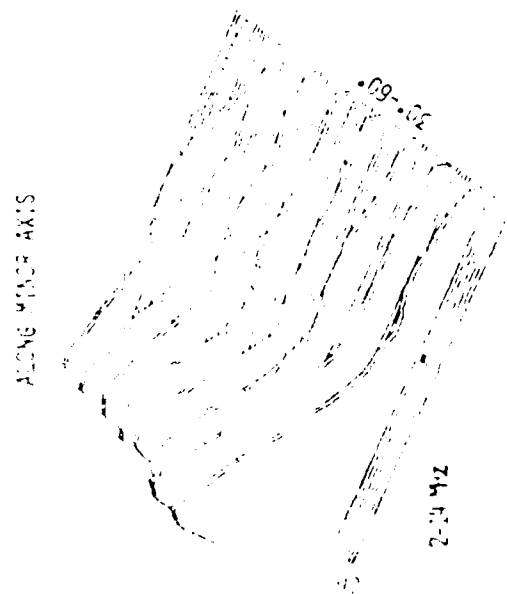
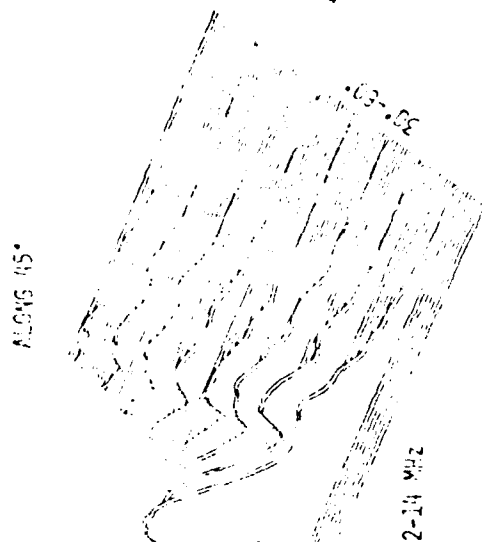
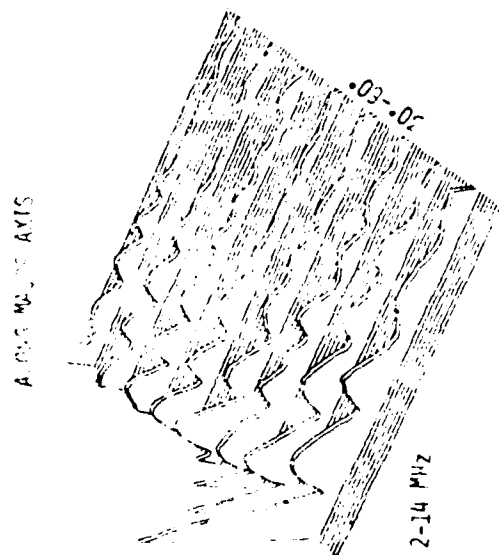


Figure 5. Experimental data for L-1 scattering from a $2500\mu \times 625\mu$ elliptical crack.

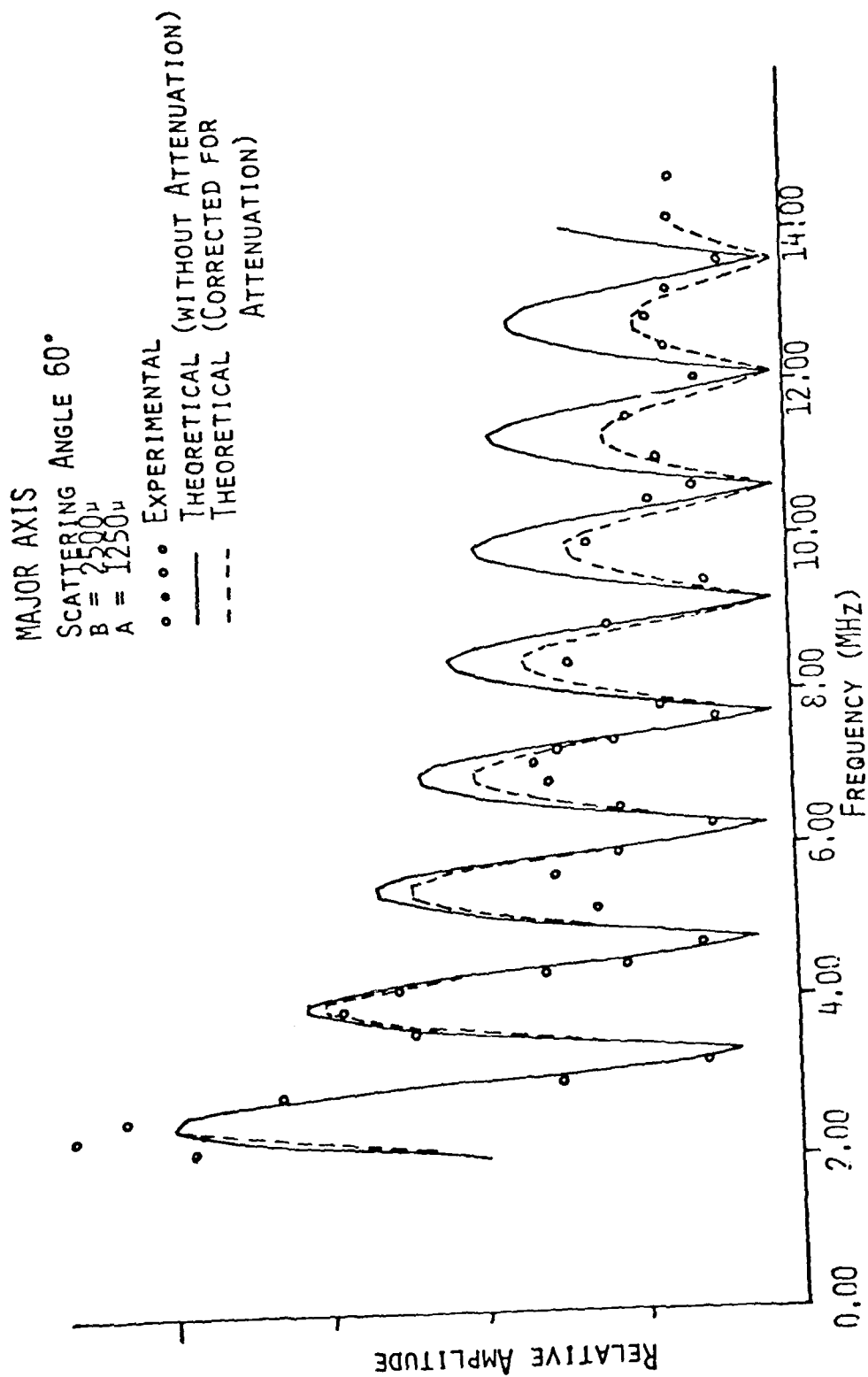


Figure 7. L-L scattering from an elliptical crack with attenuation correction.



Figure 8. Macrograph of an Austenitic Weld.

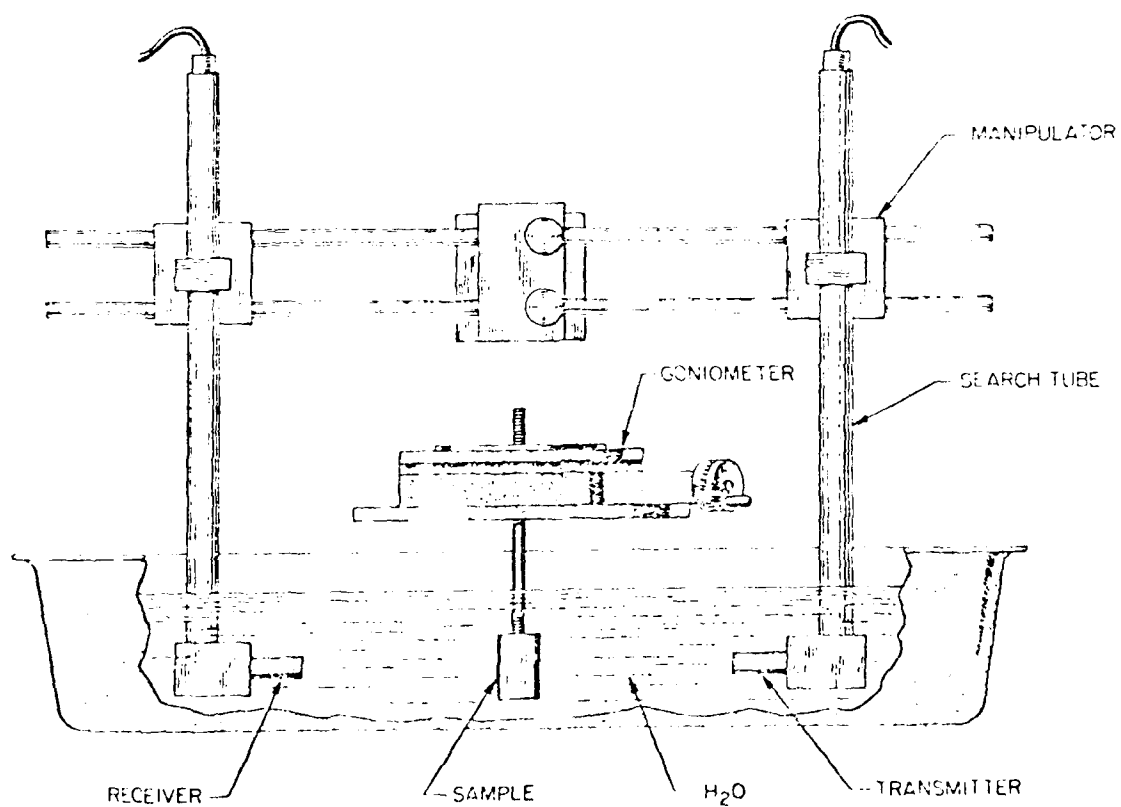


Figure 9. Apparatus to Measure Velocity Variations

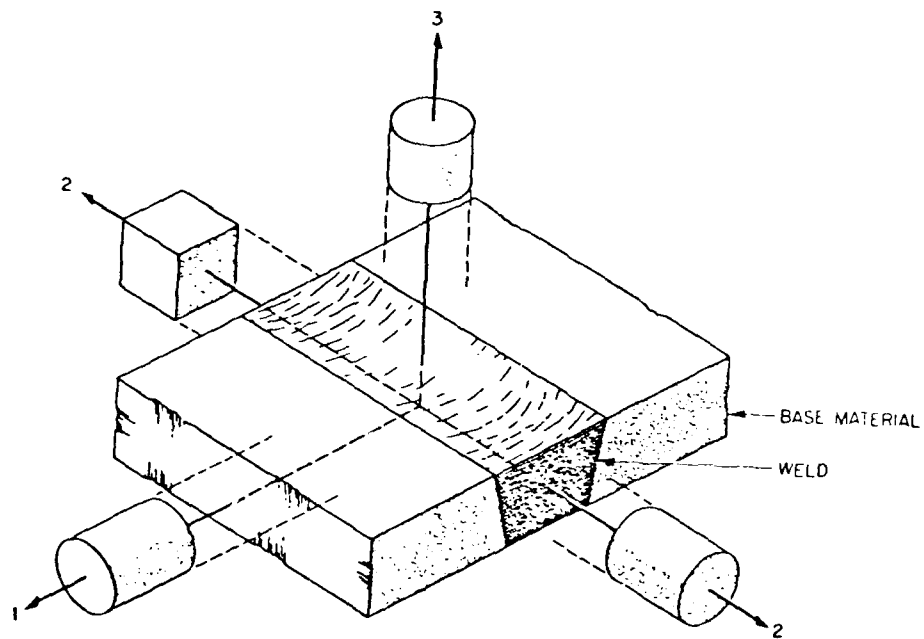


Figure 10. Sample Selection from a Section of Weld for Ultrasonic Studies.

AD-A119 066

NAVAL RESEARCH LAB WASHINGTON DC
PROCEEDINGS OF THE FIRST WORKSHOP ON NONDESTRUCTIVE EVALUATION --ETC(U)
JUN 82 O P ARORA, H H CHASKELIS, N K BATRA

F/8 11/6

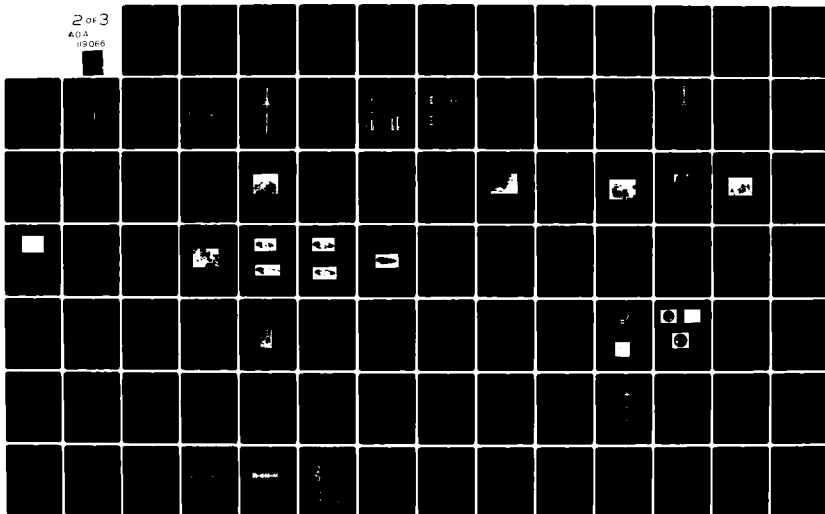
UNCLASSIFIED

DTNSRDC/SME-CR-14-82

NL

2 of 3

A.O.A.
119066



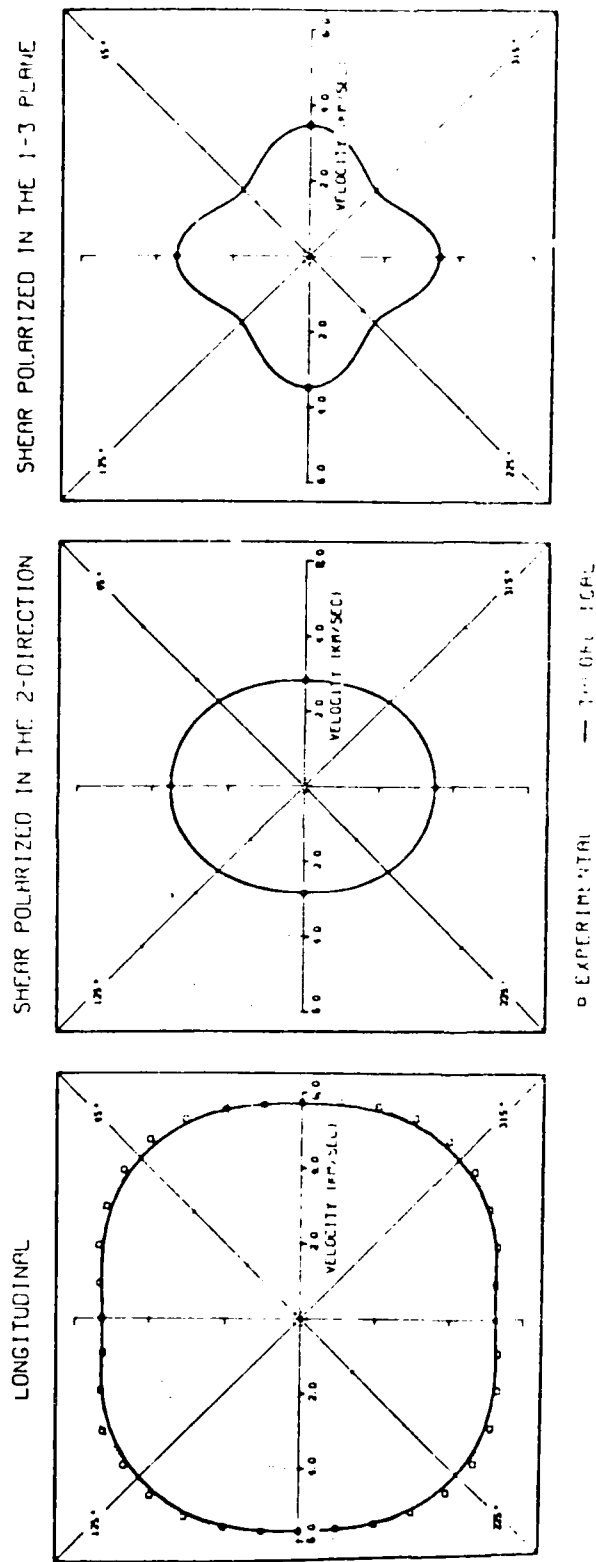


Figure 11. Variation of Velocity with Orientation in an Austenitic Weld.

NONDESTRUCTIVE EVALUATION OF BULK RESIDUAL STRESSES USING ULTRASONIC TECHNIQUES

Kamel Salama

*Mechanical Engineering Department
University of Houston
Houston, Texas 77004*

The presence of residual stresses in titanium weldments plays an important role in determining the behavior of the component and the weld when they are subjected to service loads and environment. In addition, the residual stress distribution in the welds affects the growth rate and frequency of formation of stress induced cracks. For these reasons, most of titanium weldments are stress relieved after welding to prevent welding cracks and susceptibility to stress-corrosion cracking in service. In some titanium alloys, however, tests should be conducted to make certain that stress relieving does not reduce fracture toughness, creep strength or other mechanical properties. Only in the case of surface stresses, can nondestructive evaluation of residual stresses be performed by the x-ray diffraction method. Ultrasonic methods appear to hold the best promise in the determination of bulk residual stresses in crystalline and noncrystalline solids. There are four methods which utilize ultrasonic techniques for the non-destructive evaluation of bulk residual stresses. All these methods are based on the anharmonic properties of solids which have been proven to be sensitive to residual stresses. These methods as well as the recent developments in their applications will be reviewed and discussed in order to determine their suitability to the nondestructive evaluation of residual stresses in titanium weldments.

RELEVANCE

The presence of residual stresses in titanium alloys and titanium weldments plays an important role in determining the mechanical behavior of the component and the weld. The residual stress distribution in the weld can also affect the frequency of formation of stress-induced cracks and their rate of growth. Flaws formed during welding can grow to critical size when residual stresses or macroscopic stress concentrations are present. The presence of these stresses raises the stress level around the weld to a value which is equal to that of fracture and leads to premature fracture. The presence of residual stresses can also affect the propagation of cracks when the weld is subjected to fatigue cycling. Tensile residual stresses will open the crack and make propagation easier.

For these reasons as well as others, it is necessary to conduct non-destructive determination of residual stresses when designing for a high degree of reliability. Nondestructive evaluation of residual stresses should also be performed in order to make certain that residual stresses present are within the tolerance of the structure to external loading and do not reduce the fracture toughness of the alloy or the weld. Even after stress relieving, it is highly probable that large portions of

residual stresses remain and influence the calculations for the factor of safety. This consideration will be more true in case of thick and complex geometry sections where regions of high residual stresses are likely to be present. Furthermore, nondestructive evaluation of residual stresses will be extremely necessary when the titanium alloy or weld is contaminated by interstitial oxygen or hydrogen. The presence of these impurities will reduce the fracture toughness of these materials and will lead to a greater influence of the unrelaxed residual stresses on the reliability of the structure.

NONDESTRUCTIVE EVALUATION METHODS

Only in the case of surface stresses can nondestructive evaluation of residual stresses be performed by the X-ray diffraction method. Although considerably improved in recent years, this method suffers from serious problems which severely restrict its applications. Ultrasonic methods appear to hold the best promise in the nondestructive measurements of bulk residual stresses in materials like titanium alloys and titanium weldments. There are three methods which utilize ultrasonic techniques for the nondestructive evaluation of bulk stresses¹: dispersion, birefringence and temperature dependence of ultrasonic velocity.

DISPERSION

The dispersion method² is based on the relationship between the velocity of ultrasonic waves propagating in the solid and the stress applied. From this expression, the stress acting on the solid can be determined by measuring the change in the velocity, v , from its original value at zero

stress, v_0 , using the relationship

$$\Delta v/v_0 = B(\sigma_1 + \sigma_2) \quad (1)$$

where σ_1 and σ_2 are the principal stresses in the plane normal to the wave propagation direction, and B is the acoustoelastic constant. Values of this constant, however, are not readily available in the literature, and one must calibrate the measurements relative to the particular material being investigated. Development of preferred orientation (texture) during deformation, fatigue or welding can considerably modify the acoustoelastic constants. The calibration is also necessary because the ultrasonic velocity measurements themselves are highly dependent on microstructural features.

BIREFRINGENCE

The birefringence method² is based on the difference in velocity Δv for shear waves propagated normal to the stress axis with polarization parallel, v_{11} , and normal, v_{\perp} , to the stress σ , where

$$v_{11} - v_{\perp} = \Delta v = K(\sigma_1 - \sigma_2) \quad (2)$$

where K is an acoustoelastic constant. The difference in the velocities causes a shift in phase which produces the birefringence. This method has the advantage that it is self-calibrating and one need only measure changes in velocity. However, because the number of fringes which usually forms at the normally used ultrasonic frequencies is very small, the acoustic birefringence method does not have enough sensitivity. The method also suffers from complicated acoustic birefringence patterns which can be formed due to

nonhomogeneous texture across the thickness of the specimen.

TEMPERATURE DEPENDENCE OF ULTRASONIC VELOCITY

Basically, the temperature dependences of the elastic constants of a solid are due to the anharmonic nature of the crystal lattice, and are directly related to the coefficients of higher-order terms in the strain energy function. A measure of the temperature dependence of the ultrasonic velocity can therefore be used to evaluate stresses. Experiments performed on aluminum and copper³, and more recently on type A 533 B steel, have shown that the ultrasonic velocity, in the vicinity of room temperature changes linearly with temperature, and the slope of the linear relationship changes considerably as the amount of applied stress is varied. The results obtained on these metals also show that the relative change in the temperature dependence is a linear function of the applied elastic stress, and is given by,

$$\frac{(dv/dT)_\sigma - (dv/dT)_0}{(dv/dT)_0} = -k\sigma \quad (3)$$

where k is a constant equal to 2.4×10^{-3} , 0.25×10^{-3} or 1.5×10^{-3} per MPa for aluminum, copper or type A 533 B steel respectively.^{4,5}

Measurements made on the same specimens under similar conditions have shown that the slope of ultrasonic velocity vs temperature can be determined with an accuracy of $\pm 2\%$. This quantity yields an accuracy of ± 8 MPa, ± 25 MPa

and 112 MPa in determining bulk stresses in aluminum, copper and type A 533 B steel respectively, using the temperature dependence method. The method was also used to determine the stress distributions generated by an aluminum rod which was shrunk fit into a smaller hole drilled into an aluminum disc. The agreement between hoop stresses measured by the temperature dependence and those calculated was very good.

To my knowledge, no nondestructive measurements of bulk residual stresses have been performed on either titanium alloys or titanium weldments. A study to determine the applicability, the sensitivity and the accuracy of each of the above methods to the nondestructive evaluation of residual stresses in titanium plates and welds would be necessary before a practical program can be recommended. The study should also include the determination of the sensitivity and the accuracy of these methods to changes in bulk residual stresses in these materials due to contamination, stress relieving and thickness. These parameters are extremely important to the effects of residual stresses on both the mechanical and the fracture behavior of materials tested. Finally, it will be valuable to examine the possibility of determining the sign as well as the magnitude of the principal components of the residual stresses present. While tensile residual stresses are important to fracture toughness, compressive stresses have more effects on mechanical behavior.

REFERENCES

1. K. Salama, "New Developments in Measuring Residual Stresses Using Ultrasonic Techniques," reprint of Technical Papers Presented at the 1980 SESA Fall Meeting.
2. M. R. James and O. Buck, "Quantitative Nondestructive Measurements of Residual Stresses," Critical Reviews in Solid State and Materials Sciences, 1980.
3. K. Salama and C. K. Ling, "The Effect of Stress on the Temperature Dependence of Ultrasonic Velocity," J. Appl. Phys. 51, 1505, 1980.
4. K. Salama, C. K. Ling and Jo-Jen Wang, "Measurement of Residual Stress Using the Temperature Dependence of Ultrasonic Velocity," Reprint of Technical Papers Presented at the 1980 SESA Fall Meeting.
5. K. Salama, J. J. Wang and A. L. W. Collins, "Nondestructive Evaluation of Bulk Residual Stresses in Steels," Proc. NDE Symposium, 1981.

ASSESSMENT OF WELD QUALITY USING ACOUSTIC EMISSION AND PHASE-SENSITIVE ULTRASONIC METHODS --- TRANSPARENCY SYNOPSIS

Richard S. Williams

*United Technologies Research Center
East Hartford, CT 06108*

As part of a comprehensive program in quantitative NDE research, UTRC is developing test methods capable of assessing material properties and defects in-situ. Acoustic Emission Weld Monitoring (AEWM) is one such technique that shows considerable promise in this area. It will be the primary purpose of this presentation to discuss the principles involved and the demonstrated and potential capabilities of AEWM. In addition, another new NDE technique under development at UTRC, pulsed phase coherent ultrasonics, will also be briefly discussed.

The AEWM method detects low-level AE generated as a consequence of the formation of defects during melting and subsequent solidification. Micromechanical material changes, such as cracking, plastic flow, dislocation movement, and molten metal flow release acoustic energy. This energy creates a stress wave which propagates to the surface where it is detected with a piezoelectric sensor. The detection of this energy and subsequent signal processing is AE monitoring. AEWM has been applied to a number of weld processes, including Tungsten Inert Gas (TIG), Submerged Arc, Resistance Spot, Electron Beam (EB), Gas Pressure, Electric Resistance, Manual Arc, and Capacitive Discharge Welding. Generally, the more controlled the weld process, the more successful the application of AEWM.

Working with an ultrasonic instrument manufacturer, UTRC has assisted in the development of a pulsed phase coherent ultrasonic system. This approach has shown considerable promise in the inspection of coarse grain structural materials.

Fig. 1

Today's talk will cover two test methods. The first is acoustic emission weld monitoring (AEWM) and the second, phase detected ultrasonics.

Fig. 2

During welding there are a number of potential process variations that will result in acoustic emission sources. This vuegraph lists the weld process variables and the corresponding acoustic emission sources.

Fig. 3

Acoustic emission weld monitoring has been applied to a large number of weld methods. This vuegraph lists some of those methods with the most successful application to date listed first.

Fig. 4

Here is shown the experimental setup typically used for various weld monitoring applications. The acoustic emission sensor may be mounted on either side of the weld, along the weld, or, in some cases, directly on the welding electrode.

Fig. 5

Even a high quality weld will give off acoustic emission during its formation. However, it is possible to differentiate between emissions caused from a good weld and the emissions resulting from the introduction of a defect. This vuegraph shows, on the left, the emissions typical of a good weld. The emissions resulting from the introduction of the defect are shown in the plot on the right.

Fig. 6

Shown here is a block diagram of a typical acoustic emission weld monitoring system. It is important to note the amount of signal processing required necessary for a reliable application. The acoustic emission system must be capable of not only discriminating between extraneous and relevant emission events, but also must be capable of characterizing the acoustic emission source and relating this quantitative information to detect size and/or weld feedback control.

Fig. 7

This is a plot of the output of acoustic emission weld monitoring system. Artificial defects were intentionally induced along the weld at programmed locations. All of the plots in this figure are drawn to a common X-axis indicating the location along the weld in inches. The first four plots, starting from the top, are feature outputs. The fifth plot is the composite decision reached by weighting each of the features in a prescribed manner to determine if a defect was detected or not. The last line is the results of destructive sectioning, confirming the presence of a defect. Note that there is a very good correlation between the AEWM composite decision and the results of the destructive tests.

Fig. 8

This plot is similar to the plot in Vuegraph No. 7, however, different types of defects were induced. In particular a crack was induced in the vicinity of 18 inches from the start of the weld. As before the AEWM system detected all induced defects.

Fig. 9

The previous data has shown the ability of acoustic emission to detect critical defects in the weld. Work is also underway at UTRC to process the arc noise itself. In this case there are many low level events that must be processed. To date, a good correlation has been achieved for the following process variables: arc stability, penetration, puddle size, and shield gas state.

Fig. 10

UTRC has developed in cooperation with MATEC a phase-sensitive ultrasonic instrument. The characteristics of this instrument are listed in this vuegraph.

Fig. 11

This vuegraph shows a block diagram of a phase-detected ultrasonic system. Note that not only are the phase-detected time domain signals available, but also two sample and hold circuits are included to give an analog output proportional to the phase within two adjustable stepless gates. These outputs permit impedance plane plots to be generated.

Fig. 12

An ideal application for phase sensitive ultrasonics is the inspection of ultrasonically noisy materials. This "noise" is caused by scattering at grain boundary sites. This vuegraph shows pictorially the kind of ultrasonic noise encountered in these kinds of inspections. Materials having ultrasonically noisy microstructure include titanium and stainless steel.

Fig. 13

This vuegraph shows the comparison between an ultrasonic amplitude scan and a phase scan of a defect located in a ultrasonically noisy material. Note that there is a substantially improved signal-to-noise ratio for the case of the phase-detected signal.

Fig. 14

Using phase detected ultrasonics is also possible to determine the characteristics of the defect. An example is shown here; the plot on the left is an impedance plane representation of a zero degree orientation flat bottom hole, whereas the plot on the right is a 10 deg flat bottom hole. Note that the shape and the phase angle is considerably different for the two impedance plane plots.

Fig. 15

In conclusion, two techniques have been presented. Acoustic emission weld monitoring for in-process assessment of defects and process abnormalities, and phase sensitive ultrasonics for defect detection and characterization in ultrasonically noisy material.

TODAY'S TALK

- *In-situ* assessment of weld integrity
- Flaw detection and characterization

FIGURE 1

WELD PROCESS

Heat input
Cooling rate
Arc
Chemical
reactions



Cracking
Dislocation movement
Molten metal flow
Molten metal
reactions
Arc stability

ACOUSTIC SOURCES

FIGURE 2

AEWM APPLICATIONS

- **Sub-arc**
- **TIG**
- **Resistance**
- **Manual arc**
- **Capacitive discharge**
- **Electron beam**
- **Laser**

FIGURE 3

AEWM EXPERIMENTAL SETUP

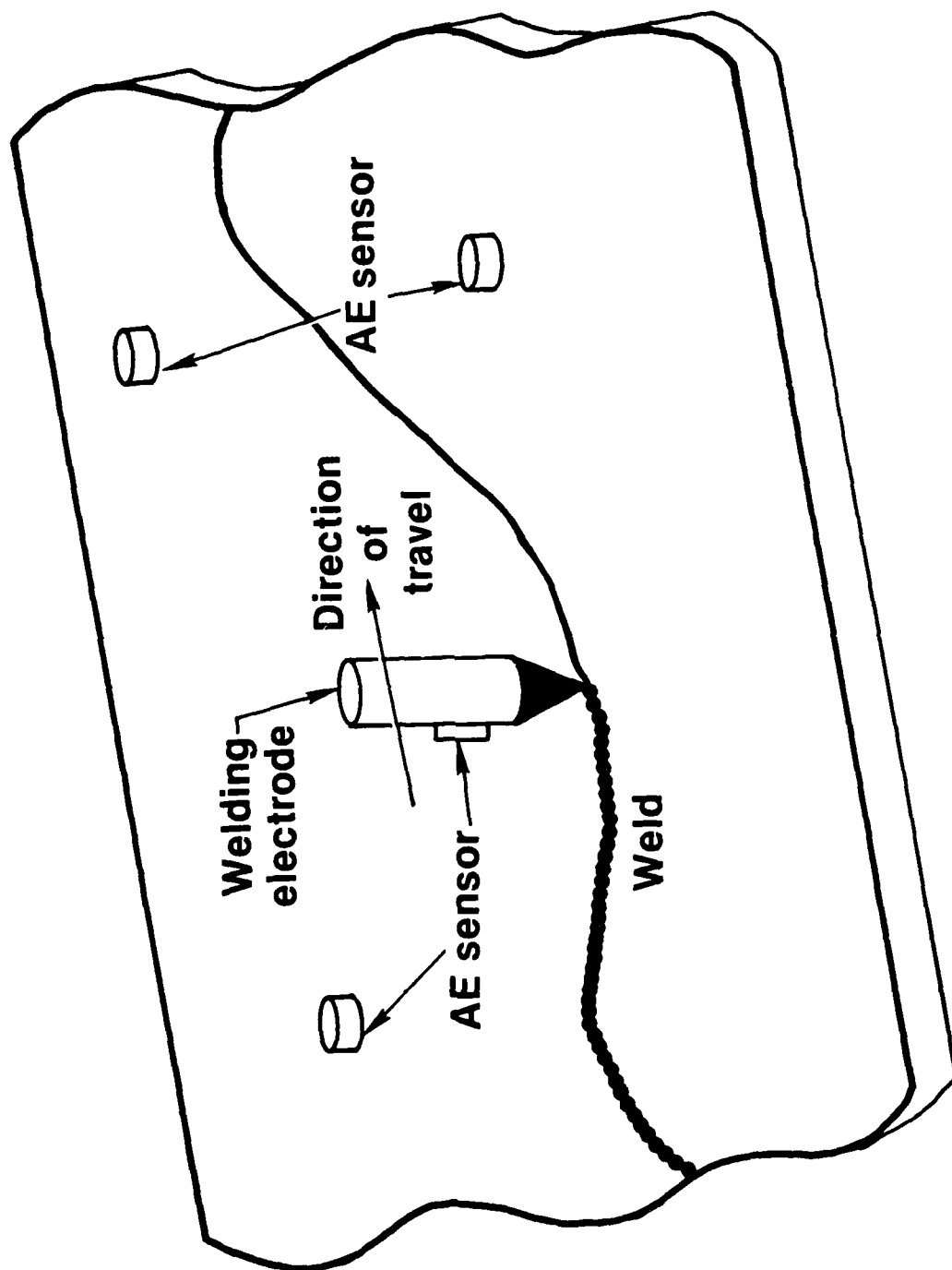


FIGURE 4

AE SOURCES

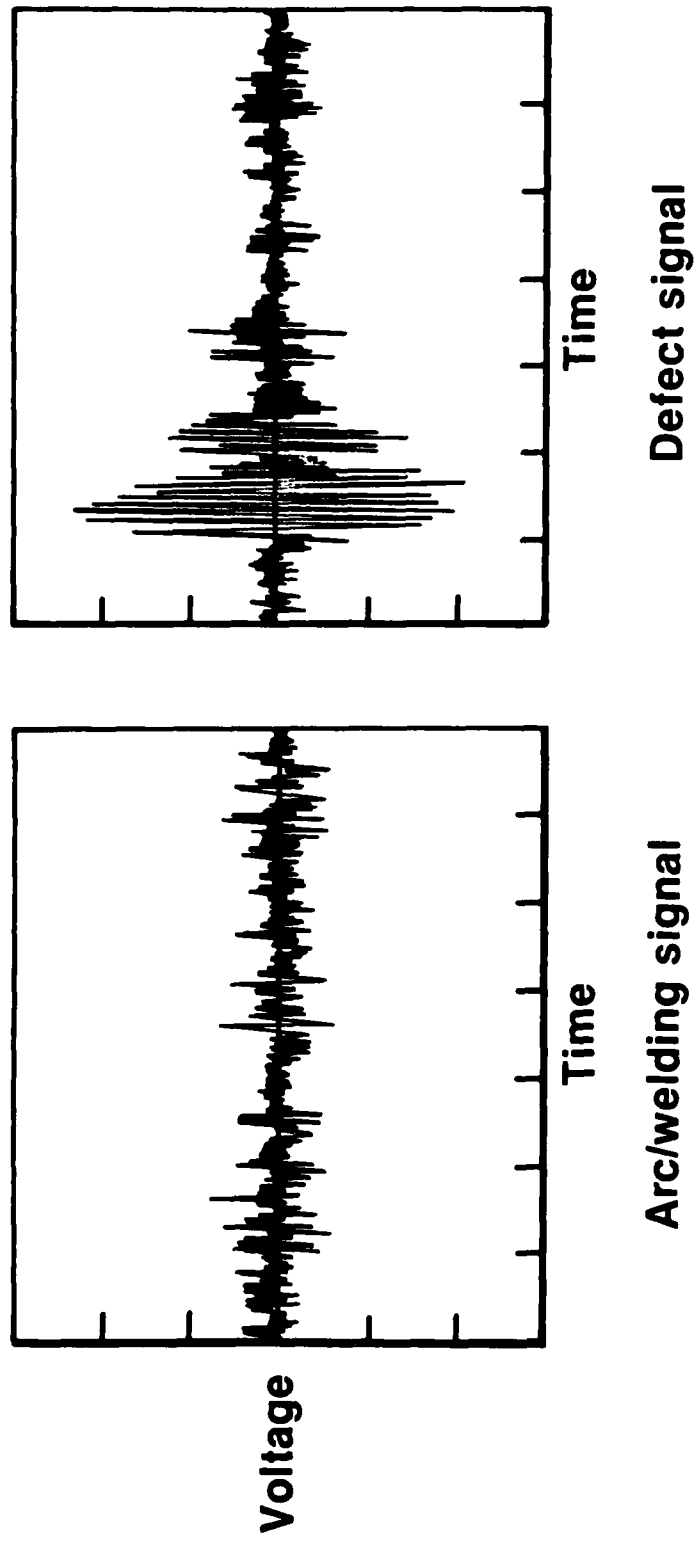


FIGURE 5

AEWM SYSTEM APPROACH

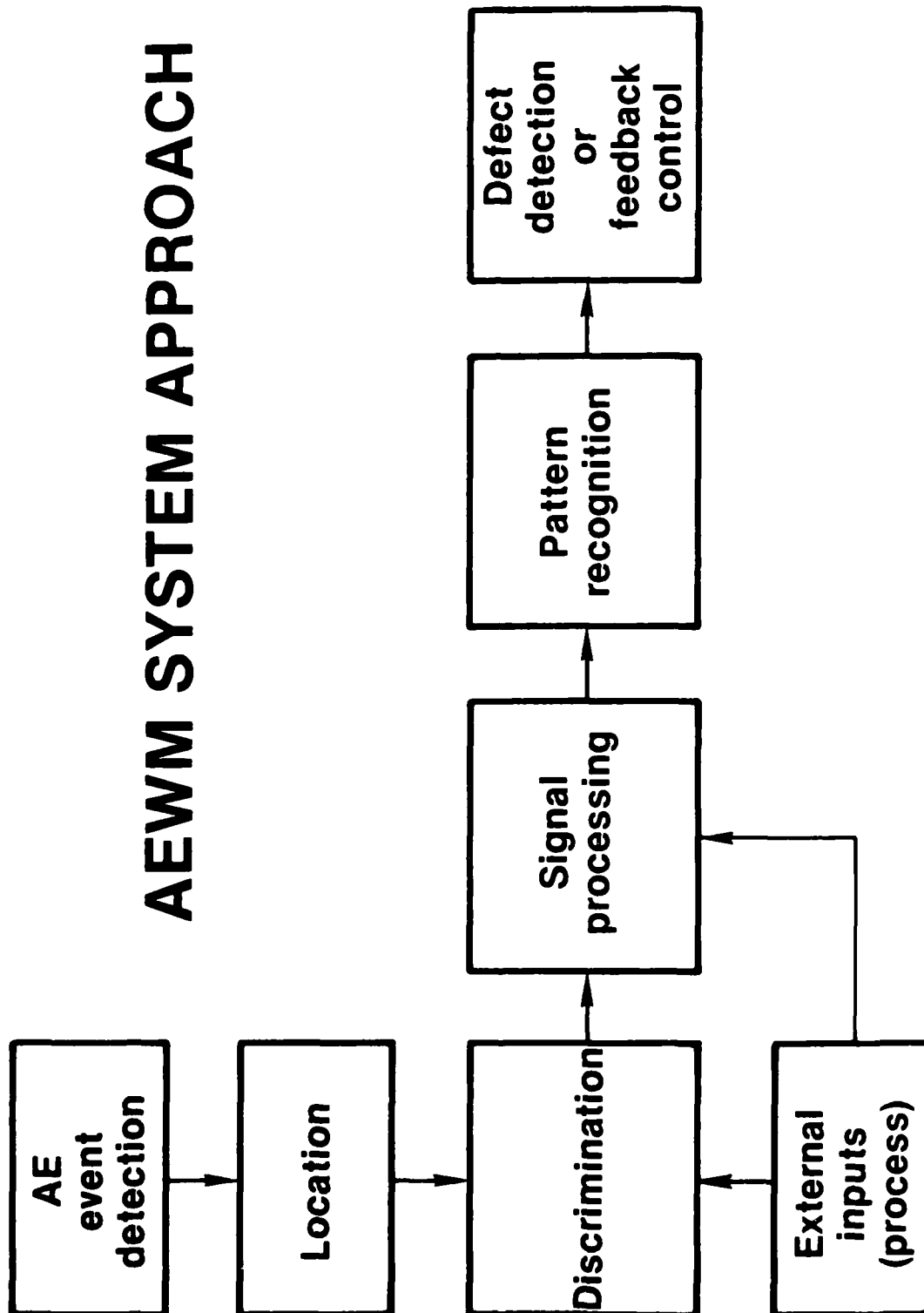


FIGURE 6

AEWM DEFECT DETECTION

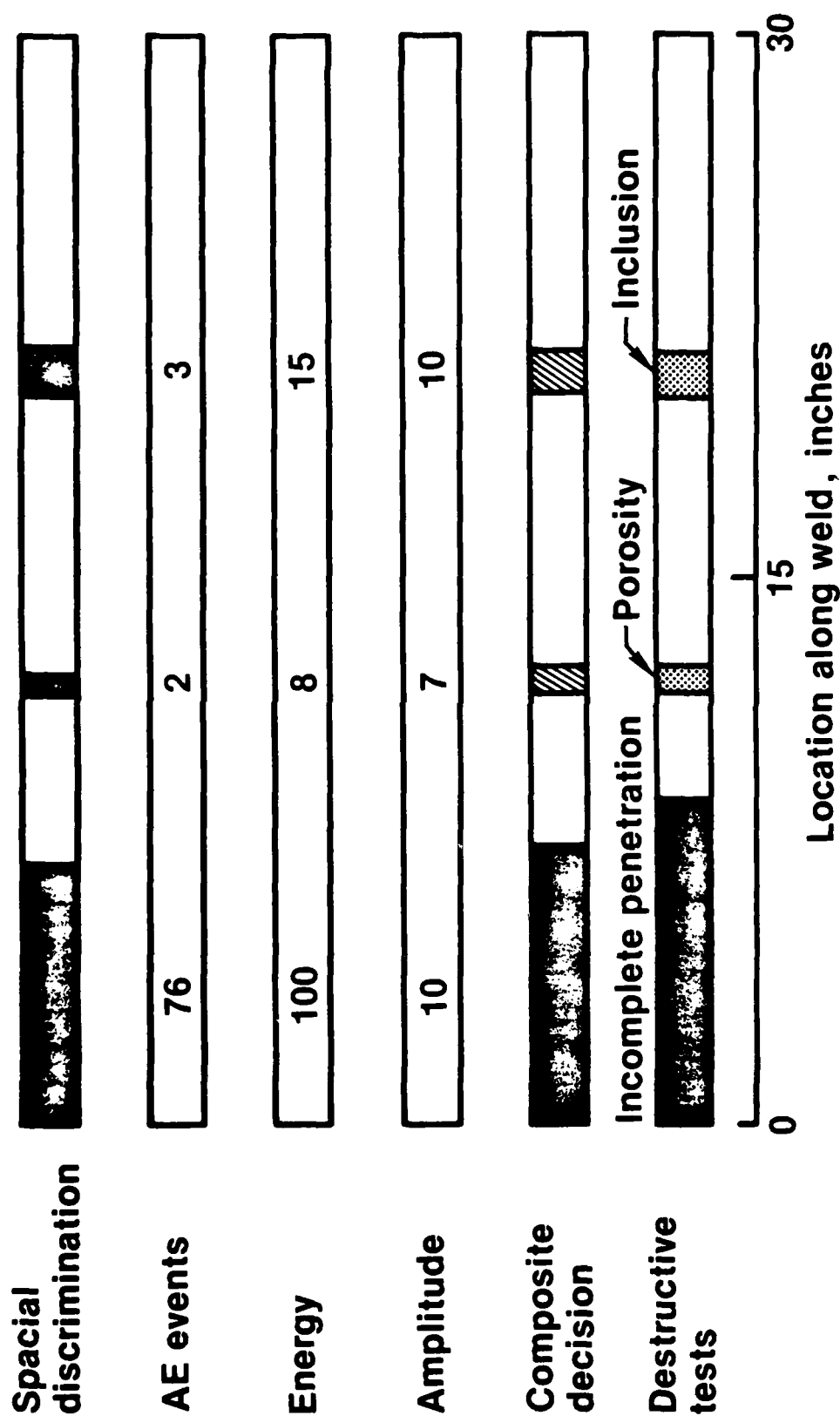


FIGURE 7

AEWM DEFECT DETECTION

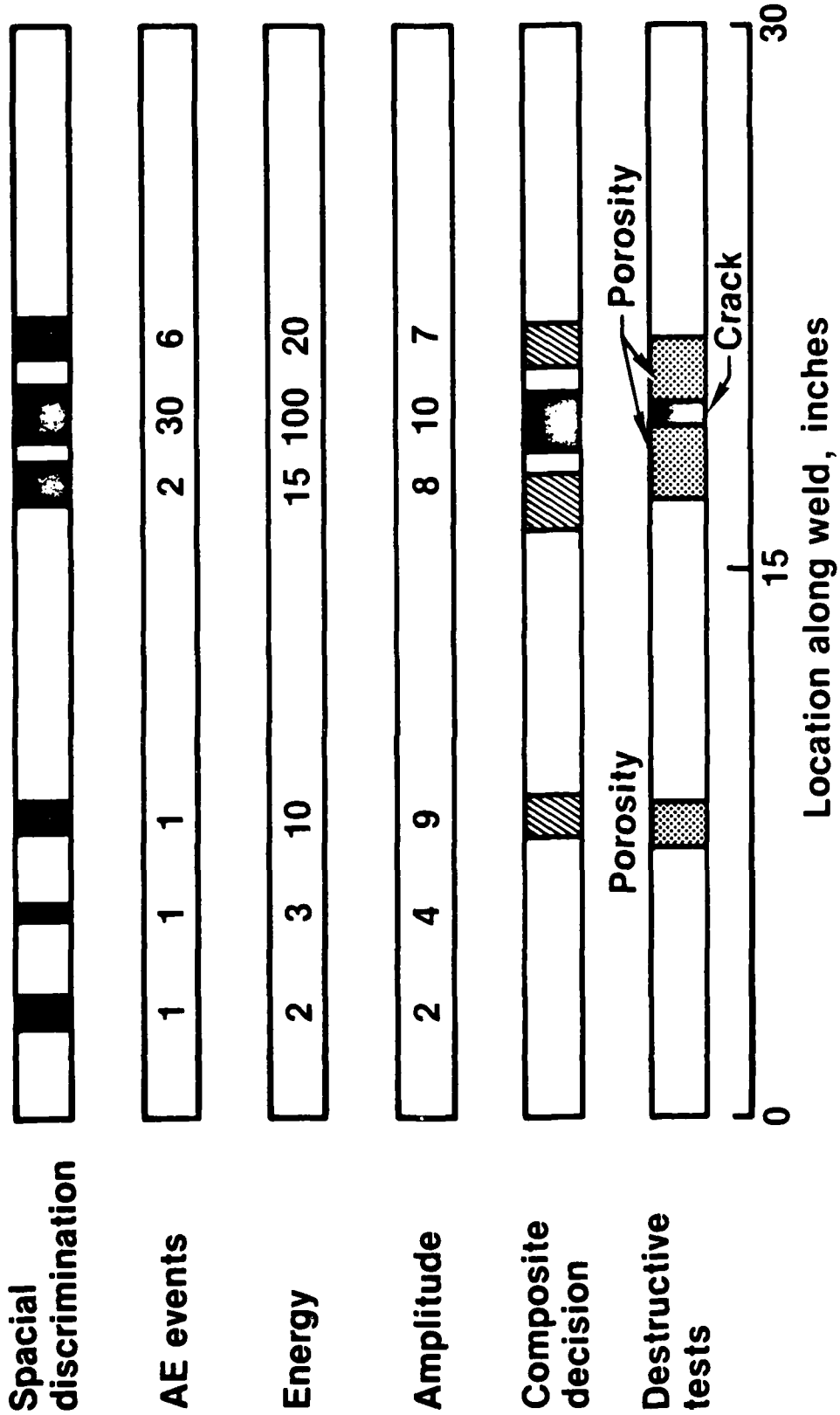


FIGURE 8

AEWM — WELD INTEGRITY

- **Process arc/weld AE**
- **Many low level events**
- **Correlation with**
 - **Arc stability**
 - **Penetration**
 - **Puddle size**
 - **Gas contaminates**

FIGURE 9

PHASE DETECTED ULTRASONICS

- Developed in cooperation with MATEC
- Both amplitude and phase information
- Highly controlled pulser/receiver characteristic
- Frequency ~ 500 kHz to 120 MHz
- Pulser power up to 2000 Watts peak
- Inphase and quadrature outputs for x-y display

FIGURE 10

PHASE DETECTED UT SYSTEM

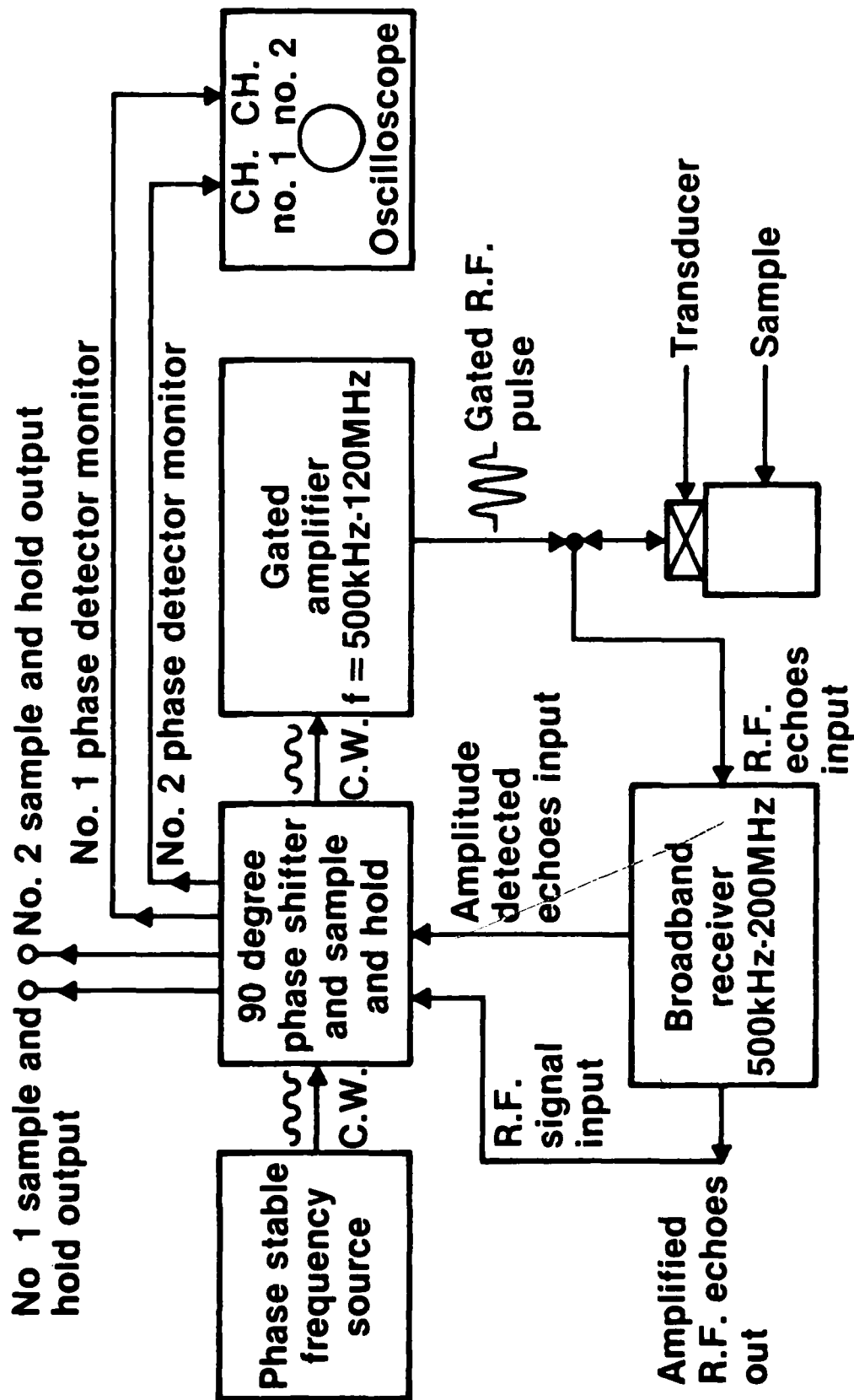


FIGURE 11

INSPECTION OF MATERIAL WITH "NOISY" STRUCTURE

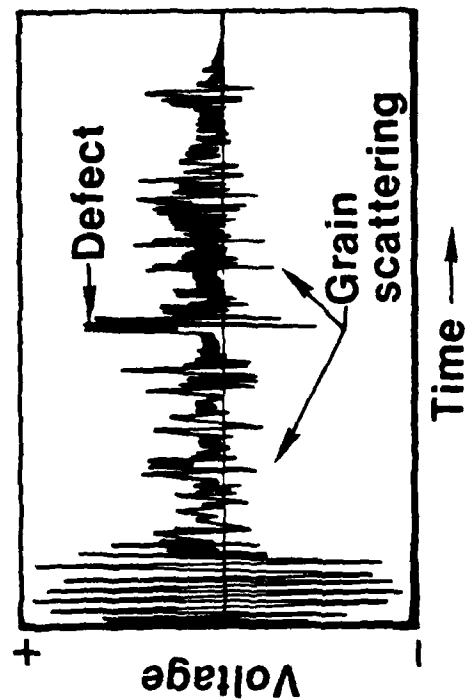
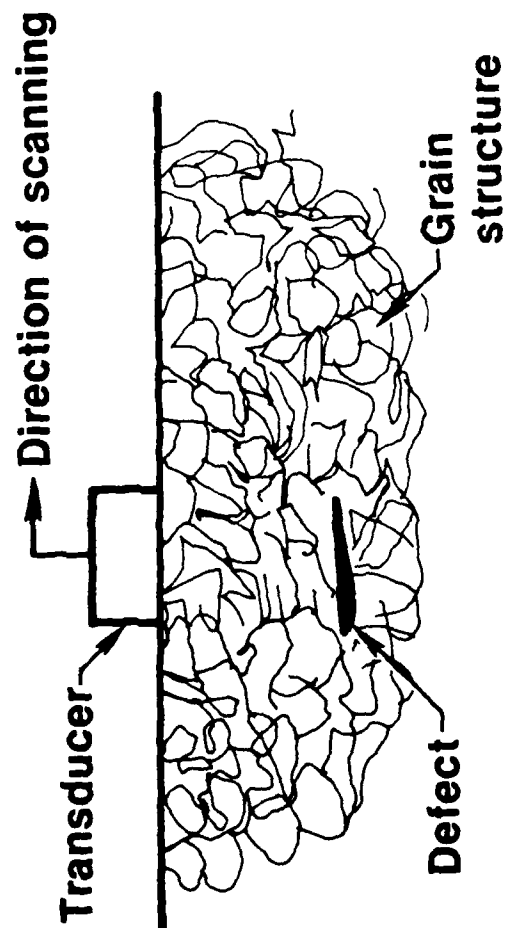


FIGURE 12

TYPICAL PHASE AND AMPLITUDE DATA

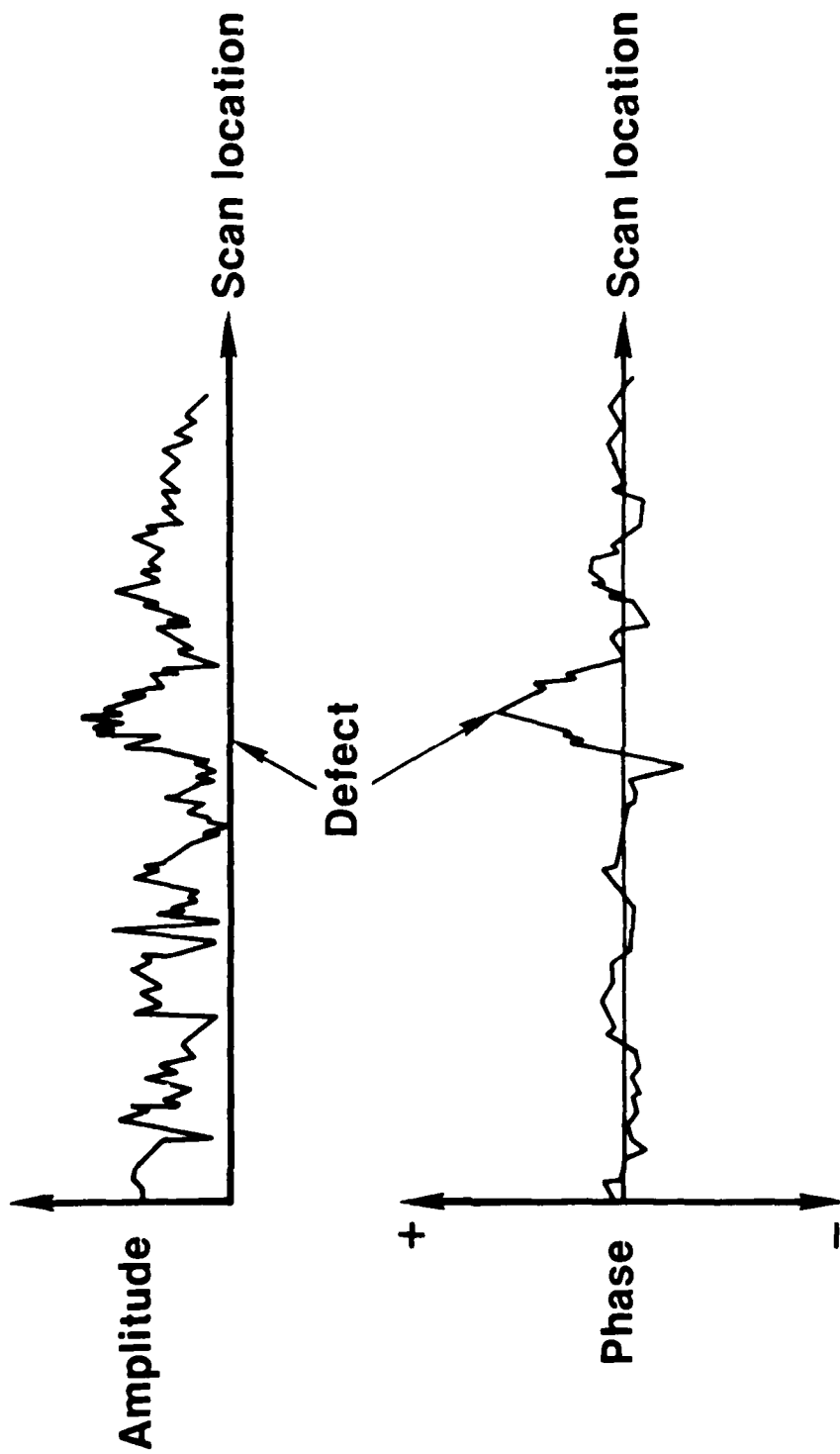


FIGURE 13

IMPEDANCE PLANE PLOTS

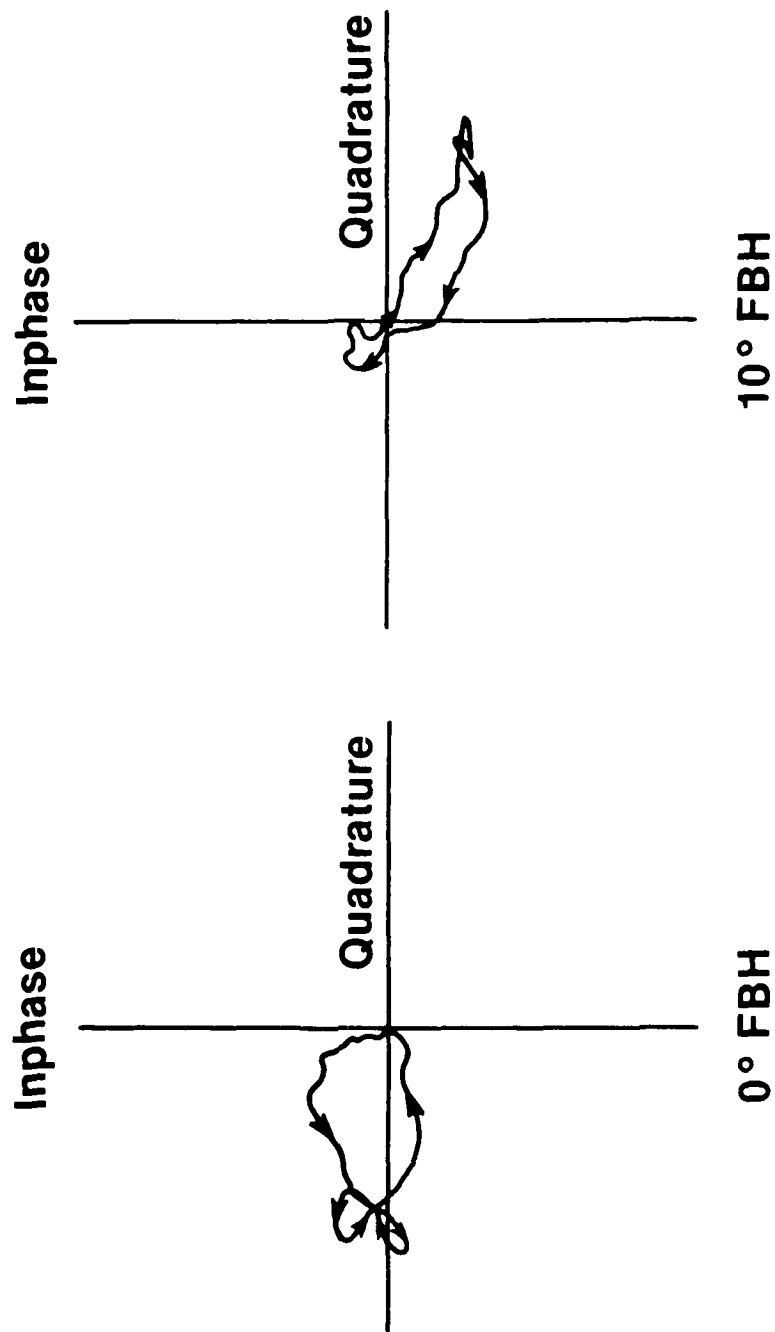


FIGURE 14

SUMMARY

- **AEWM — Weld process assessment**
- **Phase sensitive UT — Defect detection
and characterization**

FIGURE 15

IN-PROCESS WELD MONITORING BY ACOUSTIC EMISSION AND INFRARED IMAGING

W. Lichodziejewski

*Manager, Nondestructive Testing
GARD, Inc/GATX Corp.
Niles, Ill.*

Real-time, in-process weld monitoring offers advantages of economy and safety in weld repair, particularly in multipass situations. It allows bead by bead repair so the repair is less costly. It also minimizes perturbation of the weld material in the case of heavy section weld repair, thus providing a safer completed weld. It also has application in welder feedback control.

GARD has been studying both acoustic emission from solidifying welds and infrared weld puddle imaging as approaches to in-process weld monitoring. This presentation will describe the detection, location, and characterization of flaw types in welds by acoustic emission, and show examples of normal and digitally enhanced infrared weld puddle images.

INTRODUCTION

Real-time, in-process weld monitoring offers advantages of economy and safety in weld repair, particularly in multi-pass situations. It allows bead-by-bead repair so the repair is less costly. It also minimizes perturbation of the weld material in the case of weld repair, thus providing a safer completed weld. It also has application in welder feedback control.

In titanium weld inspection, the primary flaws of concern seem to be localized, not bulk flaws (i.e. cracks, interstitial gas, oxide layers, lack of penetration, etc.) which are created on a pass-by-pass basis. It therefore makes sense to consider using a defect detection approach, which inspects the weldment on a pass-by-pass basis. An in-process pass-by-pass inspection is more attractive than a stop-the-welding pass-by-pass inspection since it minimizes production time and reduces the chance of weld surface oxidation.

This paper discusses two techniques to in-process pass-by-pass weld inspection. The first, acoustic emission, has passed the feasibility stage, the initial hardware development stage, and is now in the application development phase. The second, infrared, is in the initial phases of feasibility.

ACOUSTIC EMISSION

Acoustic emission weld monitoring involves attaching "contact microphones" to the part being welded and listening for acoustic signals given off by flaws

which are created during the solidification of the weld. It has the advantage in in-process weld monitoring that it uses fixed sensor positions, and that it is not sensitive to flaw position or orientation. The sensing and signal processing is totally electronic, thus it is adaptable to computerization and weld control applications. In use, one sensor can be used to detect the presence of a flaw, and characterize the flaw as to size and type. Two sensors are located along the length of the weld to provide flaw location information by time of arrival difference of the flaw's acoustic signals between the two sensing transducers. An example of such a monitoring set-up is shown in Figure 1.

GARD has done a lot of acoustic emission weld monitoring over the past eight years. At last count GARD has monitored over 21,000 feet of weld (with acoustic emission) that has been correlated with other NDT techniques. GARD has monitored production automatic and manual welding. GARD has also monitored automatic and manual welding in the laboratory.

It became evident early in our monitoring that one of the prime problems in listening to welds for acoustic emission flaw information is the background noise generated during welding by other acoustic sources. There is arc noise, oxide or scale fracture noise, slag noise, and noise from weld restraints and backing bars. They all contribute signals which make it difficult to detect the acoustic flaw noise during the monitoring process.

Figure 2 shows typical acoustic event counts from various types of welding. It also shows the typical number of counts that we expect from a flaw such as a crack. The figure shows that signal-to-noise (that is crack information relative to background information) can be anywhere from one to one to one to four thousand. In addition to acoustic background noise, acoustic emission

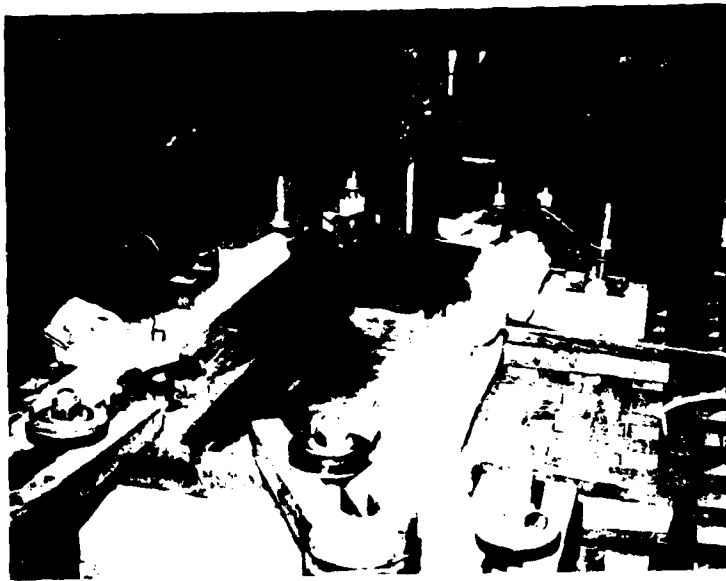


Figure 1 Acoustic Emission Weld Monitoring Setup

Figure 2

AE ACTIVITY DURING WELDING

<u>SOURCE</u>	<u>TYPICAL AE EVENT COUNT</u>
NORMAL GTAW STAINLESS STEEL	10—50
NORMAL SAW CARBON STEEL	30—1000
NORMAL SMAW CARBON STEEL	200—4000
HOT CRACK	1—10

monitoring has to be concerned about RF noises due to other equipment operating in the monitoring area, and mechanical noises due to shop operations conducted simultaneously on the part (such as grinding, chipping, or wire brushing).

GARD has developed a computerized data acquisition system which has allowed us to develop signal processing algorithms which can detect, locate, and characterize flaws in welding by the use of acoustic emission. Typical output from this data taking equipment is shown in Figure 3. This is a printout of each acoustic event which has occurred in the weld. For each event we have the time of the event, the energy given off in that event, the peak signal in various frequency bands for that event, information that relates to the time of arrival difference between transducer pairs for that event, and information as to which transducer heard the event first.

From this type of information GARD has been able to develop its detection algorithms. GARD uses the number of events within a given period of time from a given location as a primary flaw detection criterion. Location is determined by time of arrival difference between two transducers. Size is determined by average energy content in the pulses which define detect presence. Type of flaw is determined by signal content of a specific frequency band ratio.

Such detection algorithms have been incorporated into the hardware shown in Figure 4. This is a field-useable acoustic emission weld monitor. It has three analog transducer input channels. This allows the monitor to detect flaws in a plane. It has self-calibration feature which, in operation, sequentially changes each transducer from receiver to pulser. This allows the monitor to automatically calibrate transducer position on the part being inspected. It has a current sense feature which allows it to monitor,

```

1 WELD 21. PASS 1. 50 DB. 10450. RM TMP. 21 AUG 80 1415 RUN TIME 15 53 41

TIME   RDC1 RDC2 RDC3  110  150  200  270  370  500  675  920  L12  L13 ADD K
0 05 12   0   0   0   0   0   0   0   0   0   0   0   0   0 111 *
0 10 24   0   0   0   0   0   0   0   0   0   0   0   0   0 111 *
0 15 36   0   0   0   0   0   0   0   0   0   0   0   0   0 111 *
0 20 48   0   0   0   0   0   0   0   0   0   0   0   0   0 111 *
0 23 56  50  57   0  114  431  264  82  69  28  53  30  264 4068 12 *
0 23 98 1531 1763   0  493  640  514  338  273  137  169  80  111 4068 12 *
0 24 42   90  90   0  238  520  233  86  65  47  39  32  267 4068 12 *
0 24 72  112  71   0  278  253  182  77  49  50  36  26  282 4068 21 *
0 25 54   82 129   0  208  481  296  260  155  96  115  41  208 4068 12 W
0 25 60  245 151   0  264  225  321  69  27  28  33  19  296 4068 21 W
0 25 60   0   0   0   0   0   0   0   0   0   0   0   0   0 111 W
0 27 82   90  90   0  206  497  256  128  137  80  71  37  214 4068 12 W
0 28 58   99 115   0  193  647  240  86  153  123  105  54  214 4068 12 W
0 29 00   71  88   0  224  720  249  87  169  155  90  56  227 4068 12 W
0 30 72   0   0   0   0   0   0   0   0   0   0   0   0   0 111 W
0 30 88   63  86   0  186  763  279  137  201  147  91  57  1615 4068 12 W
0 31 08   58  87   0  149  664  262  73  86  67  73  38  223 4068 12 W
0 31 82  156 146   0  186  438  264  105  44  37  47  31  229 4068 21 W
0 32 26   67 122   0  147  486  287  115  101  34  37  26  250 4068 12 W
0 32 90  269 361   0  142  500  318  180  116  92  87  52  223 4068 12 W
0 33 64  109 129   0  178  331  211  149  90  40  42  31  215 4068 12 W
0 34 08   53  18   0   71  323  258  117  26  10  11  14  344 4068 21 W
0 34 32  101 173   0  168  382  333  165  179  85  66  46  273 4068 12 W
0 34 82  101 153   0  166  517  485  132  203  81  67  47  202 4068 12 W
0 34 98   43  68   0  122  547  306  141  63  41  38  31  240 4068 12 W
0 35 08   63  85   0  122  456  267  124  68  45  42  33  227 4068 12 W
0 35 22  145 287   0  137  323  258  423  361  120  172  110  218 4068 12 W
0 35 40  106 126   0  289  514  203  70  93  49  57  30  2866 4068 12 W
0 35 44 2690 2837   0  609  651  725  530  314  182  260  143  163 4068 12 W
0 35 74   0 114   0   87  415  250  103  289  34  32  13  217 4068 12 W
0 35 76  137 236   0   74  333  210  61  41  23  25  25  214 4068 12 W
0 35 84   0   0   0   0   0   0   0   0   0   0   0   0   0 111 W
0 35 92 1260 1578   0  294  497  539  479  322  170  192  126  175 4068 12 W
0 36 24   32 113   0  146  349  278  255  410  107  114  71  222 4068 12 W
0 36 28  106  69   0  179  777  229  86  137  91  100  59  289 4068 12 W
0 36 82   15  69   0  169  583  180  126  231  25  38  24  223 4068 12 W
0 37 32  360 543   0  241  688  353  264  335  146  163  86  224 4068 12 W
0 37 50   38  88   0  186  713  251  131  185  141  109  57  239 4068 12 W
0 37 54   65  92   0  155  366  368  66  42  35  27  22  258 4068 12 W
0 37 58   58  39   0  375  380  244  525  312  85  162  144  198 4068 12 W
0 38 08   37  54   0  307  312  289  72  120  41  37  28  246 4068 12 W
0 38 10  157 174   0  176  453  210  109  117  35  37  27  277 4068 12 W
0 38 32   79 150   0  336  745  549  405  522  153  176  124  206 4068 12 W
0 38 46  858 990   0  300  563  314  356  421  147  196  146  253 4068 12 W
0 38 54 1262 1559   0  333  535  337  417  308  170  186  121  263 4068 12 W
0 38 54   0 425   0  286  349  520  311  421  150  167  101  4064 4068 21 W
0 38 56  850 1041   0  285  363  414  479  268  149  150  168  210 4068 12 W
0 38 60 1080 1112   0  284  539  725  343  293  134  191  119  211 4068 12 W
0 38 64  989   0   0  329  560  631  344  276  122  162  101  4064 4068 2 W
0 38 76   71 122   0  212  593  580  349  238  131  131  71  311 4068 12 W

TIME   RDC1 RDC2 RDC3  110  150  200  270  370  500  675  920  L12  L13 ADD K
0 38 78  622  817   0  189  405  365  299  230  105  120  62  217 4068 12 W
0 38 80  144  159   0  266  393  317  214  183  136  103  75  299 4067 12 W
0 38 92 1136   0   0  576  915  533  409  282  159  181  123  4064 4068 1 W
0 38 98  702   0   0  775  770  509  274  202  122  182  81  4064 4068 1 W

```

Figure 3 AE Weld Monitor Data Printout

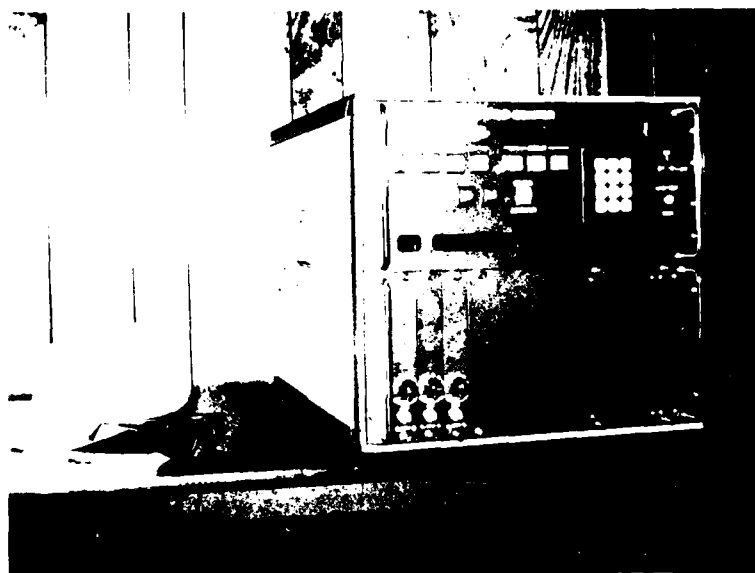


Figure 4 Acoustic Emission Weld Monitor

record, and iterate upwards the weld pass number as a function of weld current start and stop. It can record up to eight weld passes. It can store information on the location, size and type of up to 64 flaws. On an alphanumeric display, which is located above the keyboard, it can present real-time information as to flaw location. The monitor can be interrogated as to flaw type and size by an operator using the keyboard. The monitor can be used with an external oscilloscope to provide high resolution locational information. It can be used with a disk and terminal. In this mode of operation the monitor can be used as a data gathering system to generate data listings such as shown in Figure 3. The keyboard can also be used to modify the flaw detection algorithms located in EPROM inside the monitor itself.

Figure 5 shows a recent application of the weld monitor. It was used at Battelle/Columbus to monitor simulated gas pipeline welding. It monitored 21 welds and detected 13 out of 13 flaws induced while the monitor was operating. A typical flaw display is shown in Figure 6. The squares on both sides of the display indicate transducer placement. The display iterates downward after each flaw indication. Two flawed areas are indicated: one with one event, and one with four events. The first flaw was characterized as slag, with a magnitude 2 (out of a range of 1 to 10). This indication was produced during an attempt to produce hydrogen embrittlement by welding with a moist electrode. The second area of flaw indications was produced by welding over copper, which generates cracks.

Figure 7 shows the monitor being used in the inspection of a nuclear weld at Westinghouse/Tampa, where GARD monitored a circular manway weld.



Figure 5 Battelle/Columbus AEWB Test

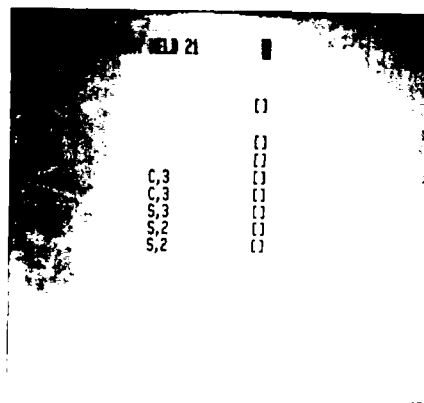


Figure 6 AE Weld Monitor Flaw Display



Figure 7 Westinghouse/Tampa AEW Test

Figure 8 shows an oscilloscope presentation of monitoring the results on a single pass. The locations of three monitoring transducers are shown as squares at the top and bottom of the picture. Resultant flaw indications are shown near the center. Figure 9 is a graphic display of the results which include the monitor's characterization of the flaws. Figure 10 shows a summary of the results of the complete manway weld. Seven flaws were detected during the test. Each was visually confirmed.

COMMENTS

As stated earlier this technology has passed the feasibility phase, the initial hardware development phase, and is now in an application evaluation phase. The two examples shown are part of this evaluation. GARD now has several programs with various agencies: U.S. Army, DOE, and the Federal Highway Administration. These programs are evaluating the use of acoustic emission weld monitoring on various types of material with various welding processes.

Several comments relative to titanium welding and its monitoring by acoustic emission; Detection of interstitial gas is important. It can likely be detected if we assume it leads to embrittlement, which in turn leads to micro-cracking (if not on the actual embrittling pass, then on the subsequent pass or passes). Oxide layer formation on the weld surface is a problem with titanium welding. This oxide is brittle. It is likely to generate micro-cracking on subsequent weld passes. Such micro-cracking should be detectable by acoustic emission.

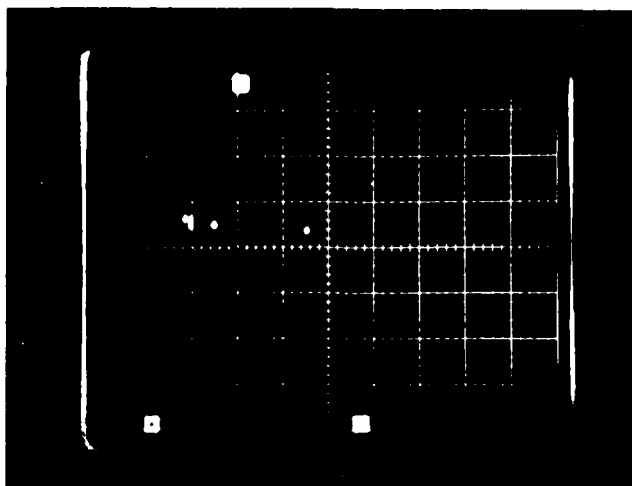


Figure 8 OSCILLOSCOPE DISPLAY, LACK OF FUSION

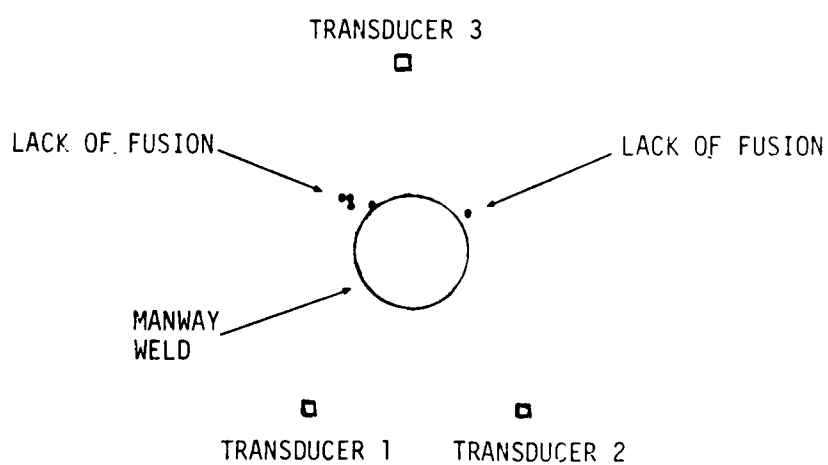


Figure 9 INDICATED LACK OF FUSION LOCATION
RELATIVE TO MANWAY WELD

Figure 10

SUMMARY OF RESULTS
FOR
STEAM GENERATOR MANWAY WELD

FLAW TYPE (VISUAL CONFIRMATION)	NUMBER OF PASSES INDICATION OBSERVED	AEWM CALL	AEWM SENSITIVITY
SLAG DEPOSIT	2	SLAG	72db
SLAG INCLUSION	1	SLAG	66db
LACK OF FUSION	4	SLAG/CRACK	66db

INFRARED IMAGING

Here we present some early feasibility work which shows that infrared viewing of a weld puddle has potential for real-time weld monitoring. It can detect flaw formation in welds and has potential, by "isotherm" viewing, as a weld process control input. Figure 11 shows the experimental set-up used at GARD in the weld puddle imaging which is documented in the figures which follow. The figures are copies of slides made from a video tape which was generated during a live weld monitoring test by an infrared vidicon. Figure 12 shows a normal MIG weld puddle viewed from an almost vertical angle. Evident is the arc, the edge of the gas cup, solidifying weld material, the liquid metal, and silicate floating in the liquid.

Several flaw induction tests were run. How the puddle was effected is shown in the following figures. Figure 13 shows the puddle disturbance caused by inducing copper into the weld. Copper normally induces cracks in a weld. Figure 14 shows the puddle disturbance caused by the induction of a piece of high strength carbon steel into the weld. This normally produces hot cracking. A tendency towards this can be seen in the newly solidified region of the weld puddle. Figure 15 shows the puddle disturbance induced by running a moist shield gas into the weld. This normally produces porosity in the weld. The resultant turbulence can be seen.

While such puddle image variations can obviously be monitored by an operator in a real-time situation, the ultimate potential for puddle imaging is that of automatic image analysis and flaw detection by computer. Figure 16 shows a four bit digitally-enhanced view of a normal MIG weld puddle. The figure clearly shows energy contours in various regions of the image. It is

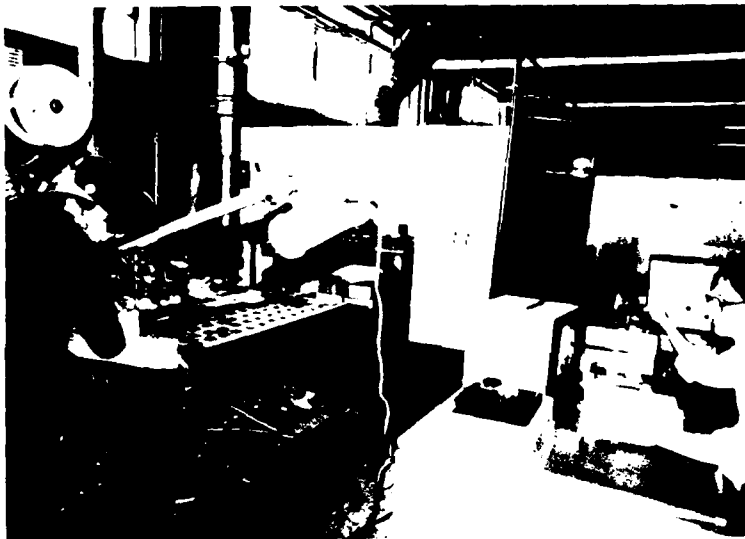


Figure 11 Weld Puddle Monitoring Setup



Figure 12 Normal MIG Weld Puddle



Figure 13 Weld Puddle With Copper Introduced



Figure 14 Weld Puddle With High Strength Carbon Steel Introduced



Figure 15 Weld Puddle With Moist Shield Gas Introduced



Figure 16 Digitally Enhanced Weld Puddle

obvious that such images or more highly-processed images can be used by computers in a pattern recognition mode for either flaw detection or weld control.

CONCLUSION

Two techniques for in-process weld monitoring have been discussed. They both have potential application to titanium weld monitoring. The first technique, acoustic emission, has been successfully demonstrated on metals other than titanium. It is available in hardware now: it can be used to detect, locate and characterize weld flaws in real-time. It will be straight forward to evaluate its state-of-the-art potential for titanium weld inspection. The second technique infrared imaging is simply in a feasibility stage. Much work will have to be done in terms of experimentation to determine its sensitivity to flaw detection and potential for in-process titanium weld monitoring.

PHOTOACOUSTIC MICROSCOPY*

R. L. Thomas, L.D. Favro, P. K. Kuo, L. I. Inglehart and J. J. Pouch

*Department of Physics
Wayne State University
Detroit, Michigan 48202*

The technique of scanning photoacoustic microscopy (SPAM) is useful for nondestructive evaluation of metal surfaces and subsurfaces. Surface flaws can be detected with a resolution of $6\text{ }\mu\text{m}$ or better and the subsurface can be systematically probed by varying the chopping frequency of the laser. Subsurface flaws can be detected to a depth of approximately two thermal diffusion lengths ($\sim 2\text{ mm}$ at the lowest chopping frequencies for Al). The current status of this technique will be reviewed and examples will be given of NDE applications for metals, ceramics and semiconductors.

In this paper we present a brief overview of the technique of Scanning Photoacoustic Microscopy¹⁻⁶ (SPAM) as it applies to problems of NDE. The technique is perhaps more appropriately described as a photothermal one, since the relevant parameters for NDE are optical absorption and thermal diffusivity for most of the experiments discussed in this paper. Alternative experiments⁶ using piezoelectric detectors, also involve the elastic properties of the solid, although the main advantages of the technique for NDE.

A block diagram of the apparatus is shown in Fig. 1. The intensity of the laser is chopped at frequency f_c , and focussed onto the surface of the sample, which is contained in a gas filled cell with an optical window. The resulting ac temperature profile of the surface periodically heats the layer of gas within a thermal diffusion length of the surface, and the resulting pressure variation couples through the gas to the microphone. The output of the microphone is monitored in magnitude and phase by means of a lock-in amplifier which is referenced to the chopping frequency. Variations in either the optical absorption or the thermal diffusivity (α) lead to changes in the photoacoustic signal.

The theory² has been worked out for an opaque solid slab with a back surface step, varying in thickness from $\Delta \gg \mu_s$ to δ , where $\mu_s = (2\alpha/\omega)^{1/2}$, and $\omega = 2\pi f_c$. The result for the magnitude of the SPAM signal is shown in Fig. 2, and that for the phase in Fig. 3. Excellent agreement is found with experimental measurements² on an aluminum slab with a back surface slot, shown in Fig. 4. The results show that the thermal wave signal from the back surface is observable in the magnitude for $\delta \lesssim \mu_s$.

The technique has been applied to NDE in ceramic materials, for which, for example, one can observe near subsurface inhomogeneities³ such as the

~200 μm Fe particle inclusion in Si_3N_4 shown in Fig. 5. Small cracks in complex shaped parts can also be detected⁴ (see Figs. 6,7), and defects on the surface and near subsurface of a semiconductor I/C chip can be detected⁵ with 6 μm resolution (Fig. 8).

REFERENCES

1. L. D. Favro, L. I. Inglehart, P. K. Kuo, J. J. Pouch and R. L. Thomas, to be published in Proceedings of the DARPA/AFML Review of Progress in Quantitative NDE, July 14-17, 1980.
2. R. L. Thomas, J. J. Pouch, Y. H. Wong, L. D. Favro, P. K. Kuo and Allan Rosencwaig, J. Appl. Phys. 51, 1152 (1980).
3. J. J. Pouch, R. L. Thomas, Y. H. Wong, J. Schuldies and M. Srinivasan, J. Opt. Soc. Am. 70, 562 (1980).
4. L. I. Inglehart, R. L. Thomas and J. Schuldies, submitted for publication.
5. L. D. Favro, P. K. Kuo, J. J. Pouch, and R. L. Thomas Appl. Phys. Letters 36, 953 (1980).
6. Proceedings of IEEE Ultrasonic Symposium, Boston, Nov. 5-7, 1980.

*Research supported in part by the Office of Army Research under Contract No. DAAG 29-79-C-0151, by AiResearch Manufacturing Company of Arizona, and by the Carborundum Company.

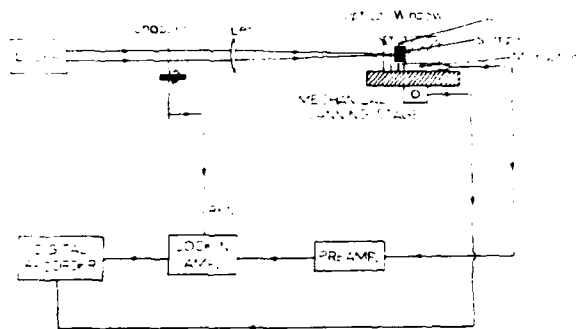


FIG. 1. Block diagram of the apparatus. Not shown is the microprocessor which controls the mechanical scanning stage.

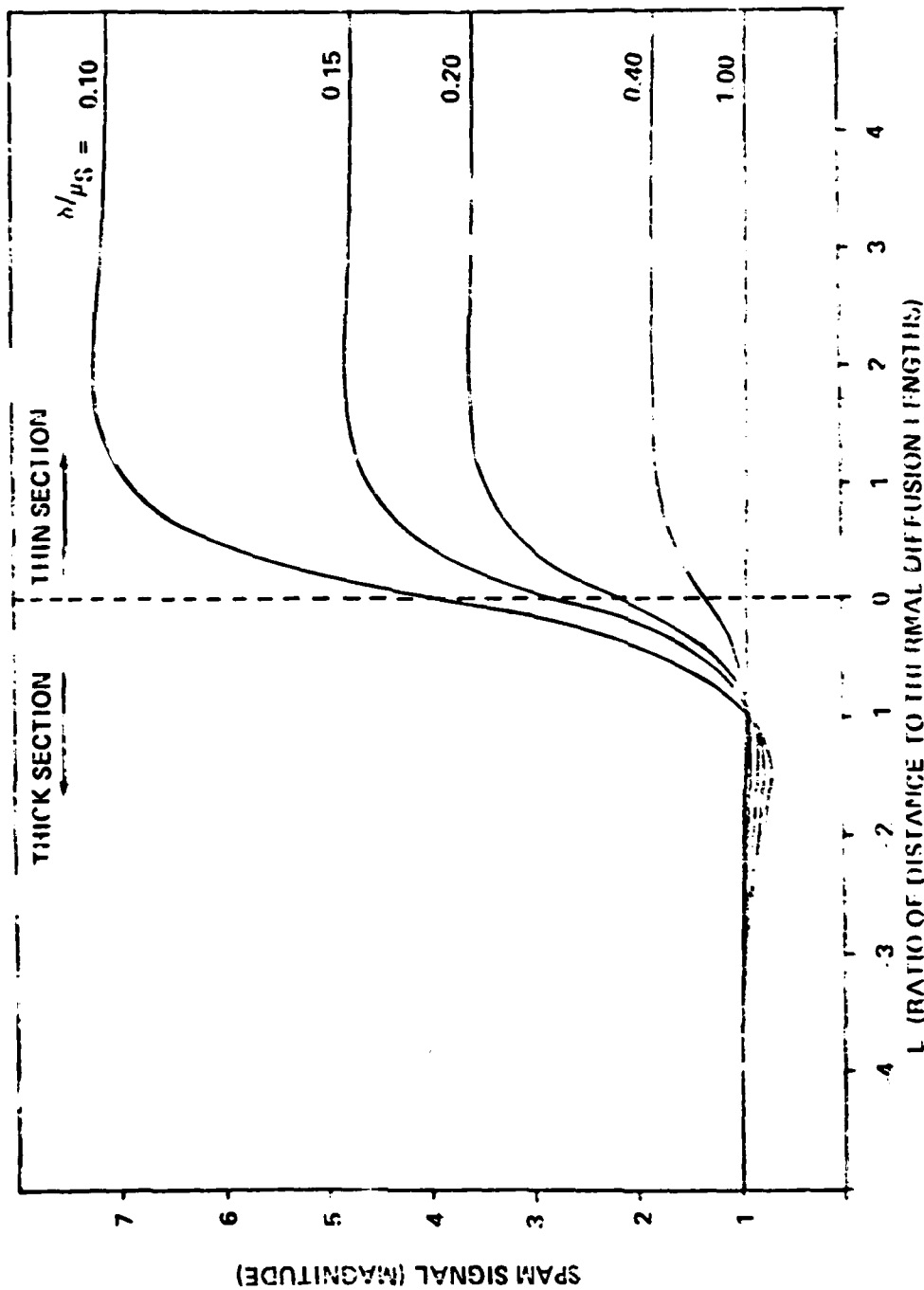


Figure 2. Calculated Results Obtained for the Relative Magnitude of the SPAM Signal.

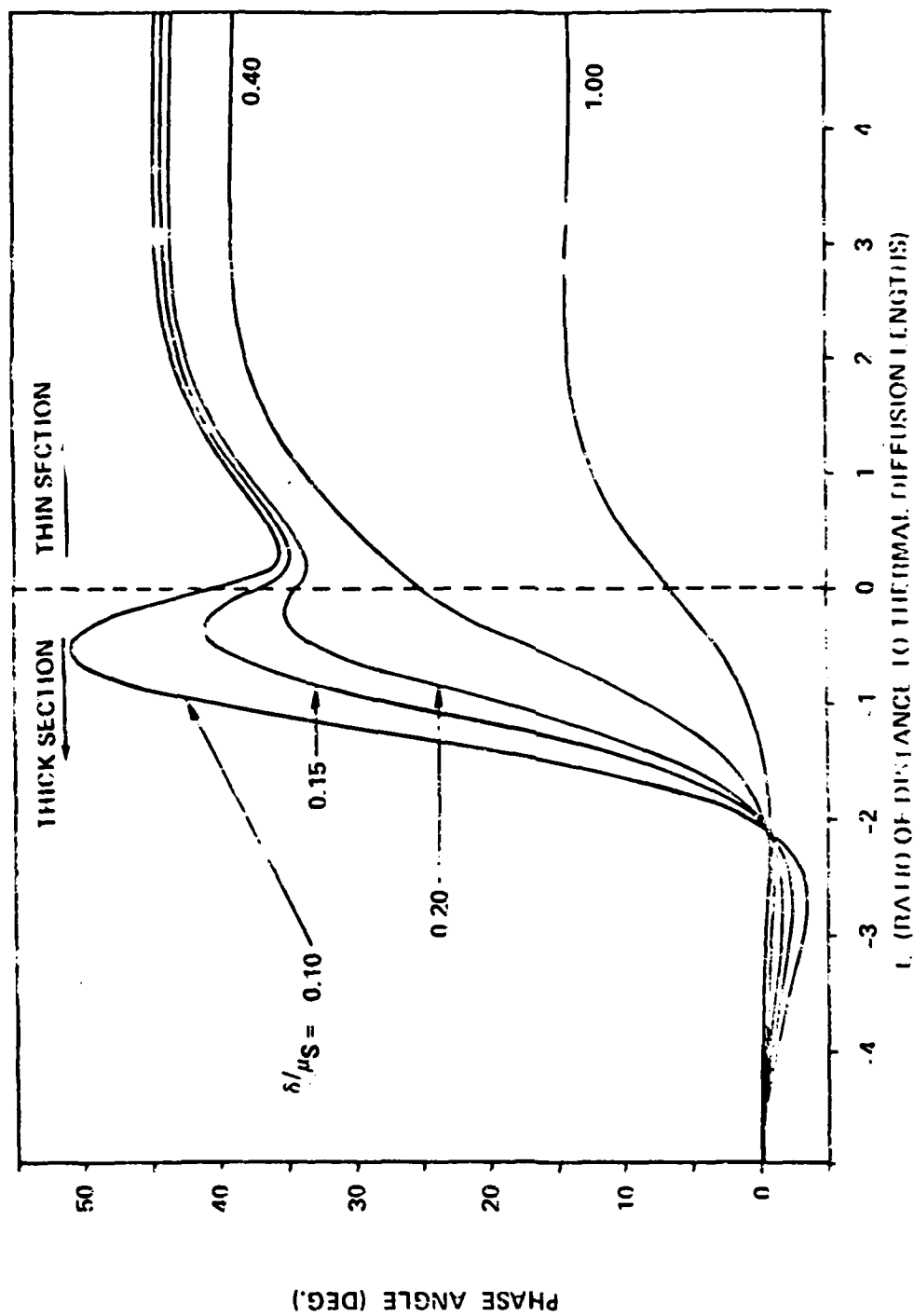


Figure 3. Calculated Results Obtained for the Relative Phase of the Beam Signal.

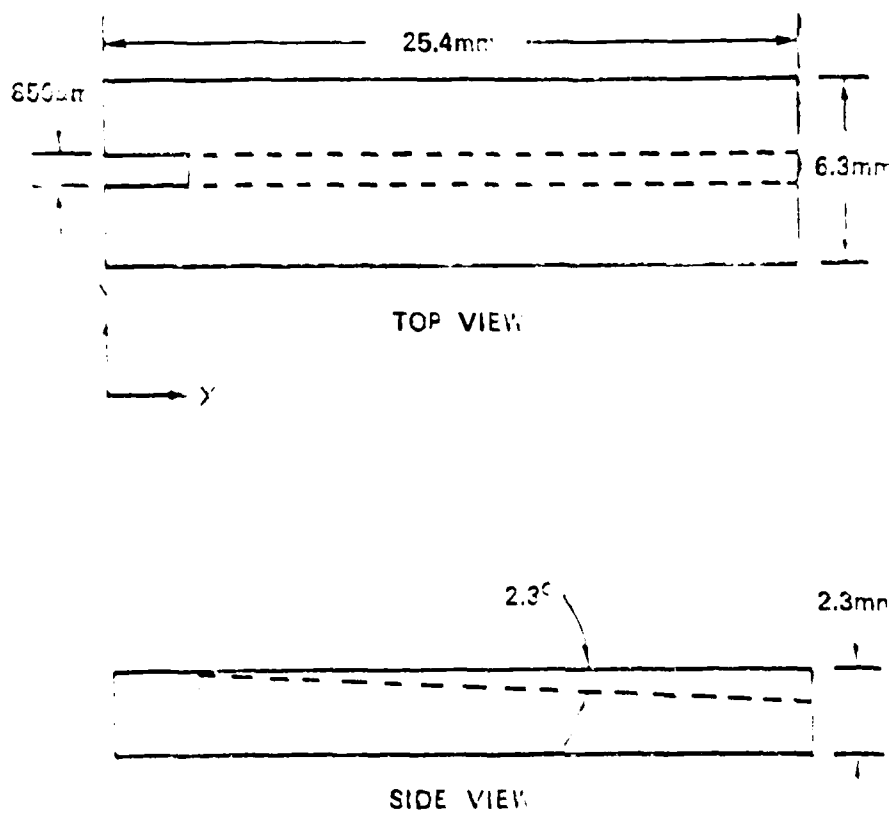


Figure 4 Photoscoustic Effect on an Aluminum Sample.

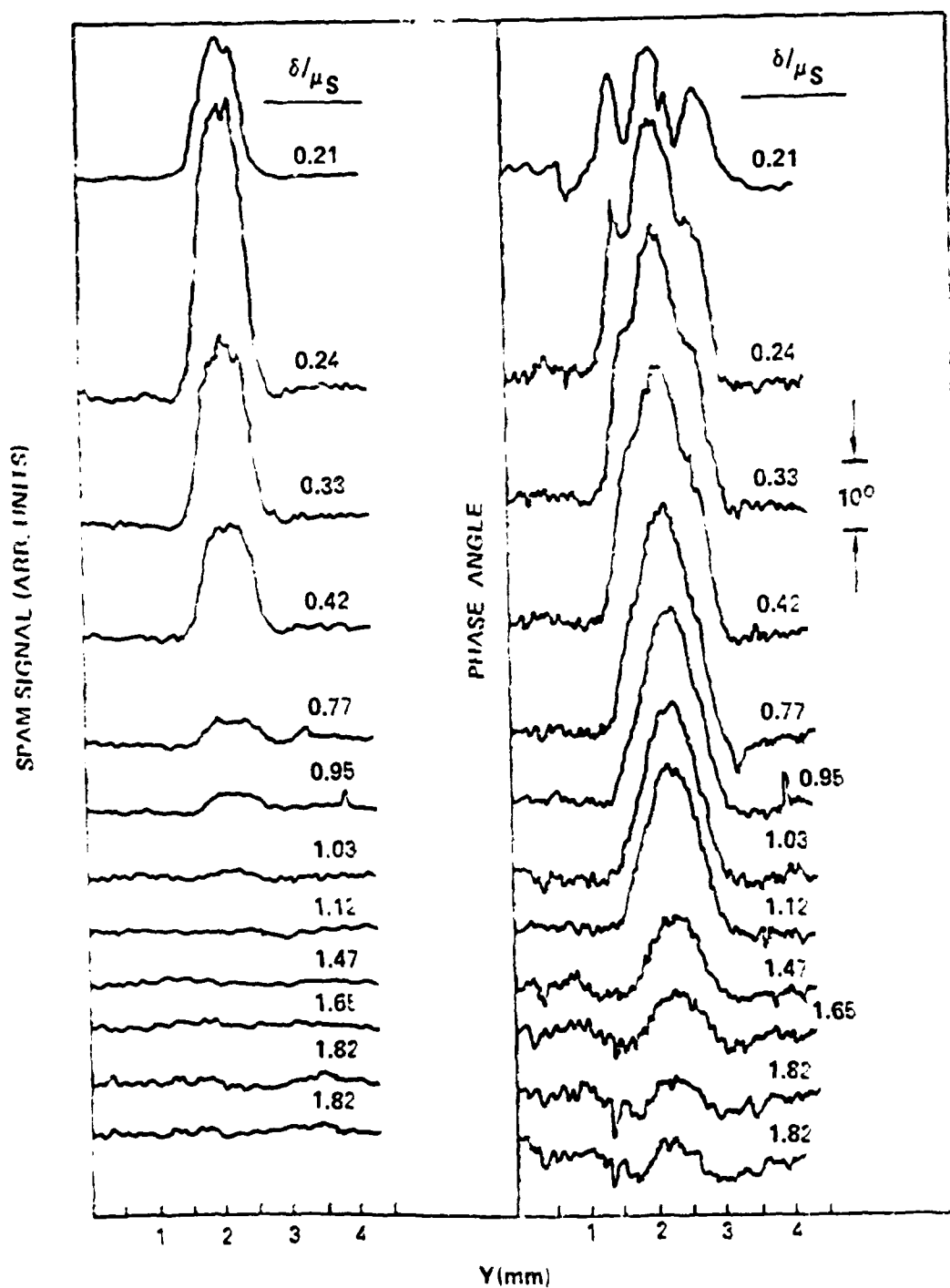
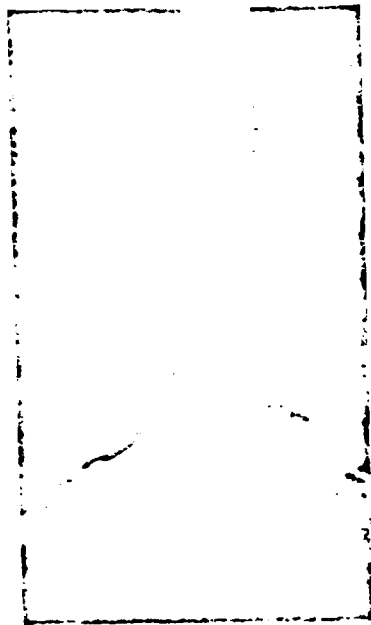
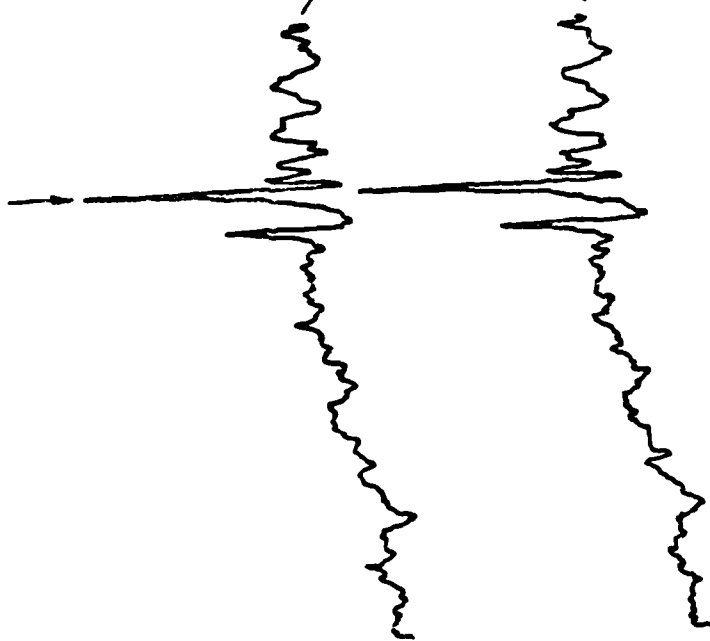


Figure 5 Comparison of Results of Relative Magnitude and Phase for a Slot.

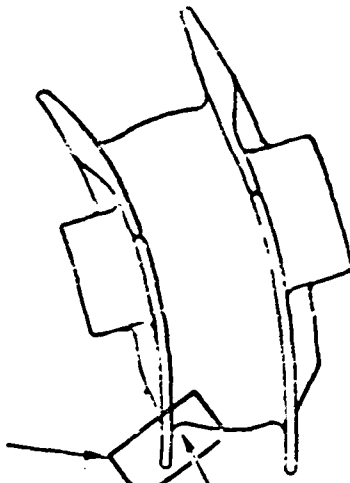
SPAM RESULTS



DEFECT SIGNAL



ISOLATION
CELL



STATOR VANE NO. 268
MATERIAL - SLIP CAST Si_3N_4

SPAM TRACES FROM I.E.
FILLET REPEATABILITY SCANS

Figure 6. SPAM Results.

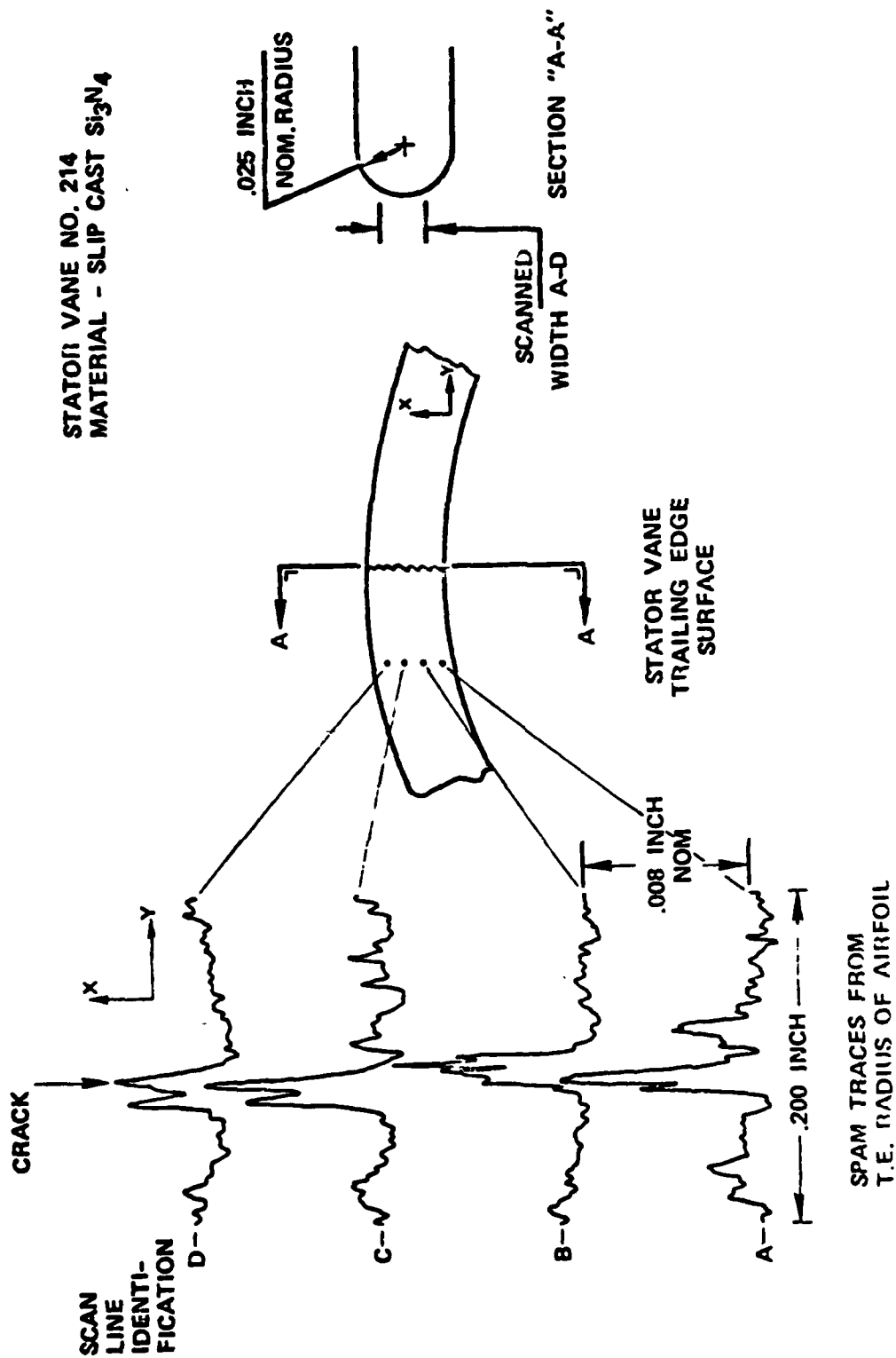


Figure 7 SPAM Results.

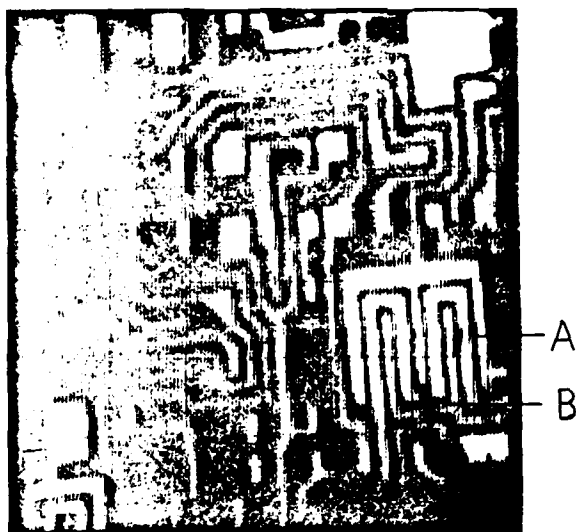


Fig. 8 Photoacoustic microscope picture of an integrated circuit, taken with the reference phase adjusted to give maximum brightness when the beam was on the large metalized area in the upper right-hand corner. A and B are visually observable defects.

COMPUTED TOMOGRAPHY FOR INSPECTION OF INDUSTRIAL OBJECTS*

Richard Kruger

*Los Alamos Scientific Laboratory
Los Alamos, New Mexico*

Computerized tomography has made a significant impact on medical diagnosis. Its application to industrial objects is now being actively pursued. This paper reviews computerized tomography technology, describes a working prototype at Los Alamos Scientific Laboratory, and presents tomograms of industrial objects including a titanium alloy phantom. Visualization of 300 micrometer air voids in a 51 mm cylindrical Ti-6Al-4V phantom will also be discussed.

Computed Tomography for Inspection of Industrial Objects*

by

R. P. Kruger
University of California
Los Alamos National Laboratory
Los Alamos, New Mexico 87545

It would not be an understatement to say that computed tomography has made a tremendous impact in medical diagnosis during the past decade. This interpretation modality is now beginning to make a similar impact in the nondestructive evaluation of reactor components,¹ steel butt welds,² and industrial materials such as electrical power capacitors.³

In tomography, let $I(E)$ denote a polychromatic x-ray or gamma-ray source beam. If these photons are detected with a perfect detector, the integrated signal is

$$I_0 = \int_0^{\epsilon} I(E) dE, \quad (1)$$

where ϵ denotes the maximum energy present in the beam. If the source beam passes through a cross section of an object with linear attenuation $\mu_z(x,y,E)$, the detected signal intensity will be

$$I_{\theta}(x) = \int_0^{\epsilon} I(E) \exp \left[- \int_L \mu_z(x,y,E) dy \right] dE, \quad (2)$$

The polychromatic projection pathlength is defined

$$p_z(x,\theta) = \ln [I_0 / I_{\theta}(x)]. \quad (3)$$

When beam changes occur, μ changes as a function of x and y as a result of changes in beam energy (E).

If the source is monochromatic [$I_0(E_0) = I_0 \delta(E - E_0)$] and efforts are made to eliminate beam softening, Eq. (3) reduces to

*Work performed under the auspices of the U.S. Department of Energy, under Contract No. W7405-ENG-36.

$$p_z(x, \theta) = \int_L \mu_z(x, y, E_0) dy \quad , \quad (4)$$

and the projection data represents the integrated pathlength L through the object at angle θ for a single energy E_0 . Beam energy does not change, and μ remains constant as a result.

The collection of all such projections p , when visualized as a two-dimensional image of $p_z(x, \theta)$, is called a sinogram. It is called this because a detected point object would record a sinusoidal path when source and detector are rotated about it.

In any event, the now familiar backprojection formula can be used to reconstruct the linear attenuation cross section of the object $\mu_z(x, y)$,

$$\mu_z(x, y) = \int_{\theta} \tilde{p}_z(x \cos \theta + y \sin \theta, \theta) d\theta \quad , \quad (5)$$

where \tilde{p} is a filtered version of the original projection p .

The additive signal-dependent noise present in tomographic projection data p_z is considered to be Poisson in nature. Thus, if \bar{I} represents the mean detected projection intensity, the noise standard deviation is $\sqrt{\bar{I}}$. This projection-based noise is reduced by \sqrt{w} in the backprojection process where w is the number of projections used to approximate the integral of Eq. (5). This brief discussion has avoided many nuances associated with computed tomographic reconstruction. It is intended only to give the reader basic information. More detail can be found elsewhere.¹

The Los Alamos tomographic scanner hardware is designed as a modular system. The source, x , y , θ stages, and detector are each discrete mechanisms mounted on separate stands. In this way, the system is tailored to permit sensitivity and/or spatial resolution to be optimized for a particular problem. A generic description of the scanner is shown in Fig. 1.

The detector collimator consists of a pair of movable plates permitting the collimator aperture to vary from a minimum of 0.05 mm up to a maximum of several millimeters on a side. The detector itself is simply placed behind the plates and can be a solid-state detector, a NaI detector, or a proportional counter depending upon the application.

The scanner assembly moves the object under inspection back and forth through the radiation beam and angularly rotates it between scans. The assembly is built from commercially available linear and rotational modules. All axes are driven by direct-current stepping motors controlled by an LSI-11.

The source module is a stand that permits many types of sources to be mounted on it. Isotopic gamma ray sources are inserted inside a cylindrical shield with an insert that collimates the beam.

The tomographic system interface controller that connects the LSI-11 computer to the mechanical tomographic scanner assembly is also designed in a modular fashion. This permits a high degree of flexibility and ease of modification for particular applications.

This scanner has allowed us to experiment with many different x-ray and gamma-ray sources and many different scan geometries. It is well suited to feasibility studies and is ill suited for production inspection tasks. Several tomographic examples will now be shown to demonstrate this flexibility.

There is a need at Los Alamos for robust capacitor designs in the laser fusion program. A nondestructive method of assessing damage during use was needed. Computed tomography has been valuable in this regard.

The capacitor used for the initial experiments consisted of a 2.54-cm-diam cylindrical power capacitor composed of rolled, thin layers of polypropylene film and aluminum foil. Silicone fluid was also present as an additional dielectric. This capacitor had not yet electrically failed. However, the conventional radiograph of the capacitor indicated a large irregularly shaped defect region. The tomographic plane thickness was set at 2.5 mm, and the tomographic resolution was set at 0.1 mm/pixel. This was accomplished by adjusting the detector collimator to a height of 2.5 mm and a width of 0.1 mm. The source-detector distance was 60 mm. A conventional x-ray source was used and was set at 50 keV and 4.0 ma. Figure 2 shows a typical tomographic cross section representing μ . It is clear that the more dense aluminum has coalesced creating less dense voided regions around it.

The next three examples all represent 10.16-cm-diam objects with a reconstruction pixel size of 0.2 mm and a plane thickness of 2 mm. The source used in these examples was ^{192}Ir . Figure 3a is an aluminum cylinder with several small holes drilled in it. The smallest of these holes is 0.5 mm.

This represents an ability to detect objects as small as 0.5% of the object diameter. Figure 3b is a simulated small rocket propellant cross section. The outer cylinder is stainless steel and teflon and is used to simulate the propellant. Small defects have been milled into the outer cylinder wall and the teflon. Several other aluminum, steel, and air voids have also been inserted into the teflon. Figure 3c is a TI-4AL-V titanium alloy cylinder. The smallest defect size again represents 0.5% of the diameter. The pie-shaped cut has been filled with Lucite on one edge and aluminum on the other. Both μ estimates are detectably different from the cylindrical air voids and the titanium alloy. The ability to detect μ differences of 1% or less with spatial accuracy of 0.5% or less makes tomography an excellent NDE tool for many applications.

REFERENCES

1. R. P. Kruger, G. W. Wecksung, R. A. Morris, "Industrial Applications of Computed Tomography at Los Alamos Scientific Laboratory," Opt. Eng. Vol. 19, No. 3, June 1980.
2. I. L. Morgan, H. Ellinger, R. Klinksiek, F. Hopkins, J. Thompson, "Tomography Analysis of Structural Materials," SPIE Vol. 182, Imaging Applications for Automated Industrial Inspection and Assembly, April 1979, pp 179-186.
3. R. P. Kruger, "Nonmedical Application of Computed Tomography to Power Capacitor Quality Assessment," to appear in the IEEE Nuc. Sci. Trans., April 1981.

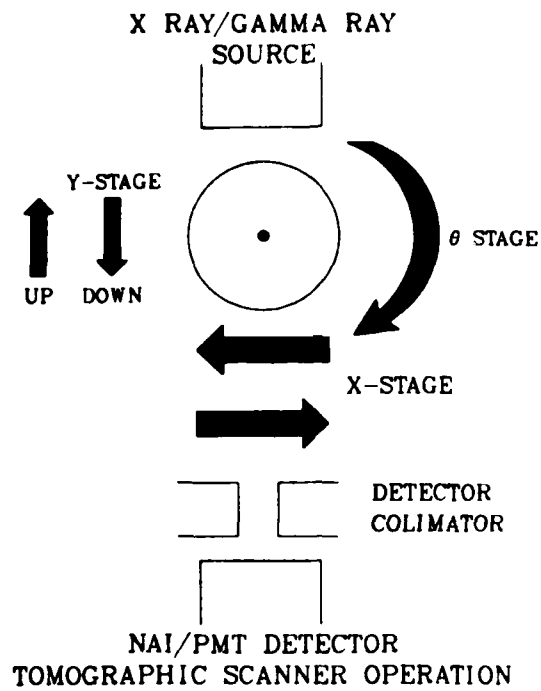


Figure 1

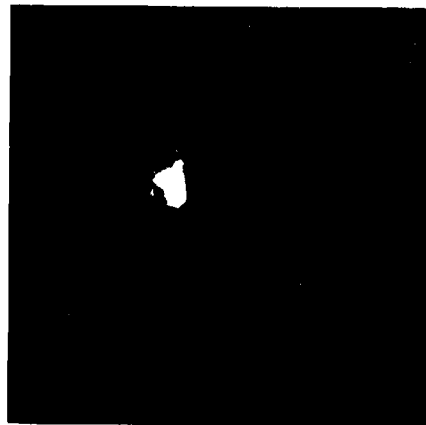


Figure 2 Capacitor Cross Section

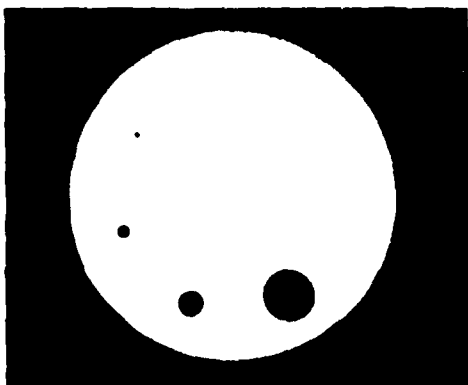


Figure 3a Aluminum cylinder tomogram

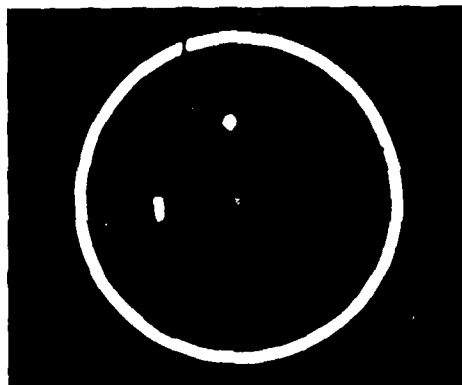


Figure 3b Simulated artillery shell/rocket motor tomogram

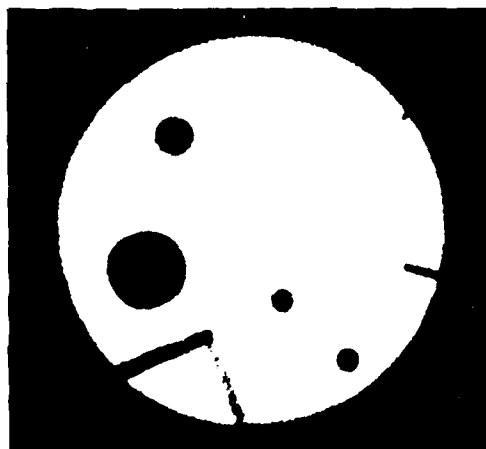


Figure 3c TI-4AL-V alloy tomogram

RANDOM SIGNAL CORRELATION AND SPLIT SPECTRUM PROCESSING

E. S. Furgason, N. M. Bilgutay, B. B. Lee and V. L. Newhouse

*School of Electrical Engineering
Purdue University
West Lafayette, Indiana 47907*

Two complementary techniques are described which allow enhanced detection of flaws in large grained materials. In the first technique, a correlation system is used to enhance the signal-to-noise ratio of the received ultrasonic echo signals. This system is microprocessor compatible and can operate with both random and pseudorandom transmit signals. Results are shown which demonstrate the enhancement capabilities and flexibility of this system. A flaw-to-grain enhancement technique called split-spectrum processing is then described which improves the flaw-to-grain echo ratio in large grained materials. This enhancement is achieved by partitioning a wideband received spectrum to obtain decorrelated bands, which are then processed to suppress the grain echoes with respect to the flaw echo. Experimental results for titanium and stainless steel are presented showing improved flaw detection capabilities.

Introduction

The detection and imaging of flaws in large grained materials is a very difficult problem, especially when the material is highly attenuative. It requires both a method for increasing signal-to-noise ratio, and a method to enhance flaw echoes while suppressing grain echoes. One of the most effective techniques for increasing signal-to-noise ratio is with the highly sensitive random signal correlation system¹ developed in our laboratory. More recently we have developed a promising split-spectrum processing technique which has been shown to improve the flaw-to-grain echo ratio.

The original random signal correlation system is shown in Fig. 1. This system obtains high sensitivity through two associated processes - pulse-compression and time averaging - both of which occur in the correlation receiver. In pulse-compression, the system overcomes peak power limitations by transmitting large time-bandwidth random or pseudo-random signals and then compresses them by correlation with a reference signal. The pulse-compression results in output signals with resolution equivalent to pulse-echo systems and allows the system to obtain the maximum power output, which is not reduced by increasing scan range, as it is in conventional pulse-echo systems¹. In addition, since correlation is an integration process which can be made to occur over more than one transmit burst at each range of a scan, the system performs the equivalent of time averaging to increase the signal-to-noise ratio even more.

Even with high signal-to-noise ratio it may still be difficult to locate flaws due to another type of interference. When the range cell of an ultrasound pulse-echo flaw detection system contains many unresolved and

random reflectors such as grains, the overlapping echoes which result can make the detection of flaws within the range cell difficult even when the flaws are substantially larger than the grains.

There is a technique used in radar to extract targets that are embedded in smaller random targets known as clutter, which like grains result in unresolved and randomly distributed reflections that conceal the desired target. To improve the detection of targets in clutter, the clutter echoes are uncorrelated by simultaneously transmitting with two or more channels centered at different frequencies or by shifting the transmitted frequency between pulses. The decorrelated received clutter signals are then averaged, which results in signal-to-clutter ratio enhancement.

Ultrasonic applications of the frequency diversity concept have been limited. Koryachenko² analyzed the possibilities of applying frequency diversity concepts to flaw detection while Kraus and Goebbels³ have reported experimental results for a similar technique. In their work, Kraus and Goebbels use a broad-band transducer to transmit a set of 1024 smaller bandwidth signals, at center frequencies distributed over 3.7-5.3 MHz. The resulting echoes are subsequently rectified and averaged, resulting in enhancement of the flaw-to-grain echo ratio.

We recently developed⁴ a different approach to flaw enhancement, referred to as split-spectrum processing, which produces frequency diverse quasi-decorrelated signals from the received wideband signal by digital filtering instead of by transmitting many different narrow band signals. In addition, a novel minimization algorithm is used which gives results superior to the averaging procedures developed earlier. In this technique the decorrelated or quasi-decorrelated signals are produced by splitting a wideband echo spectrum as described above. The final enhancement signal is then

produced from these signals by plotting, at each range, the minimum amplitude exhibited by any of the signals at that range.

Signal-to-Noise Ratio Enhancement

The signal-to-noise ratio enhancement, SNRE, of the correlation system is given by the the band compression of the correlator¹ and is thus

$$\text{SNRE} = \alpha BT \quad (1)$$

where α is the duty cycle of the transmitter, $B_{in} = B$ is the receiver 3 dB bandwidth and T is the integration time of the output low-pass filter, which is approximately one-half the reciprocal of the low-pass 3 dB bandwidth.

The factors α and B are constrained, but the integration time, T , can be increased arbitrarily and is limited only by the stability of the integrator and the rigidity of the scanning system. The signal-to-noise ratio enhancement of the system can be seen in the correlation output of Fig. 2. This output shows the presence of a simulated flaw (a small hole) in a small grained titanium sample in which the received flaw echo was buried in receiver noise. The system is not able, however, to distinguish flaws from grains in large grained materials unless a method such as the split-spectrum processing technique is employed.

Recently, we have improved the original random signal system by developing an entirely digital version, Fig. 3. This new system replaces the bulky acoustic delay line of the original random signal system with a set of high speed digital shift registers. All controls; scan rate, scan range, initial range and number of integrated transmit bursts at each range are digitally controlled. This digital control makes the system compatible

with microprocessor control for automated system applications. The new system also has the capability of using either pseudo-random or random transmit signals.

Results using this system have produced outputs equivalent in resolution to pulse-echo systems for both the pseudo-random or random transmit signals, as shown in Fig. 4. However, when the system is operated at higher speed (i.e. less correlation time) significant noise becomes evident around the desired echo, as shown in Fig. 5. This is self-noise due to incomplete pulse-compression. In the present system, used for the split-spectrum processing, the self-noise was reduced to a tolerable level by correlation over many transmit bursts, slowing system speed somewhat. In order to increase system speed, we are currently developing a new type of correlation system which would use a different type of large time-bandwidth transmit signal called complementary Golay codes⁵. Complementary Golay codes have the special property that when the correlation outputs from two codes within a complementary pair are added, the self-noise should cancel, as shown in the computer simulations of Fig. 6. An initial prototype system, using 64 bit complementary Golay codes, has produced the outputs shown in Fig. 7. As can be seen, there is some residual noise left due to incomplete cancellation. More work is required on better transmitter design to increase this self-noise cancellation so that this new system could be used in conjunction with the split-spectrum processing technique to be described.

Split-Spectrum Technique

When the range cell of an ultrasound system contains many unresolved and random reflectors such as grains, the overlapping echoes which result

make the detection of flaws within the range cell difficult even when the flaws are substantially larger than the grains. This problem arises in the ultrasonic examination of many industrially important materials such as titanium, ceramics and stainless steel. Since grain echoes are stationary with respect to time, it is not possible to improve the flaw-to-grain echo ratio through utilization of time averaging or correlation techniques which are effective in random noise suppression.

Since the grains are small and closely spaced, their echoes result in a complicated interference pattern which, unlike flaw echoes, is highly sensitive to shifts in the transmitted frequency. Therefore, decorrelation in grain echoes can be obtained by shifting the transmitted frequency, which makes flaw visibility improvement possible with further processing. This basic principle has led to the development of a split-spectrum processing technique for an ultrasonic flaw detection system which improves the flaw-to-grain echo ratio in large grained materials.

The split-spectrum technique which obtains frequency diverse signals from the original wideband output of the ultrasound correlation receiver operates as follows. The program Fourier transforms the wideband system output to obtain the amplitude spectrum of the echo signal, divides the spectrum into the desired number of bands by means of digital filtering, and finally inverse Fourier transforms each band to obtain the individual frequency shifted signals. Filtering is accomplished by Gaussian shaped windows having selectable bandwidth b and fixed frequency spacing Δf . The center frequencies of the resulting signals range within the half-power bandwidth of the transducer. These signals are then normalized with respect to amplitude, giving zero-mean outputs with maximum magnitude of unity. The

resulting set of decorrelated signals are then processed using techniques described below to enhance flaw visibility.

Signal Processing Techniques

Several techniques have been employed for processing the signal set obtained from the original wideband echo signal:

a) Average of Squared Signals:

This conventional technique has been used in previous frequency averaging applications and is similar to square-law detection followed by n-pulse integration in radar. In this technique, the signals corresponding to different frequency bands are normalized, squared and then averaged. If we define $r_i(t)$ as the filtered and normalized signal corresponding to the i th band centered at frequency f_i , then the output of the averaging algorithm is given by

$$y(t) = \frac{1}{m} \sum_{i=1}^m r_i^2(t) = \overline{r^2}(t) \quad (2)$$

where m is the number of frequency shifted signals.

b) Square of Averaged Signals:

This is an alternate averaging technique which averages the normalized signals corresponding to the different frequency bands and squares the resulting signal giving

$$y(t) = \left[\frac{1}{m} \sum_{i=1}^m r_i(t) \right]^2 = \overline{r}^2(t) \quad (3)$$

c) Minimization of Squared Signals:

The minimization technique, originally introduced by this group⁴ represents the reflection at each range by the minimum amplitude appearing at that corresponding range in any of the m filtered, normalized, and squared signals. The output for the minimization algorithm may be defined as

$$y(t) = \min_t \left[r_i^2(t); i=1,2,\dots,m \right] = r_{\min}^2(t) \quad (4)$$

In all three cases the final processed data results in positive values which are normalized to unity for comparison purposes.

Experimental Results

In the work described here a wideband transmitted noise signal centered at 5 MHz with 2 MHz half-power bandwidth is used in a correlation type random signal flaw detection system shown in Fig. 1. The processing algorithms described above have been applied to output data obtained from a titanium sample with average grain boundary spacing of 15 μm , containing a flat-bottom hole to simulate the flaw. Figure 8 shows the unprocessed correlator signal for a 1.19 mm diameter hole at 76.2 mm depth surrounded by grain echoes. Figure 9 shows the square of this signal and the processed outputs for the averaging and minimization algorithms with the optimal values of Δf and b . The number of signals in the processing set is determined by the transducer bandwidth B , which is 2 MHz centered at 5 MHz, and the frequency spacing Δf . Therefore, for example, $\Delta f=100$ kHz results in twenty-one signals ranging in center frequency between 4-6 MHz which account for the signal set used in the processing algorithms.

The enhancement for the averaging algorithms shown in Figure 9 is seen to be limited. However, the minimization algorithm clearly improves the flaw visibility significantly. In addition to suppressing the grain echoes, the minimization algorithm results in considerable improvement in resolution which can be seen by comparing plots in Fig. 9.

The performance of the three algorithms was also examined using a stainless steel sample with average grain size of $106\text{ }\mu\text{m}$ having a 4 mm diameter flat-bottom hole at 62 mm depth. The wideband echo signal corresponding to the correlator output is shown in Fig. 10. The target echo shown here is clearly embedded in grain echoes and does not correspond to the largest echo. The squared correlator output and the resulting optimal processed data for the three algorithms are shown in Fig. 11. These results indicate that all three algorithms recover the hole echo which was indistinguishable from the grain echoes in the original wideband output. This is a significant result since it indicates that these processing techniques are capable of recovering the flaw echo even when it is below the grain noise level. However, as in the titanium data, the minimization algorithm is seen to attain significantly better results compared to the averaging algorithms. The maximum enhancement achieved by the averaging algorithms for the stainless steel data is a factor of two better than in the titanium case. It should be noted, however, that the particular data presented here corresponds to the best enhancement achieved by the averaging algorithms in all the experimental data studied. Therefore, these results may be considered as the upper limit of improvement which can be achieved by the averaging algorithms.

Conclusions

A flaw detection system has been described which uses two complementary techniques to detect flaws in large grained materials with high attenuation. The first technique, was shown to allow detection of flaws buried in background receiver noise. It obtains nearly unlimited signal-to-noise ratio enhancement through the use of a sensitive correlation receiver. A split-spectrum processing technique was then described which first reduces the background noise level by using the random signal correlation system and then improves the flaw-to-grain echo ratio in large grained materials. The enhancement is achieved by partitioning a wideband received spectrum to obtain frequency shifted bands, which are then processed to suppress the grain echoes with respect to the flaw echo using a novel signal minimization algorithm. Experimental data for titanium and stainless steel were presented which show superior flaw detection capabilities for the minimization algorithm with respect to the frequency averaging techniques.

References

- (1) N. M. Bilgutay, E. S. Furgason, V. L. Newhouse, Evaluation of Random Signal Correlation System for Ultrasonic Flaw Detection, IEEE Trans. Sonics and Ultrasonics, Vol. SU-23, (1976) 329-333.
- (2) V. D. Koryachenko, Statistical Processing of Flaw Detector Signals to Enhance the Signal-to-Noise Ratio Associated with Structural Reverberation Noise, Soviet Journal of Non-Destructive Testing, Vol. 11, (1975) 69-75.
- (3) S. Kraus, K. Goebbels, Improvement of Signal-to-Noise Ratio for the Ultrasonic Testing of Coarse Grained Materials by Signal Averaging Techniques, First Int. Symp. on Ultrasonic Materials Characterization, NBS, Gaithersburg, Maryland, (1978).
- (4) V. L. Newhouse, E. S. Furgason, N. M. Bilgutay, J. Sanie, Flaw-to-Grain Echo Enhancement, Proc. Ultrasonics International '79, Graz, Austria, (1979) 152-157.
- (5) M. J. E. Golay, Complementary Series, IRE Trans. on Info. Theory, Vol. II-7, (1961) 82-87.

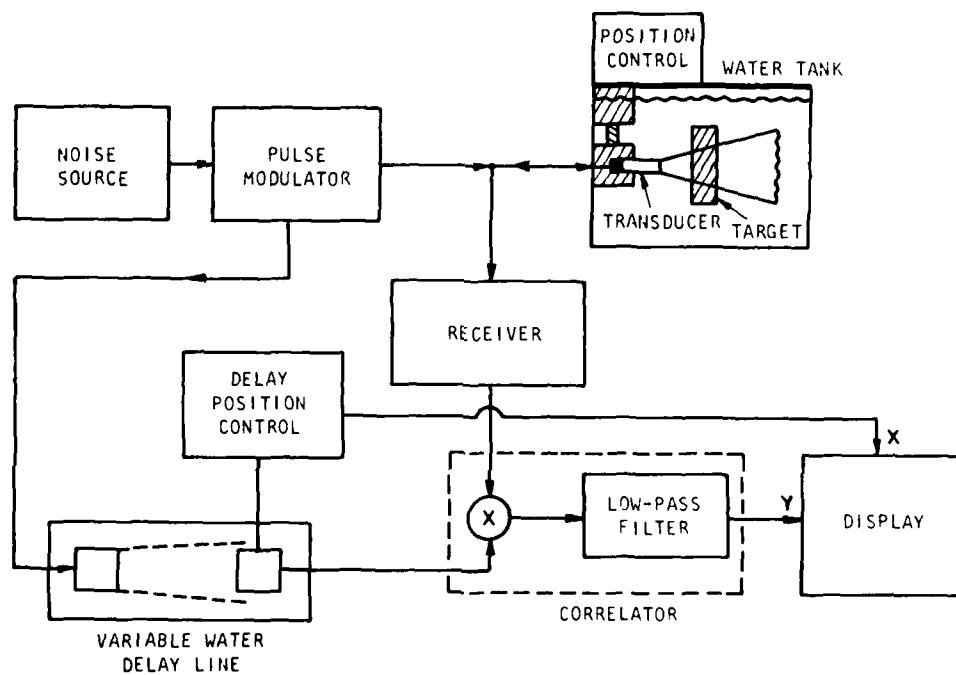


Fig. 1 Original analog random signal flaw detection system.

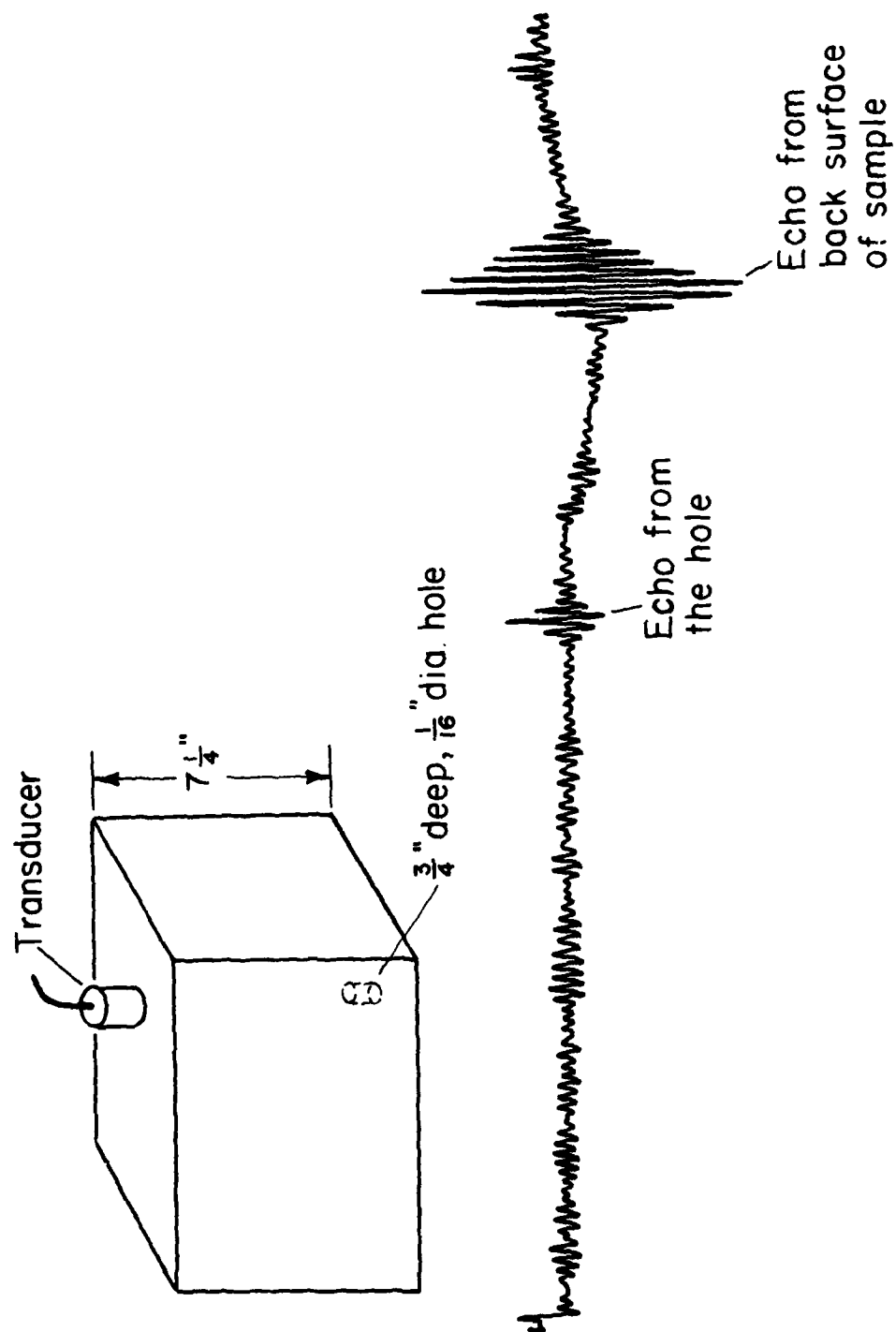


Fig. 2 Detection of a flat-bottomed hole in small grained titanium with less than unity input SNR.

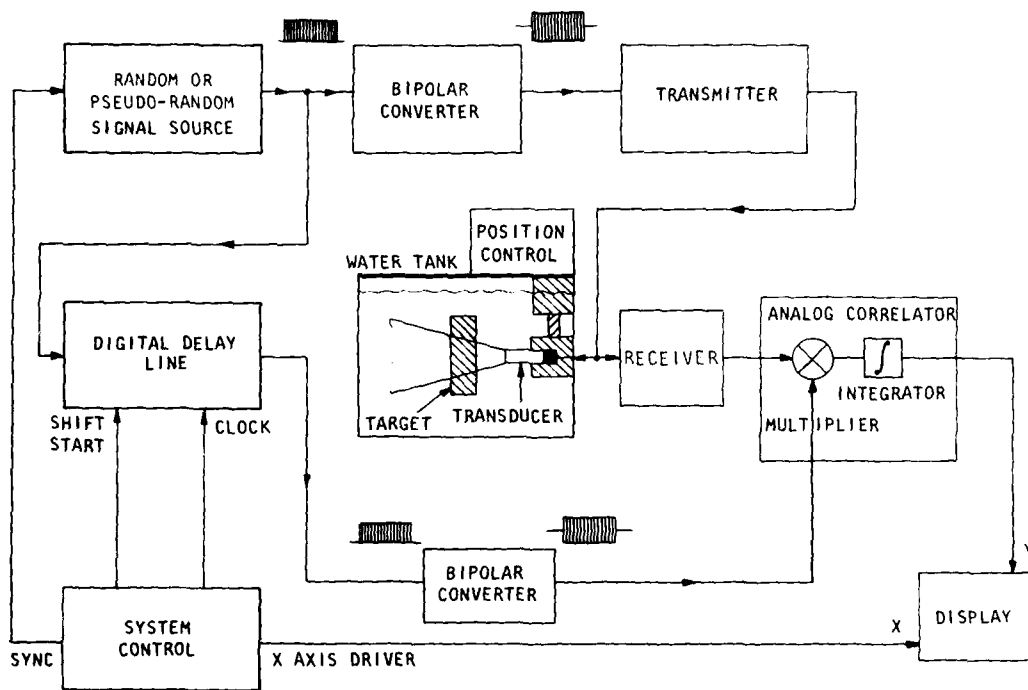


Fig. 3 Block Diagram of Digital Flaw Detection System.

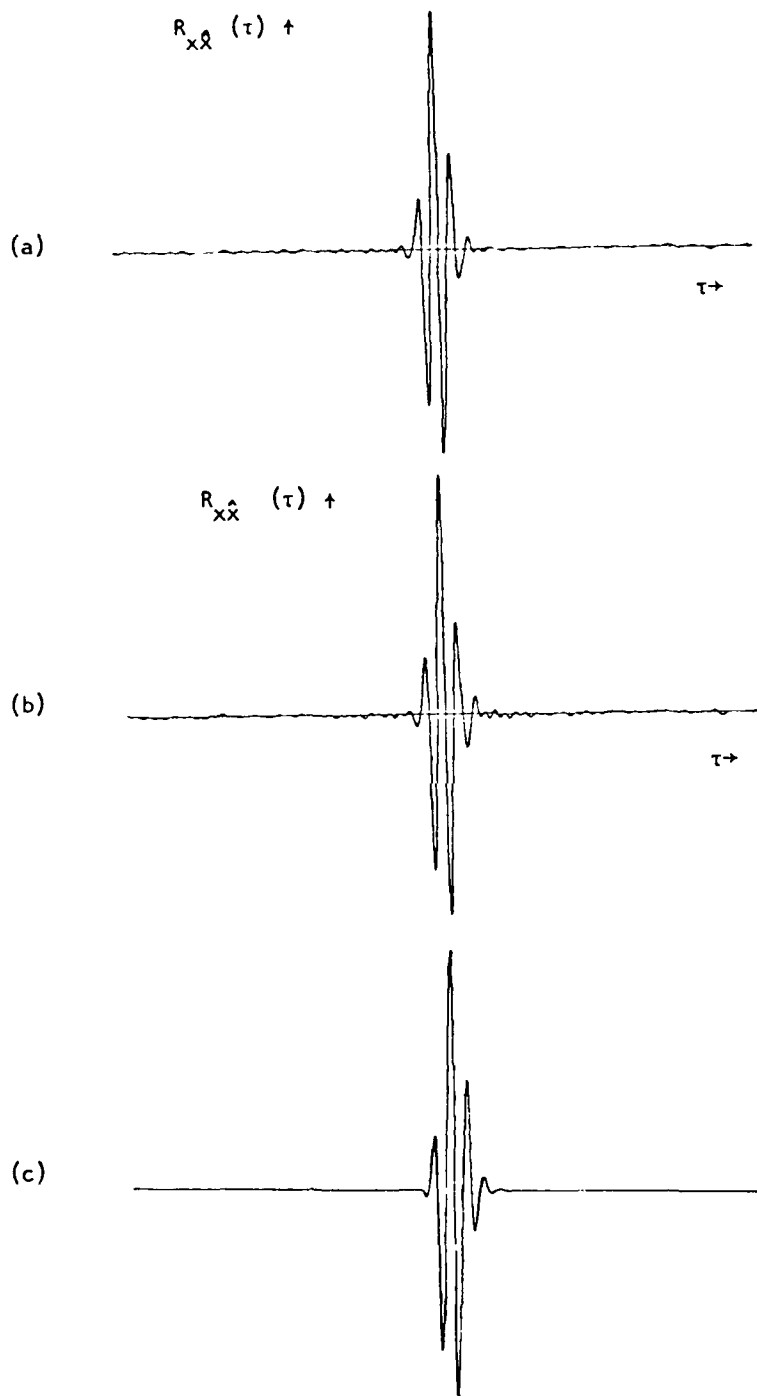
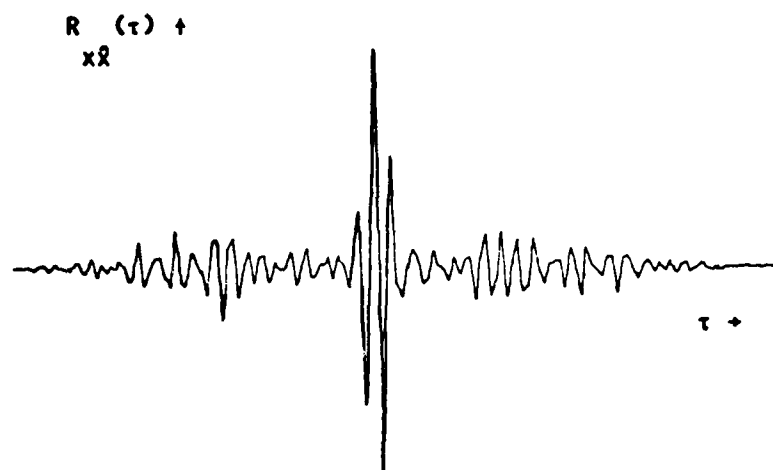


Fig. 4 Comparison of pulse-echo and correlation system outputs.

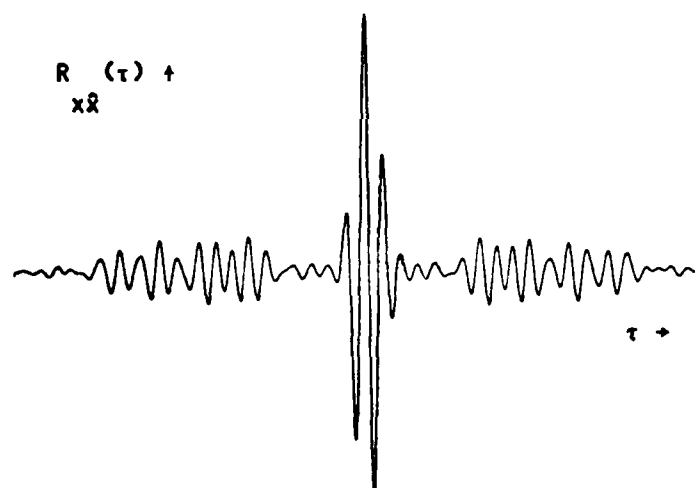
a. Measured correlation output for 198,608 bits of a 8,388,607 bit pseudo-random m-sequence.

b. Measured correlation output for a 198,608 bits of clipped, sampled random signal.

c. Ideal pulse-echo output.



(a)



(b)

Fig. 5 Correlation output for a 64 bit pseudo-random m-sequence.

a. Measured

b. Computer simulated.

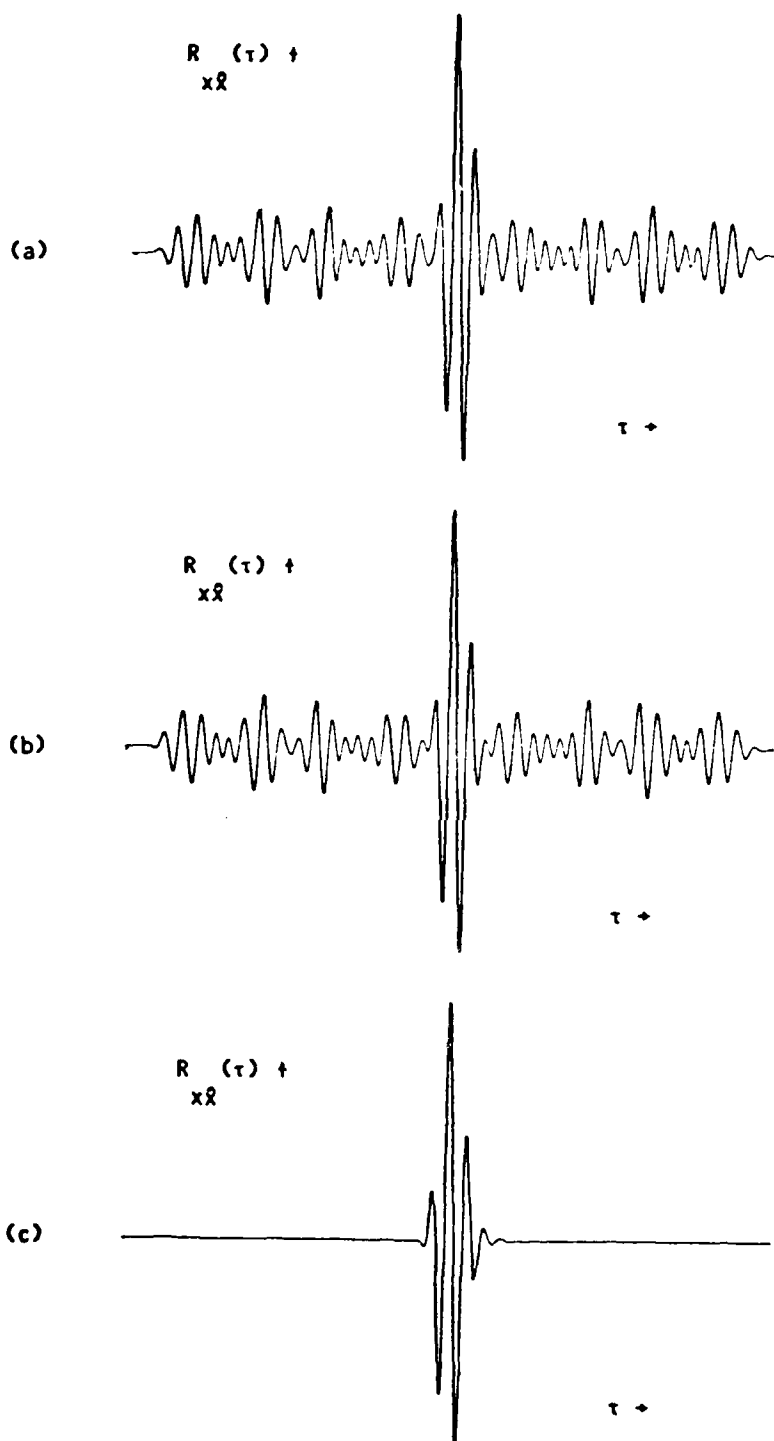


Fig. 6 Computer simulated correlation outputs for 64 bit

- a. Golay code A.
- b. Golay code B.
- c. Normalized sum of a. and b.

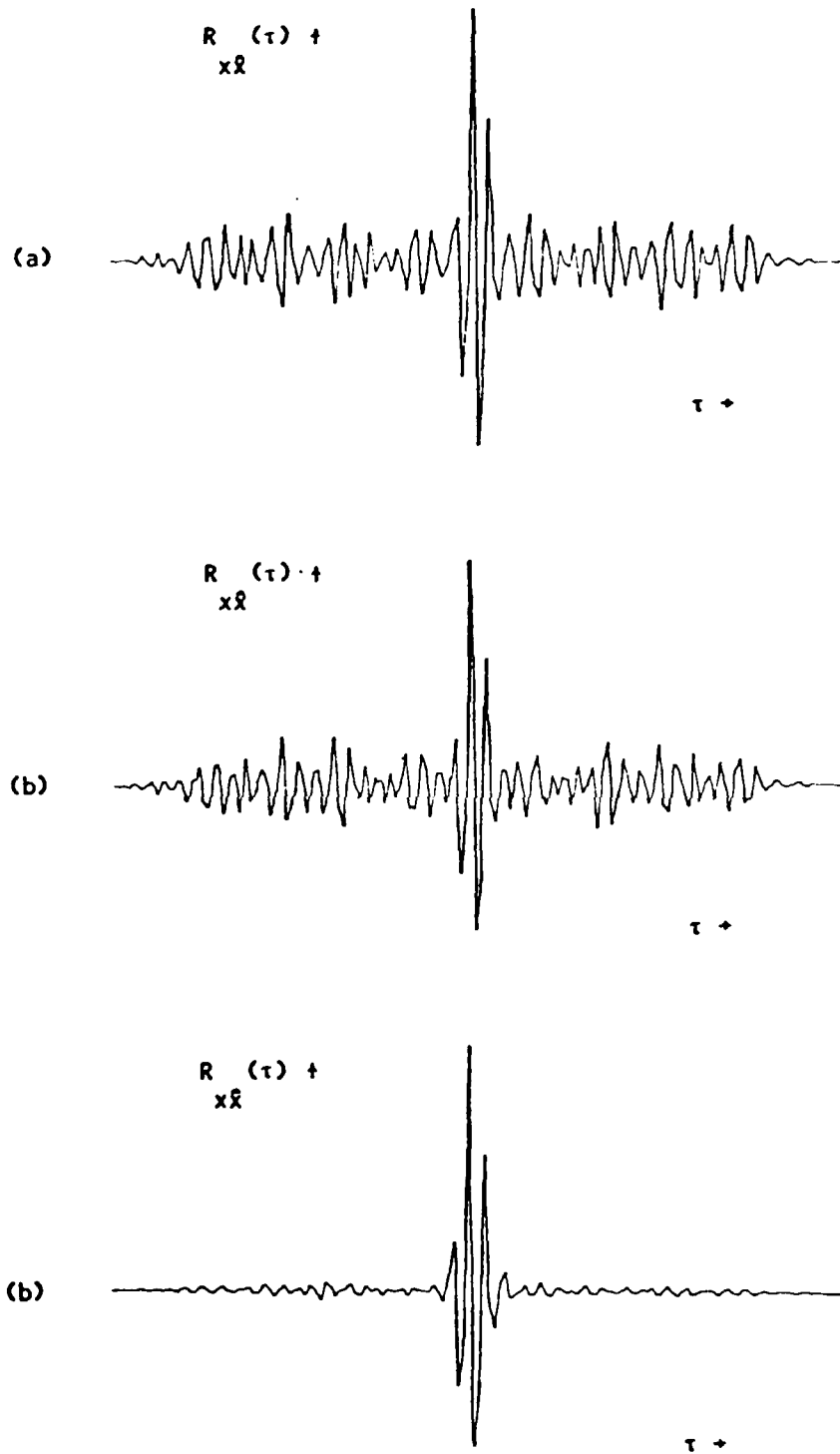


Fig. 7 Measured correlation outputs for 64 bit

a. Golay code A.

b. Golay code B.

c. Averaged sum of a. and b.

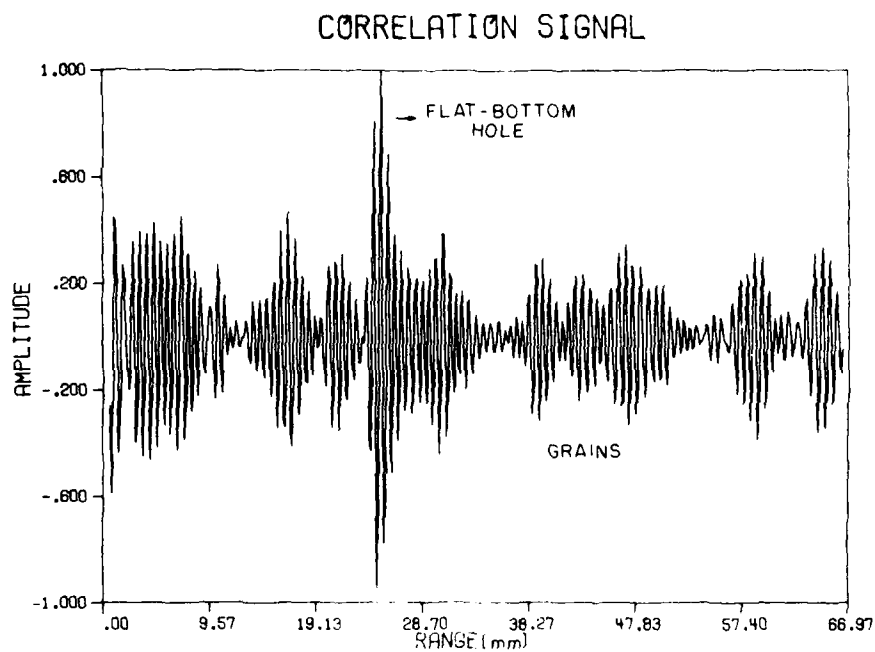


Fig. 8 Correlator output for a titanium sample with 1.19 mm diameter flat-bottom hole.

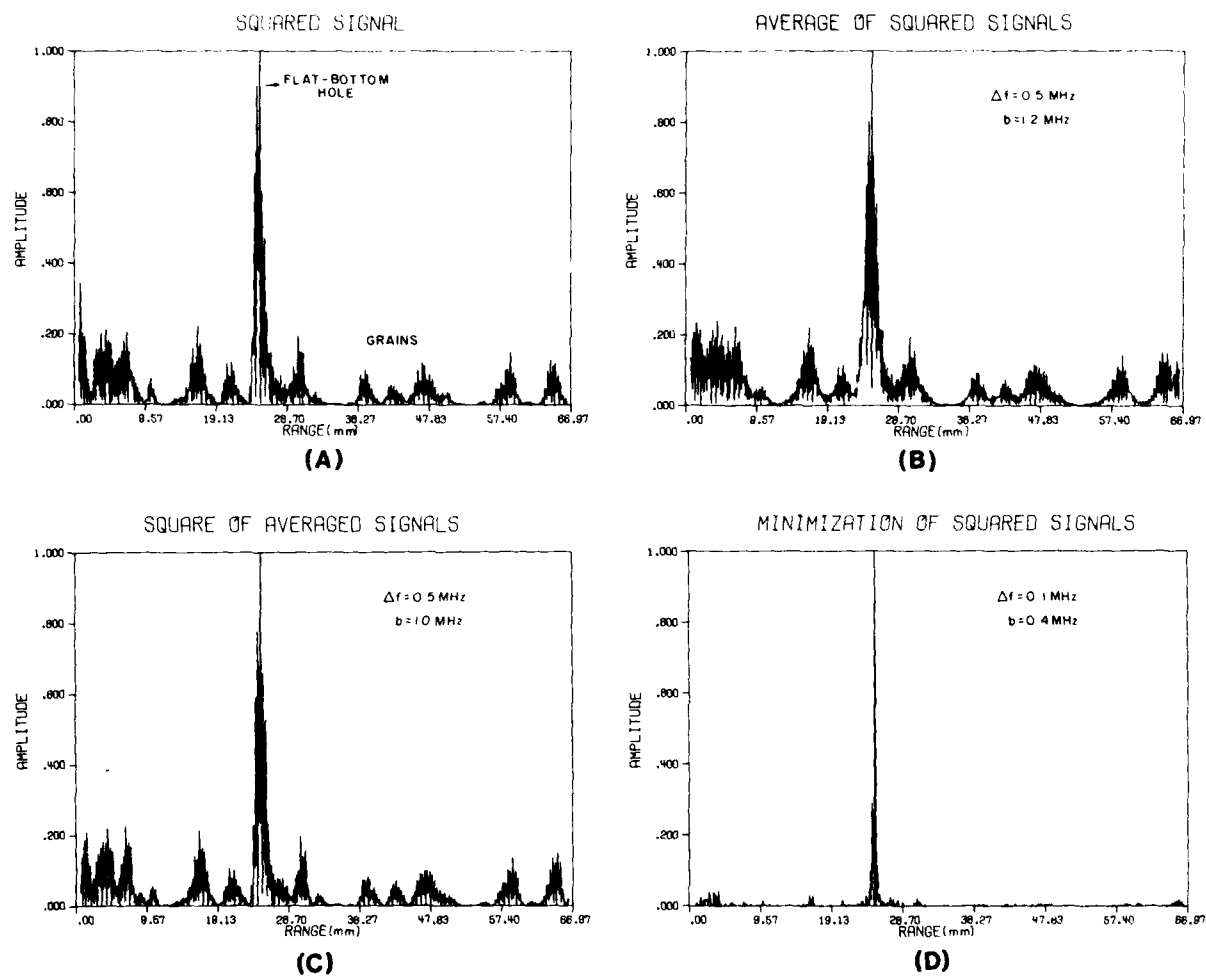


Fig. 9 Titanium data: Squared wideband echo signal and processed outputs for the three algorithms.

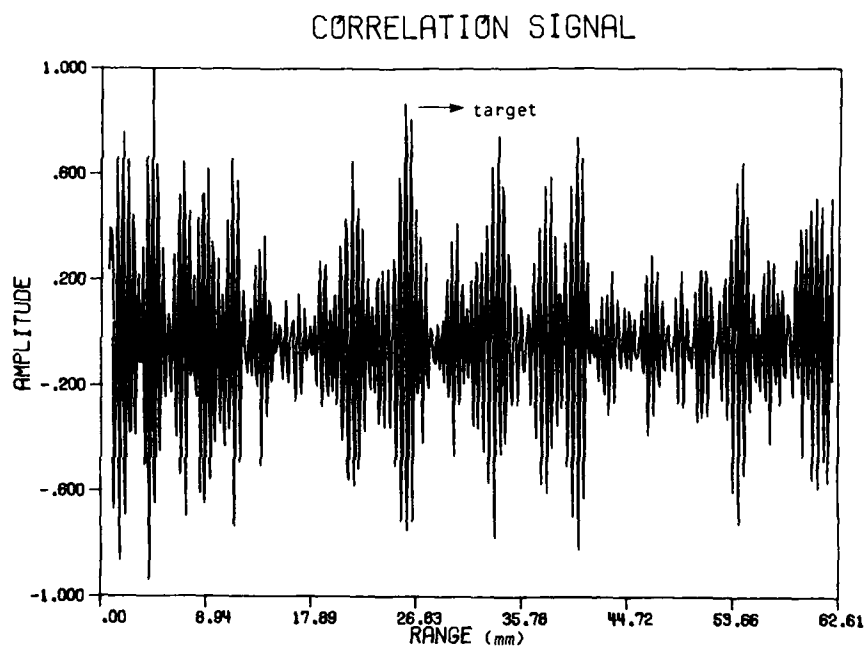


Fig. 10 Correlator output for a stainless steel sample with 4 mm diameter flat-bottom hole.

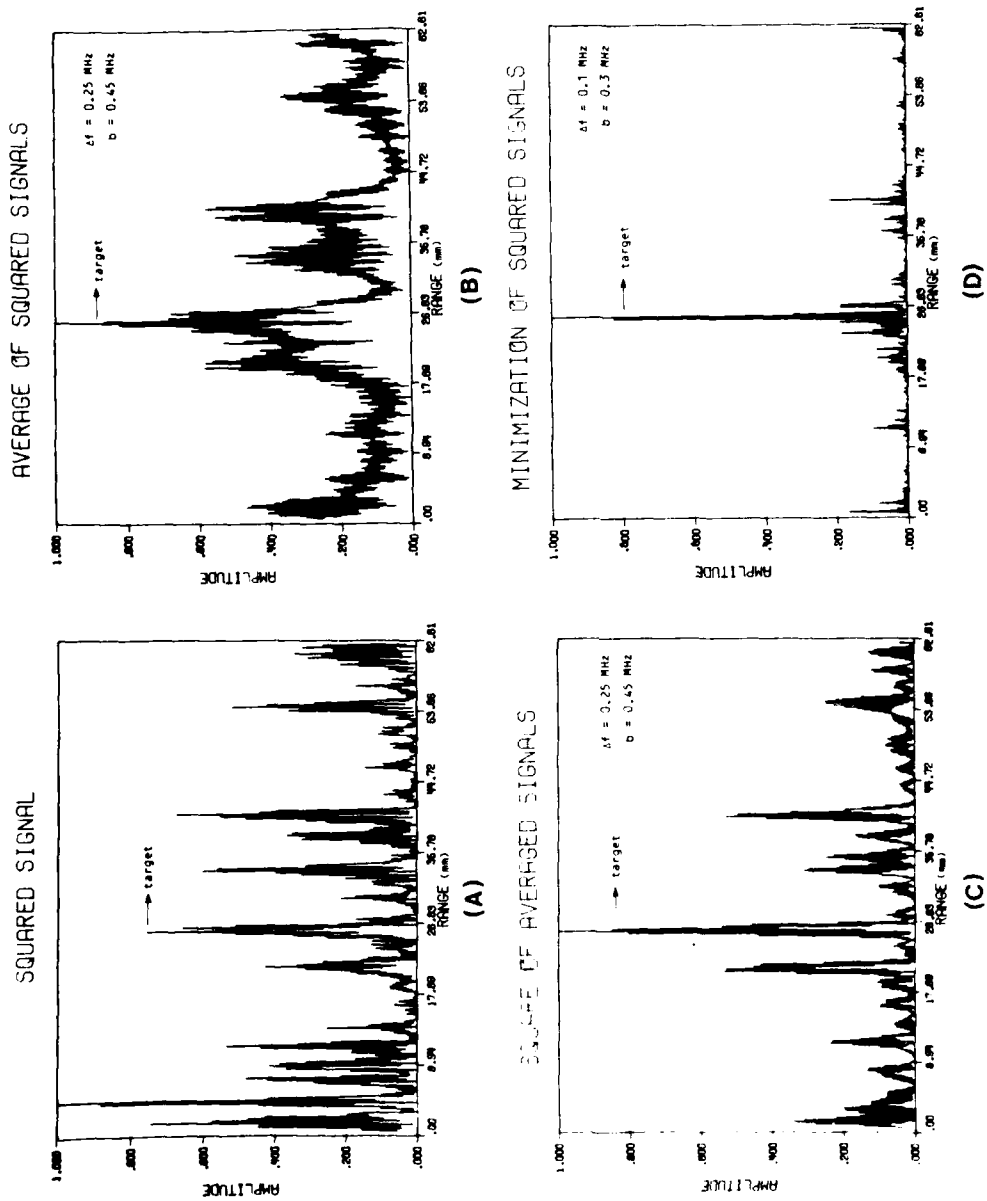


Fig. 11 Stainless steel data: Squared wideband echo signal and processed outputs for the three algorithms.

ALN 4000 ULTRASONIC PIPE INSPECTION SYSTEM

Anthony N. Mucciardi

*Adaptronics, Inc.
McLean, VA 22102*

This paper presents examples of S/N enhancement and detection using a variety of signal processing techniques that have been applied successfully to problems of comparable complexity. The application of a pattern recognition algorithm—adaptive learning (ALN)—following the S/N enhancement and detection is described along with the defect classification and sizing results obtained.

The implementation of both procedures into a field-portable, microprocessor-based advanced NDE instrument, namely ALN 4000 Ultrasonic Pipe Inspection System is described.

1. INTRODUCTION

The purpose of the ALN 4000 Pipe Inspection System is to detect, locate, and size circumferential intergranular stress corrosion cracks (IGSCC's) in the heat affected zones (HAZ) around welds in stainless steel pipes. The system uses ultrasonic instrumentation to sense anomalies in the pipe and employs Adaptive Learning Networks (ALN's) to distinguish IGSCC's from other types of anomalies and to estimate the lengths and depths of these cracks. Inspections are performed automatically with manual assistance required only to calibrate the ultrasonics, mount the mechanical scanner on the pipe, start the system, and interchange the normal (0°) and 45° transducers between the pipe Thickness Scan and the anomaly Detection Scan.

In summary, an ALN 4000 pipe inspection consists of the following operations:

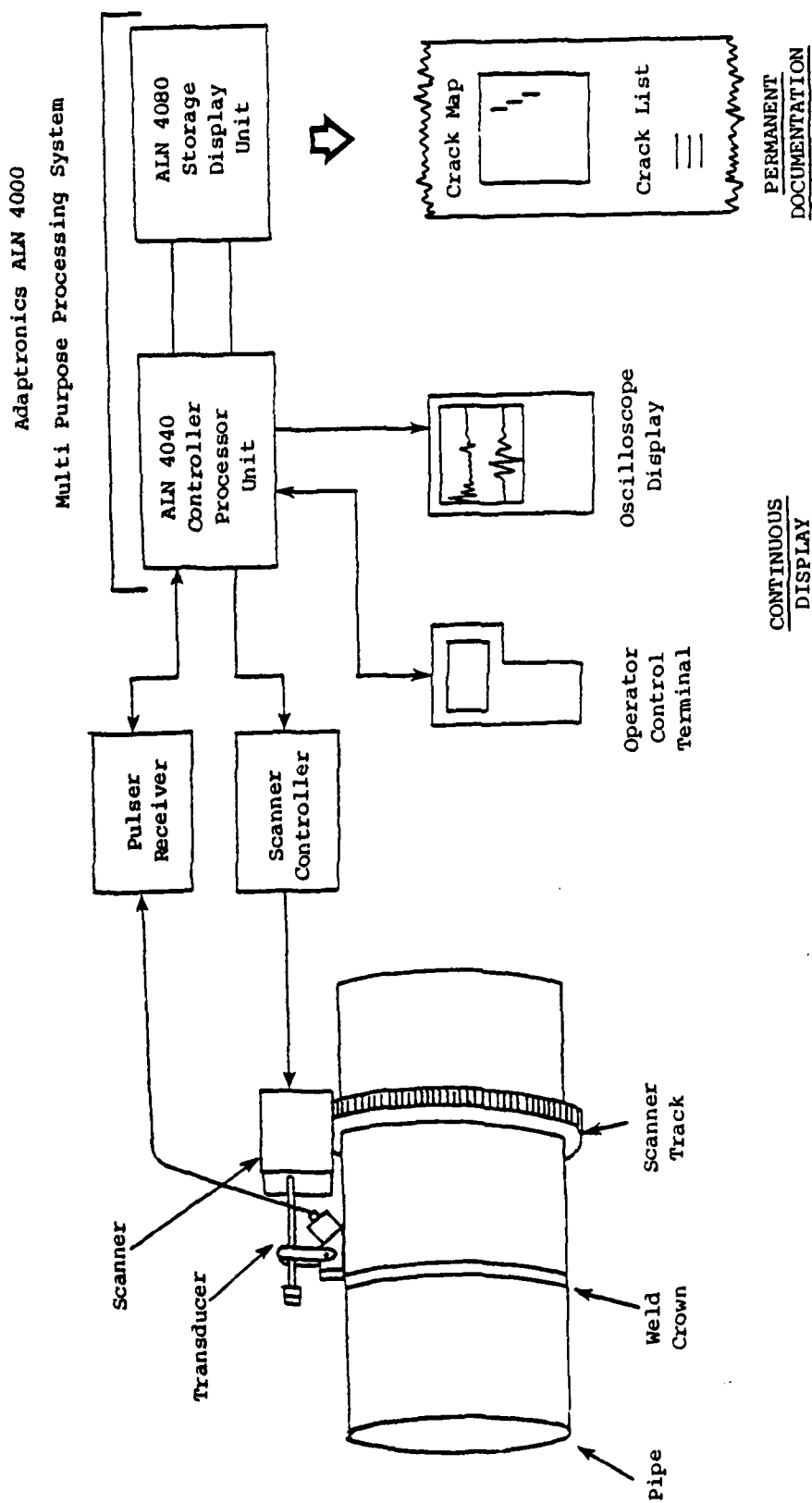
1. System Calibration - Distance, amplitude, distance amplitude corrections (DAC) and matched filter calibrations are performed. Calibration is done automatically; however, the transducer is positioned manually.
2. Thickness Scan - The thickness profile of the pipe is measured, with a normal transducer, at 8 circumferential positions around the pipe. These pipe thickness data are used for ray tracing.
3. Detection Scan - The system scans the inspection region, on one side of the weld, and generates an Anomaly Map based either on RF signal-to-noise ratio or percent DAC as a function of position on the inner surface of the pipe.

4. Detection Association Process - Adjacent points in the Anomaly Map which have detection amplitudes above a given threshold are associated with each other and the associated region is defined to be an anomaly. An anomaly may be any reflector: a crack, a void, geometry, etc. A list of anomalies and their centroid locations is prepared from the Anomaly Map.
5. Characterization Scan - The scanner returns to each anomaly in the Anomaly List and an ALN classification is performed to determine whether the reflector is an IGSCC. If the reflector is classified as a crack, estimations are made of its length and depth. The list of cracks is printed out along with a coarse plot of the crack locations.
6. Calibration Check - The amplitude responses from the calibration side-drilled hole (SDH) are checked to determine that there has been no significant change in ultrasonic sensitivity during the inspection.

A block diagram of the ALN 4000 Pipe Inspection System is shown in Figure 1.

AUTOMATIC SCANNING

AUTOMATIC FLAW DETECTION AND CHARACTERIZATION



CONTINUOUS
DISPLAY

PERMANENT
DOCUMENTATION

FIGURE 1: ALN 4000 PIPE INSPECTION SYSTEM

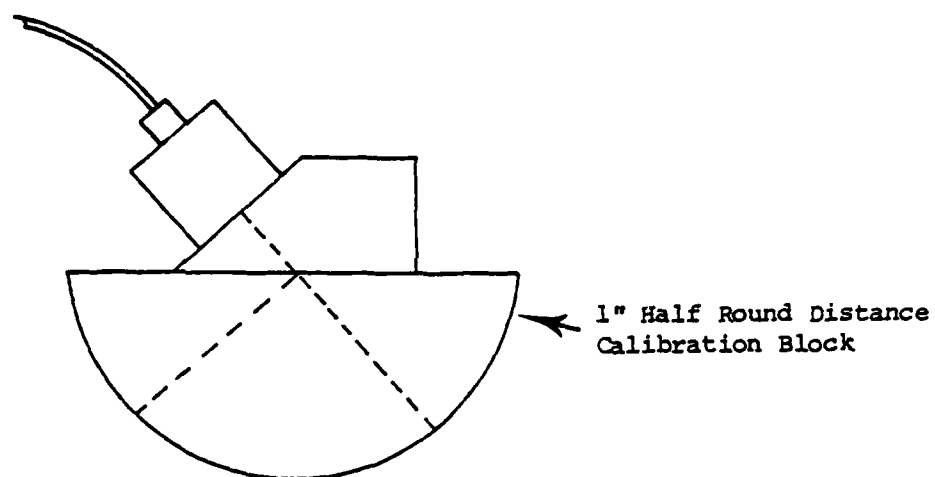
2. SYSTEM CALIBRATION

As in conventional manual inspections, distance, amplitude, and DAC curve calibrations are performed in an ALN 4000 inspection. In addition, a reference shot is taken on a 3/32" round bottom hole; this reference waveform represents the point source or "impulse" response of the pulser/transducer/receiver combination and is used subsequently as the characteristic of the matched filter.

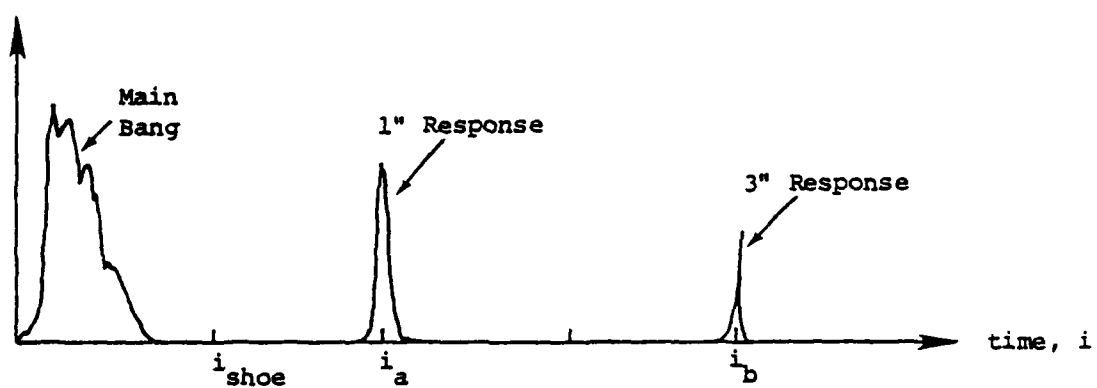
2.1 DISTANCE CALIBRATION

As shown in Figure 2a, a 1" radius half-round calibration block is used to perform the distance calibration. The transducer is manually placed on the block, and the resulting waveform response, shown in Figure 2b, is displayed on the oscilloscope screen. When the operator has maximized the resonant responses, he keys the GO button on the hand-held operator's terminal and the ALN 4000 performs the distance calibration.

First a peak-seeking routine in the ALN 4000 locates the time points of the 1" and 3" responses. Since the digitized waveform is a sampled signal, the time base is computed in terms of a sample index i . Sampling of the waveform begins when the pulser is triggered, so $i=1$ corresponds to the trigger time. The occurrence times of the 1" and 3" responses are designated i_a and i_b . To determine the number of time samples per inch of material, i_a is subtracted from i_b and the difference is divided by 2. This number, i_{cal} , is the distance calibration constant:



(a) Transducer Setup for Distance Calibration



(b) Time Waveform Response from Distance Calibration

FIGURE 2: DISTANCE CALIBRATION

$$i_{cal} = (i_b - i_a)/2 \quad (\text{samples/inch}) \quad (1)$$

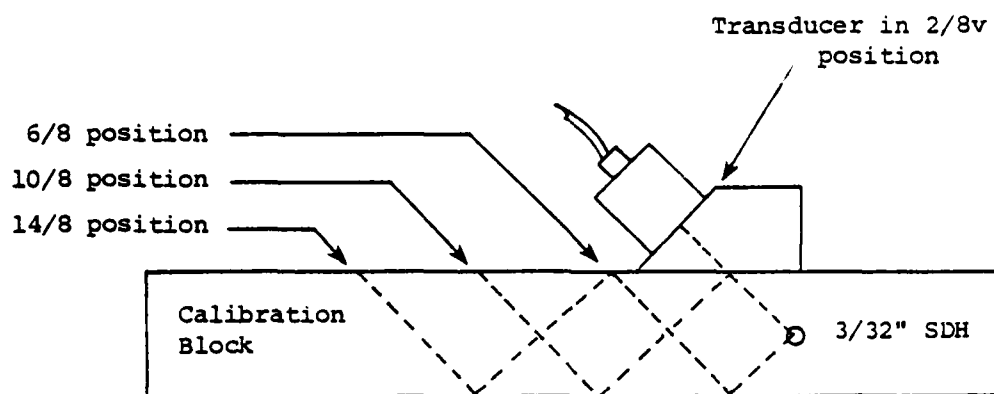
Next the shoe delay, i_s , which corresponds to the time that the beam enters the metal, is computed. Though there is no waveform response at this point, it is computed by subtracting the calibration time constant, i_{cal} (one inch's worth of points) from the 1" response time:

$$i_s = i_a - i_{cal} \quad (2)$$

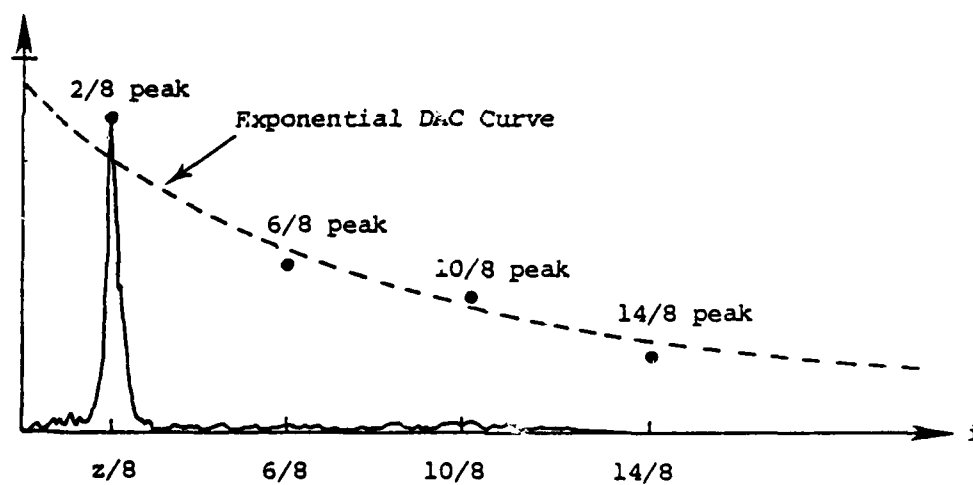
The i_{cal} and i_s parameters are used throughout the remaining signal processing. From here on, all of the rectified waveforms displayed on the oscilloscope are time-shifted and scaled to begin at i_s , i.e., the metal entry point, and to end at the number of metal-path inches specified by the user.

2.2 AMPLITUDE CALIBRATION

As shown in Figure 3a, amplitude calibration is performed using a calibration block with a 3/32" side-drilled hole (SDH) located midway between the two pipe wall surfaces. First the transducer is manipulated by the inspector to provide the 2/8's v response. When he has this response properly maximized, as shown in Figure 3b, he adjusts the pulser/receiver gain/attenuation to obtain a 75±5% amplitude response on the oscilloscope. He keys the GO button and the ALN 4000 checks that the amplitude is within the required range. If not, the inspector is asked to recalibrate. At the completion of the calibration, the operator is asked to key into the ALN 4000 the gain and attenuation settings on the pulser/receiver, and the DAC curve calibration begins.



(a) Transducer Setup for Amplitude and DAC Calibration



(b) Time Waveform Response from DAC Calibration

FIGURE 3: AMPLITUDE AND DAC CURVE CALIBRATION

AD-A119 066

NAVAL RESEARCH LAB WASHINGTON DC F/6 11/6
PROCEEDINGS OF THE FIRST WORKSHOP ON NONDESTRUCTIVE EVALUATION --ETC(U)
JUN 82 O P ARORA, H H CHASKELIS, N K BATRA

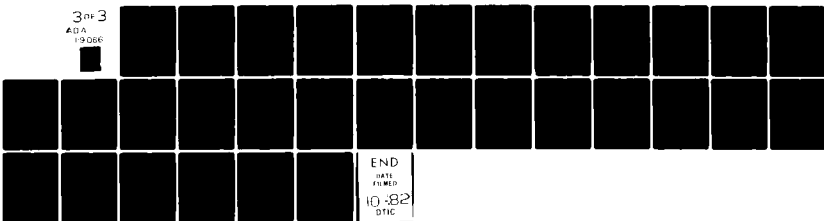
UNCLASSIFIED

DTNSRDC/SME-CR-14-82

NL

3 of 3

ADA
19066



2.3 DAC CURVE CALIBRATION

Calibration of the distance amplitude correction (DAC) also uses the SDH cal block. During the gain calibration, the ALN 4000 noted the time and amplitude of the 2/8's v response. The inspector moves the transducer to the 6/8's v position, and upon depression of the GO key, the ALN 4000 detects the peak value and time of occurrence of the SDH for that transducer position. This procedure is repeated for the 10/8's v and 14/8's v positions. At each of these four positions, the inspector marks the peaks on the oscilloscope face with a grease pencil.

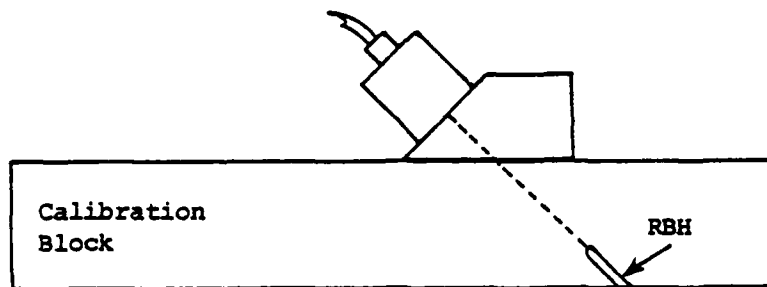
The ALN 4000 computes an exponential curve to best fit the four peaks. This curve represents 100% DAC, and it is displayed on the scope. If the curve is satisfactory to the inspector, he traces it with the grease pencil for future reference. If it is not acceptable, he may repeat the calibration process at any number of the four transducer positions, and the ALN 4000 will refit the curve.

The coefficients of the exponential curve and the corresponding values at each time sample (i.e., the DAC time waveform) are stored in memory along with the four peak points used to compute the curve.

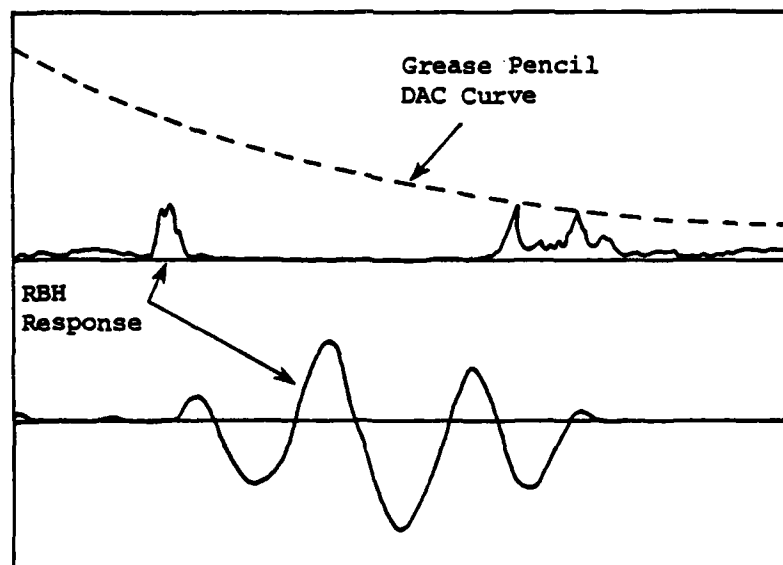
In subsequent signal processing, all signals, with the exception of the displayed rectified waveform, are corrected for distance through multiplication by a gain curve which is the reciprocal of the DAC curve.

2.4 MATCHED FILTER CALIBRATION

To obtain the weights for the matched filter, the inspector positions the transducer to provide a maximum response from the reference round bottom hole (RBH) in the calibration block. (See Figure 4a.) As shown in Figure 4b, a time-expanded and amplitude-corrected version of the RBH response is shown on the lower half of the oscilloscope. When the signal appears correctly, the inspector keys GO and the reference response is stored for use in the matched filter processing.



(a) Transducer Position for Matched Filter Calibration



(b) Waveform Display for Matched Filter Calibration

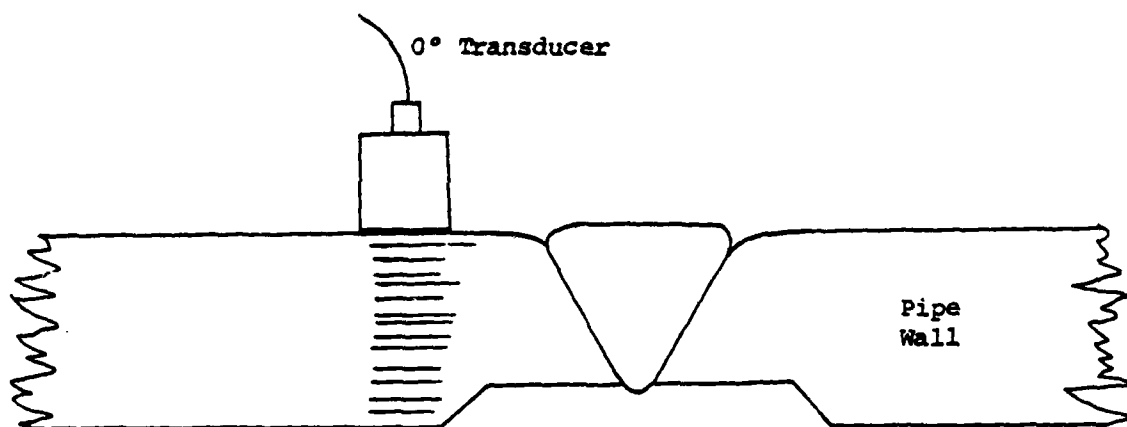
FIGURE 4: MATCHED FILTER CALIBRATION

3. THICKNESS SCAN (TS)

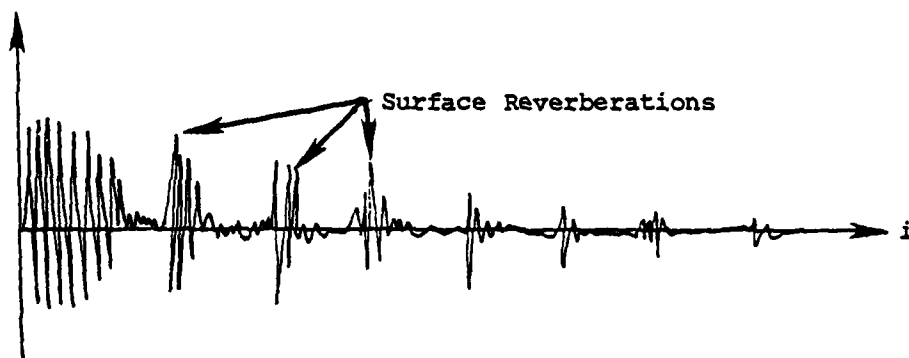
Prior to searching for defects in the pipe, a Thickness Scan (TS) is performed to determine the thickness and counterbore profile of the pipe. The resulting pipe thickness contours are used in the subsequent portions of the inspection to trace the UT rays in the pipe wall and to compute the transducer positions and ultrasonic time windows which are required to inspect locations on the inner surface of the pipe.

As shown in Figure 5, a normal (0°) transducer is used to perform the TS. At eight equally spaced circumferential locations, the scanner performs an axial scan and develops a map of the pipe thickness as a function of the axial distance from the center of the weld. The depth at each axial point is computed from the ultrasonic pulse resonance period between the inner and outer surfaces of the pipe wall. The map at each circumferential location is assumed to be a piecewise linear contour consisting of three segments: (1) the pipe's unmachined inner surface, (2) the angled portion of the counterbore, and (3) the flat portion of the counterbore.

Because of the weld crown surface geometry, it may not be possible to obtain good thickness measurements from the weld centerline out to a position about half the transducer diameter beyond the edge of the weld. If the thickness in this region cannot be measured directly, as evidenced by the lack of measurable metal surface reverberations in the ultrasonic signal, a thickness profile for this region is assumed. First a check is made to determine whether the counterbore occurs within the region which can be measured. If so, this



(a) Transducer Position for Thickness Scan



(b) Waveform Response for Thickness Scan

FIGURE 5: NORMAL TRANSDUCER FOR THICKNESS SCAN

counterbore is assumed to extend uniformly to the weld centerline, and the thickness for the unmeasured region is set (to a constant) equal to the thickness as measured at the closest measurement to the weld. If there is no counterbore detected in the measurable region, it is assumed that a counterbore exists under the weld crown and that it has the nominal dimensions of 1/16 inch depth, 3/16 inch flat length, and 3/16 inch taper length.

4. RAY TRACING USING THE THICKNESS PROFILE

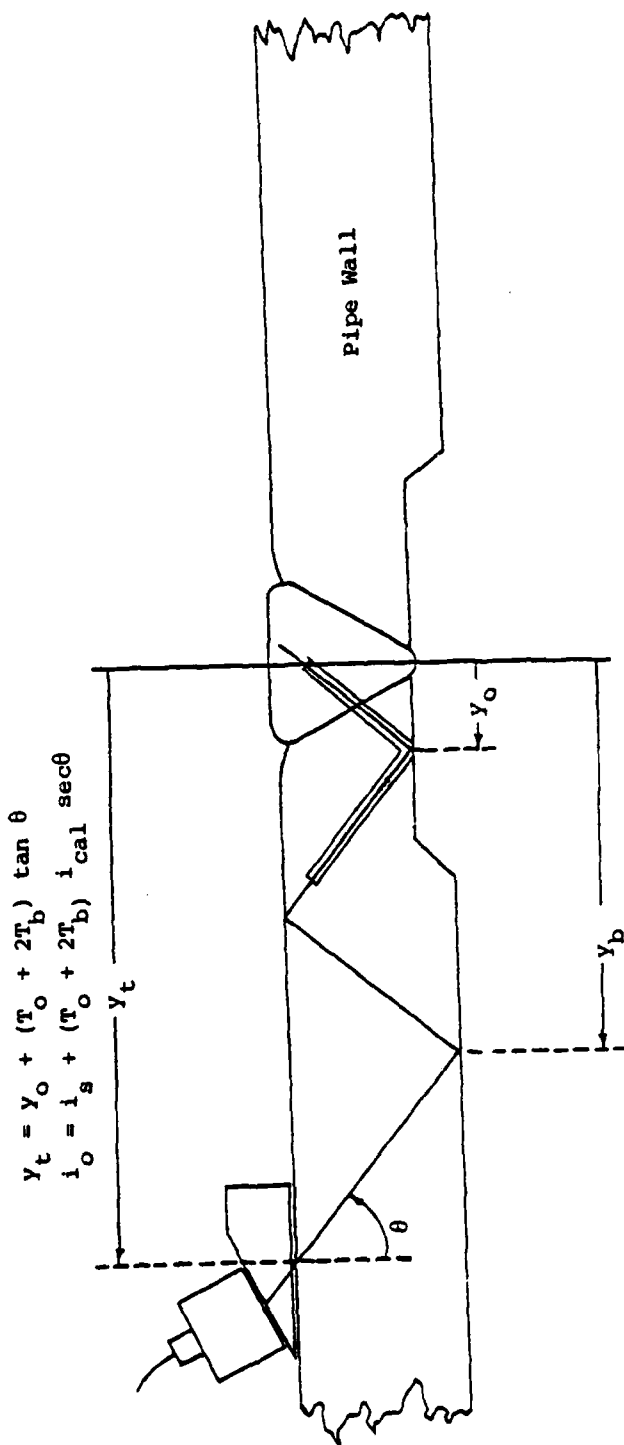
Ray tracing is used (1) during the Detection Scan to compute the transducer position and the UT window parameters such that the window is physically centered around the desired intercept point, and (2) during the Characterization Scan to determine the precise location of a reflector from the transducer location and from the occurrence time of the reflector within the UT signal.

4.1 RAY TRACING IN THE DETECTION SCAN

The ray trace geometry for the Detection Scan is shown in Figure 6. To inspect a region of the inner pipe surface around a point which is a distance y_0 from the weld center, it is desired to position the transducer such that the center of the transducer main beam intercepts the point y_0 . The transducer position is equal to the position y_0 of the inspection point plus the axial displacement due to the 1-1/2 V pattern. The displacement is a function of the shear wave entry angle θ , the thickness T_b of the pipe at the point x_b where the beam first bounces off the inner surface, and the thickness T_0 at the inspection point. The equation for the desired transducer position y_t is:

$$y_t = y_0 + (2T_b + T_0) \tan \theta \quad (3)$$

where the $2T_b$ term accounts for the first two legs of the 1-1/2 V pattern, the T_0 term accounts for the third, and the $\tan \theta$ term converts the pipe wall thicknesses to the axial component of the travel path.



y_o = axial position of the desired inspection point on the inner surface

y_t = transducer axial location required to inspect point y_o

y_b = axial position of the first inner surface bounce

T_o = pipe thickness at position y_o

T_b = pipe thickness at position y_b

θ = shear wave entry angle

i_o = time that the pulse reaches intercept point y_o

t_s = shoe delay


 analysis window

FIGURE 6: RAY TRACING FOR THE DETECTION SCAN

It is desired that the center of the analysis window occur at the time i_o when a pulse echo from the intercept point y_o is recorded at the transducer. Time is defined to begin when the transducer is triggered. The intercept time i_o consists of the round trip travel time through the shoe and through the 1-1/2 V pattern:

$$i_o = i_s + (2T_b + T_o) i_{cal} \sec \theta \quad (4)$$

where i_s is the shoe delay (from Equation 2), the $\sec \theta$ term converts the wall thickness to ultrasonic travel path length, and the i_{cal} (from Equation 1) converts travel path length to travel time.

4.2 RAY TRACING IN THE CHARACTERIZATION SCAN

The objective of ray tracing in the Characterization Scan is to determine the axial and radial locations of a reflector. In the following equations it is assumed that the transducer has been positioned such that the reflector lies along the center of the transducer main beam. The centering is accomplished by dithering the transducer axial position until the magnitude response of the matched filter output is maximized. With the transducer properly "peaked up," the axial location y_r of a reflector is computed from the transducer position y_t and the reflector occurrence time i_r within the UT signal:

$$y_r = y_t - \frac{(i_r - i_s) \sin \theta}{i_{cal}} \quad (5)$$

axial travel path in metal

where the reflection occurrence time minus the shoe delay $(i_r - i_s)/i_{cal}$ is the round trip distance in metal and the \sin term converts total travel path distance to the axial component of the path. (See Figure 7.) (Note that the calculation of the reflector's axial position y_r by Equation 5 does not depend on pipe thickness profile. This holds true, however, only if the reflector is centered on the transducer beam and if the reflecting surfaces are parallel.)

In theory, the radial position z_r of the reflector away from the inner surface may also be determined. If the occurrence time i_r coincides with the ideal surface intercept time i_o computed for the transducer located at its peaked up location then, by the definition of i_o , the reflector occurs at the surface. Any difference between these two times indicates a radial displacement z_r of the defect from the surface:

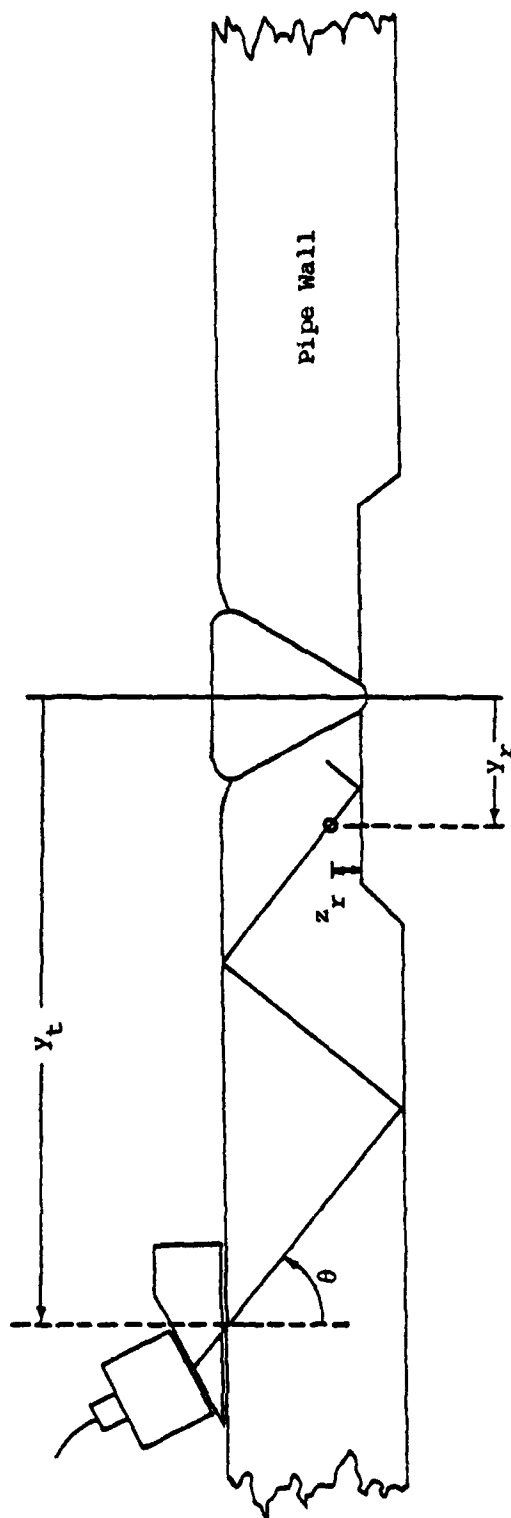
$$z_r = \frac{|i_o - i_r|}{i_{cal}} \cos \theta \quad (6)$$

where the magnitude of the time difference $|i_o - i_r|$ indicates the reflector occurrence time prior to or subsequent to the beam striking the surface, and the $\cos\theta/i_{cal}$ converts the time to the vertical component of the travel path in metal.

The accuracy of the radial displacement measurement of Equation 6 is limited, however, due to possible compounding of error in (a) the wall thickness measurement, which affects the window center time i_o computed from Equation 5, and (b) the transducer positioning during the UT peak up, which affects the

$$y_r = y_t - \frac{(i_r - i_s) \sin \theta}{i_{cal}}$$

$$z_r = \frac{|i_o - i_r|}{i_{cal}} \cos \theta$$



y_r = axial position of the reflector

z_r = radial position of the reflector

y_t = transducer location when reflector is peaked up

FIGURE 7: RAY TRACING FOR THE CHARACTERISTIC SCAN

reflection occurrence time i_r . Thus, only reflectors which are measured to be more than one third the wall thickness from the inside may be ruled out as being IGSCC's, based upon radial location.

5. DETECTON SCAN (DS)

5.1 THE DETECTION SCANNING SEQUENCE

The Detection Scan (DS) performs a general survey of the inner surface of the pipe over the heat affected zone and the counterbore region. The width of the region to be inspected (on one side of the pipe is defined to be W , where W extends from the weld centerline to a point one nominal wall thickness T_{nom} beyond the edge of the weld. If, in the Thickness Scan, the counterbore is determined to extend beyond the T_{nom} point, W is increased to include the full counterbore so that the inspection will cover all of the cold-worked area around the weld.

A series of C equally spaced circumferential scans are performed over the region W . Each scan begins with the scanner at the 0° circumferential position.¹ The axial position of the transducer is maintained constant throughout each circumferential scan and is incremented by an amount W/C between scans.

5.2 THE ANOMALY MAP

The Detection Scan generates a map of pipe anomalies. As shown in Figure 8, the Anomaly Map (AM) consists of a grid of points on both sides of the weld.

¹For horizontal pipes, 0° is defined to be top dead center, and for vertical pipes the 0° position must be defined specifically for each weld. For "free" pipes, the 0° position may be specified arbitrarily, but should then be mounted in the test jig such that the designated 0° position is at top center.

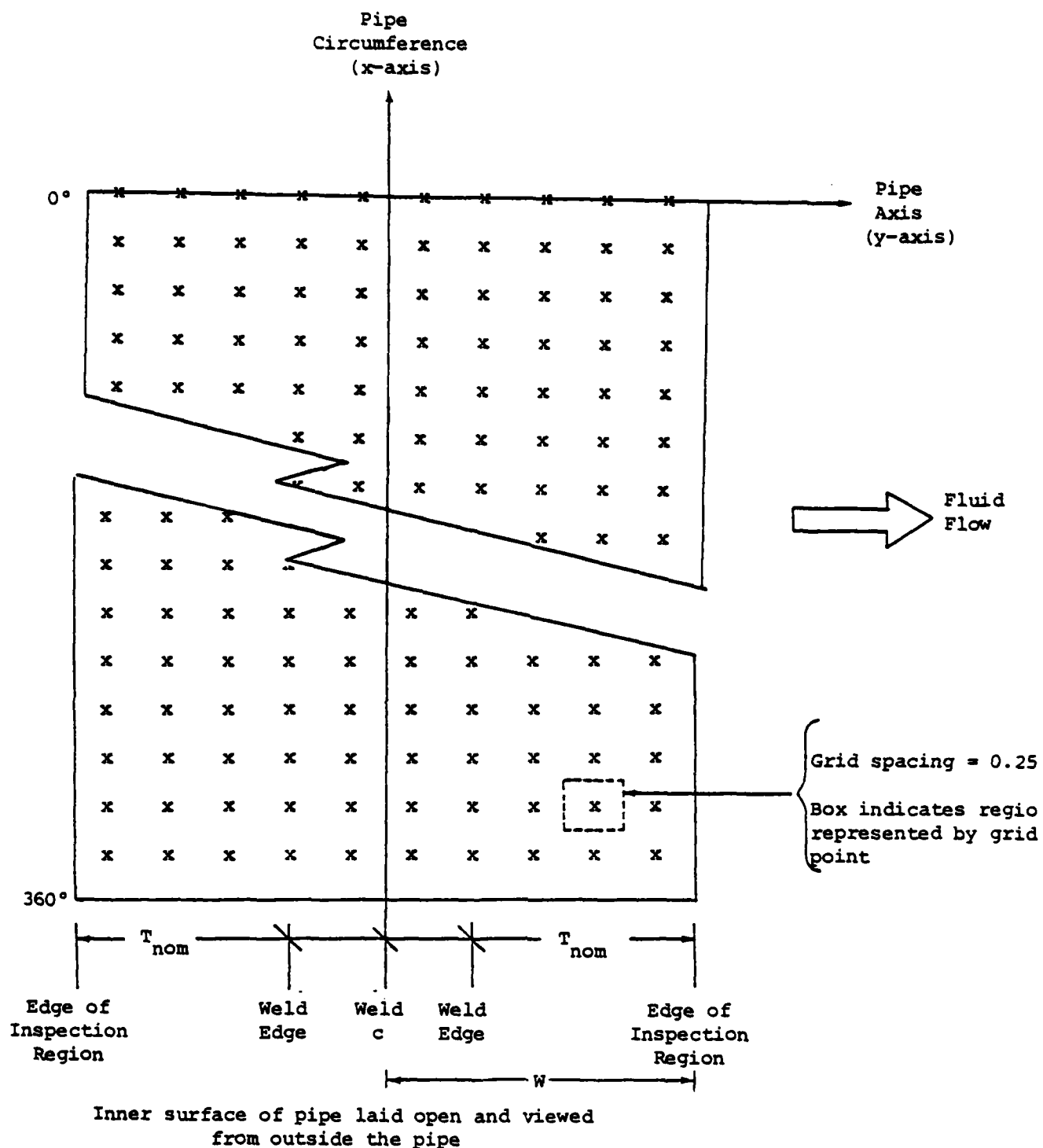


FIGURE 8: PIPE ANOMALY MAP - GRID LOCATIONS ON INNER SURFACE OF THE PIPE

The grid extends axially from the weld centerline to points one nominal-wall-thickness T_{nom} beyond the edges of the weld or to the end of the counterbore, whichever is further. The grid extends 360° circumferentially around the pipe. Each point on the grid represents the quarter-inch square region surrounding it, and the number stored in the corresponding memory location indicates the highest DAC reading received from an anomaly anywhere in the designated region. The resulting map is a contour of percent DAC as a function of pipe position, and it may be interpreted as an amplitude-versus-position profile.

As the scan proceeds and the transducer spot passes over the pipe inner surface, detections are performed on the windowed portions of the ultrasonic signals. The detection window spans several axial cells in the AM. The detection window is divided into regions corresponding to the cells in the anomaly map. The relationship between the waveform regions and map cells depends upon the transducer position and the pipe thickness profile (Equation 5). The peak DAC value is determined over each region, and that peak value is recorded in the corresponding AM cell. Because there is spot overlap from one circumferential scan to the next, two levels of response may be detected for the AM cell. The highest value is always kept. Thus, a value is recorded only if it is higher than a previously recorded value, and in that case the previous value is overwritten.

5.3 WAVEFORM AVERAGING

Ultrasonic data shots are taken while the scanner is in circumferential motion. To achieve both spatial and temporal averaging, a series of ten UT

shots are taken while the scanner is in motion and the RF waveforms are averaged. (Because there is no axial motion, the time waveforms are averaged directly without time shifting.) The ten shots are taken over a circumferential span of approximately 1/8 inch, where the span is centered around the circumferential location of the corresponding anomaly map grid points. The processing of the composite waveform, i.e., detection and recording of anomalies, occurs during the remaining 1/8 inch traverse to the next grid point.

5.4 CONVENTIONAL DETECTION LOGIC

As illustrated in Figure 9, the conventional detection logic, which is performed over the analysis window (see Section 4.1), consists of DAC compensation, full wave rectification, and detection of maximum DAC over regions corresponding to axial cells in the Anomaly Map. This DAC compensation and rectification corresponds to the procedures used in conventional UT inspections.

5.5 MATCHED FILTER DETECTION LOGIC

With the objective of increasing the amplitude of responses from IGSCC's with respect to other reflectors, a matched filter may be inserted between the DAC compensation and the rectification functions in the detection logic. As shown in Figure 10, the "noise" between the two "crack" signals is reduced by comparison to the conventional logic shown in Figure 9. To be consistent with the DAC calibration, the overall gain of the matched filter is set such that the calibration SDH's provide a 100% DAC response when using the matched

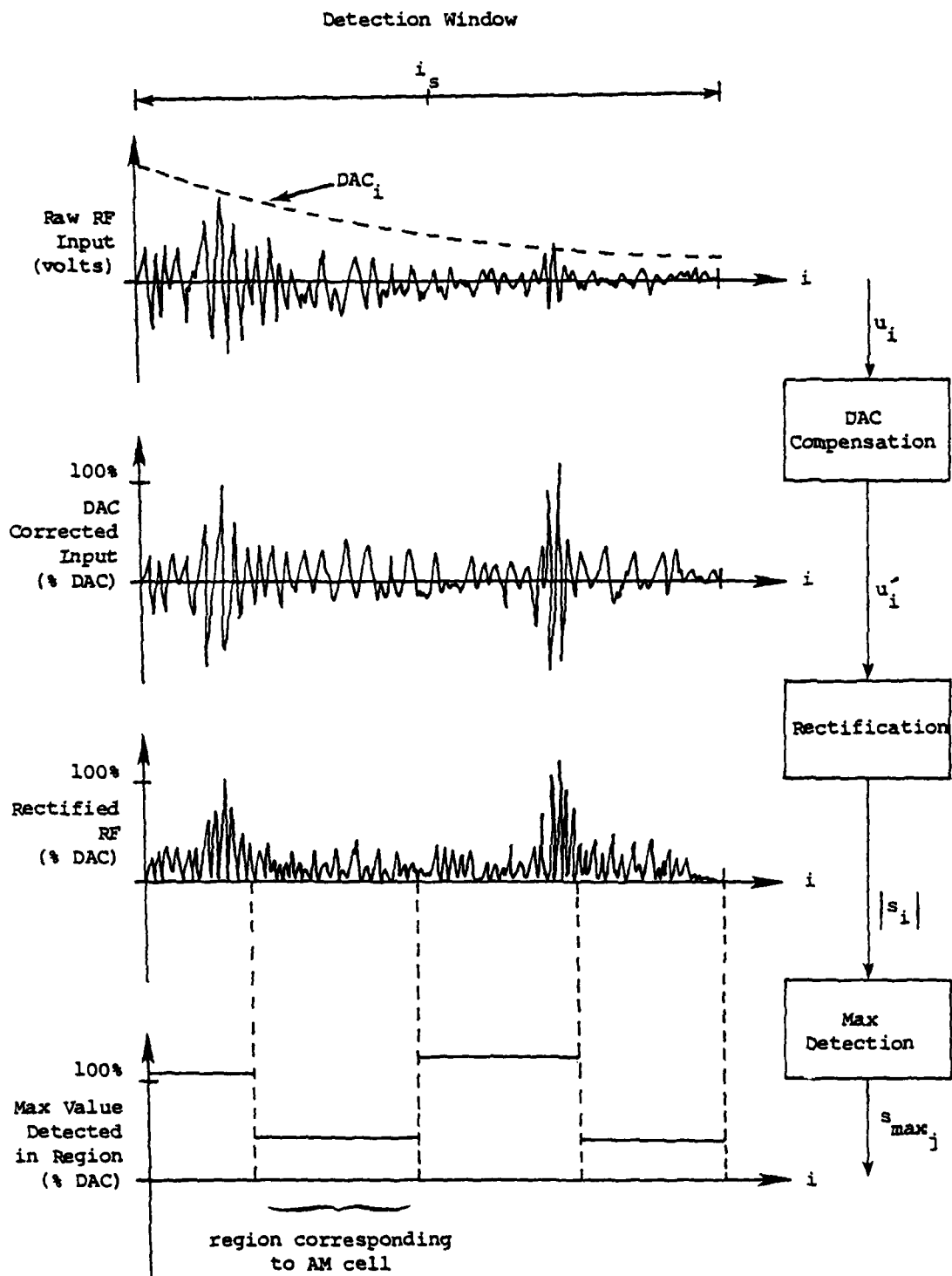


FIGURE 9: CONVENTIONAL DETECTION LOGIC

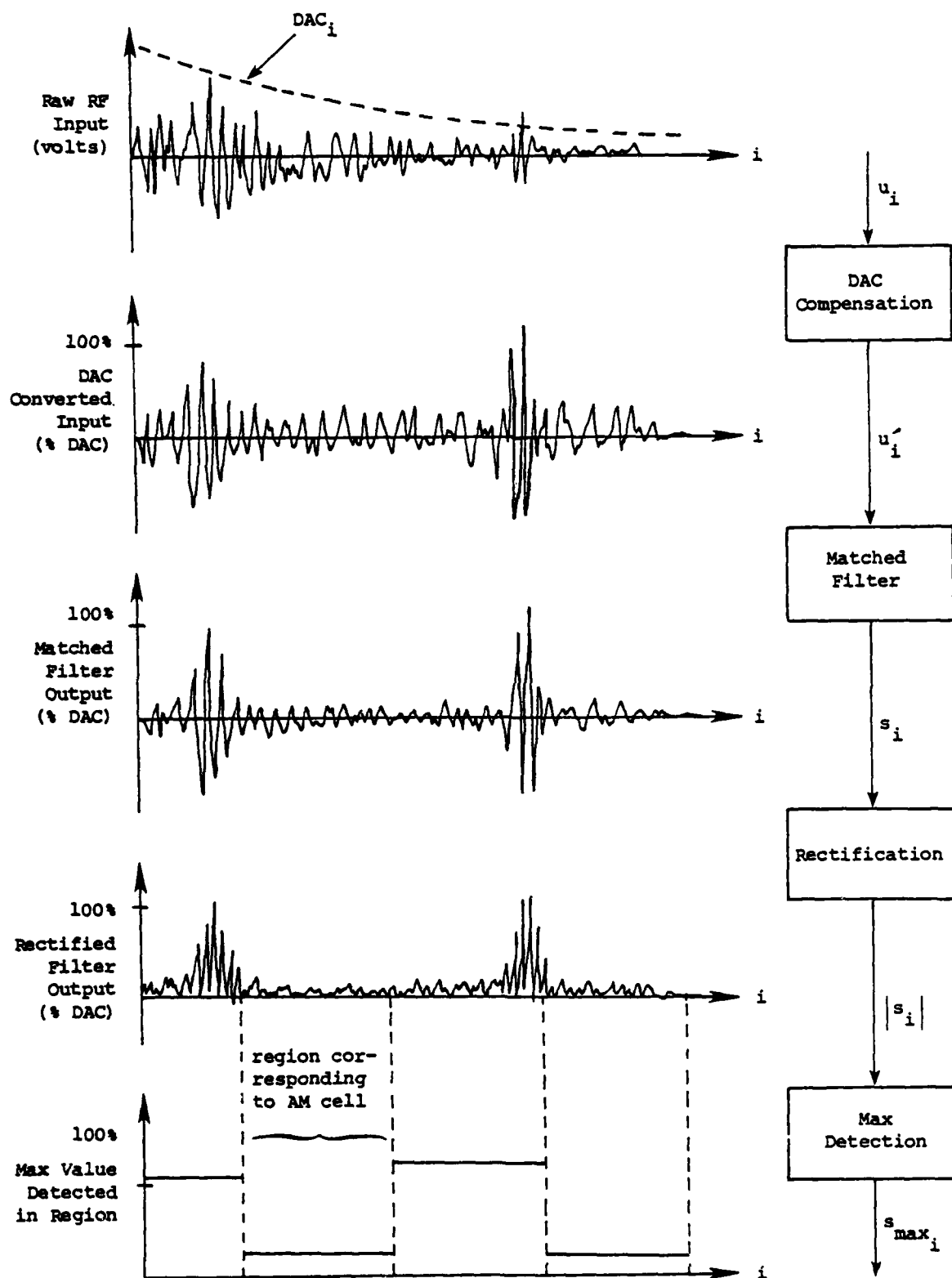


FIGURE 10: MATCHED FILTER DETECTION LOGIC

filter detector as well as when using the conventional detector. For small IGSCC's, however, the responses from the matched filter detector are expected to be greater than responses from the conventional detector, thereby increasing the probability of detecting small cracks with the matched filter.

6. DETECTION ASSOCIATION PROCESS (DAP)

Upon completion of the Detection Scan on one side of the weld, the scanner pauses and the Detection Association Process compiles the results. The two-dimensional Anomaly Map is reduced to an Anomaly List (AL) of reflectors to be further analyzed by the Characterization Scan (CS). Adjacent indications on the map grid are assumed to have resulted from the same reflector and are clustered together. The location of the reflector is taken to be the centroid of the indications. A one-cell indication with no adjacent indications is assumed to be a potential defect and is entered into the AL.

Finally, to minimize scanner travel, the DAP computes the sequence in which the Characterization Scan will treat the reflectors in the AL.

7. CHARACTERIZATION SCAN (CS)

In the Characterization Scan the scanner returns to each reflector in the Anomaly List, locates the reflector more precisely, classifies it as an IGSCC or otherwise, and, if the reflector is a crack, estimates the length and depth.

7.1 REFLECTOR LOCATION

To begin the examination of a reflector, the scanner is positioned (using Equation 3) so as to place the 1-1/2 V intercept at the center of the reflector as estimated by the DAP. The transducer is then dithered in both the axial and circumferential directions until the amplitude of the matched filter output is maximized, thus placing the defect in the center of the transducer main beam. From this transducer location, the ray trace algorithms (Equations 5 and 6) are used to obtain a more accurate determination of the reflector location.

7.2 REFLECTOR CLASSIFICATION

With the transducer at this peaked-up point, 25 UT shots are averaged for a composite waveform. The composite waveform is parameterized and the parameters are input to an Adaptive Learning Network (ALN) classifier which discriminates IGSCC's from other reflector types. Thus, the crack detection is a two-step logic wherein two conditions -- matched filter threshold crossing and ALN

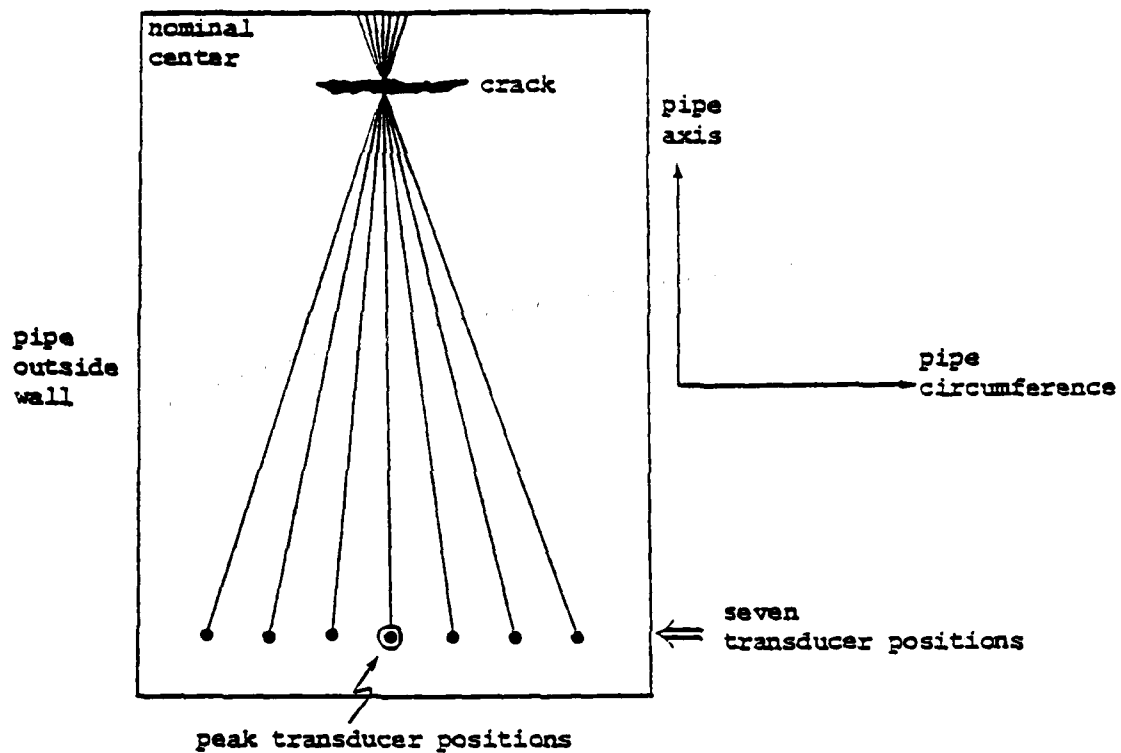
classifier routine -- must be met to issue a crack call. The crack/no-crack classification is recorded in the AL.

7.3 CRACK SIZING

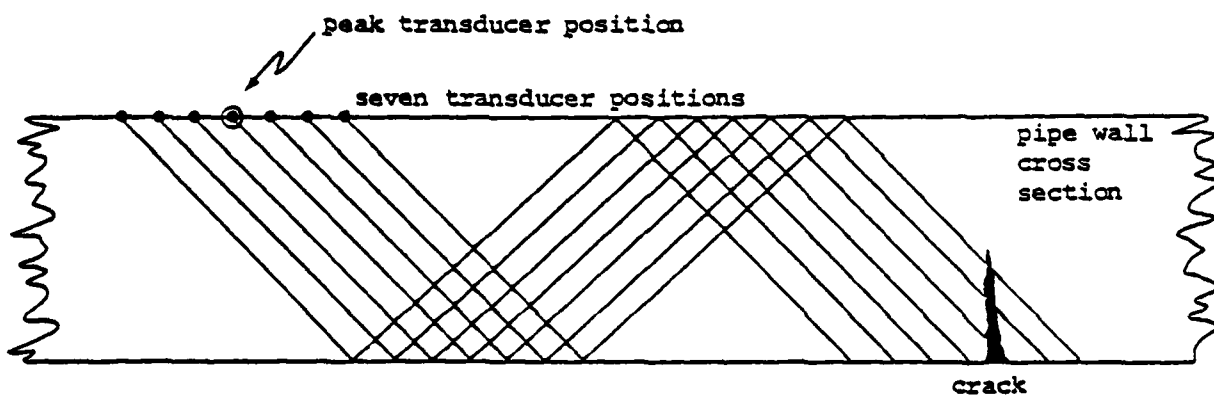
If the reflector is a non-crack, the CS proceeds to the next reflector in the AL. If the reflector is a crack, the crack is sized.

As a first step in sizing the cracks, the scanner moves the transducer circumferentially until the magnitude of the matched filter output is reduced by a factor of 2 (i.e., 3 dB). At each circumferential point, the axial position is dithered to insure that the maximum response for that circumferential position is obtained. The 3 dB points are recorded for both sides of the crack. If the circumferential distance between the 3 dB width is greater than twice the 3 dB width of the transducer, it is assumed that the crack is longer than the width of the beam and that the transducer cannot "see" the whole crack from a single position. In this case, the crack length estimation is based upon the separation of the 3 dB points.

For shorter defects, which can be wholly encompassed within the transducer beam, the length is estimated using ALN's. As shown in Figure 11a, a series of seven UT shots are taken at a constant axial position but with varying circumferential positions and skew angles. Three shots are taken at equal intervals on each side of the peak location, and the transducer is skewed at each location such that the beam center line passes through the nominal crack center. Ripple parameters of the seven power spectra are then computed and input to an ALN which produces a length estimate.



a) For Estimating Short Crack Lengths



b) For Estimating Crack Depths

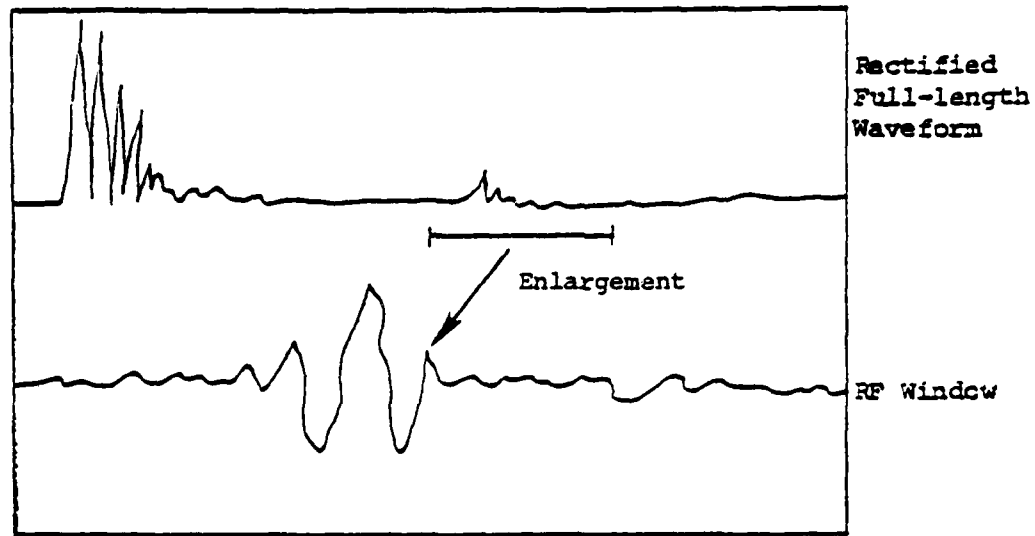
FIGURE 11: TRANSDUCER LOCATIONS FOR COLLECTING UT WAVEFORMS FOR SIZING CRACKS

The procedure for estimating crack depth via an ALN is similar, except tht the transducer is incremented axially as shown in Figure 11b. Because of the fixed transducer shoe geometry, no pitch rotation of the transducer is performed.

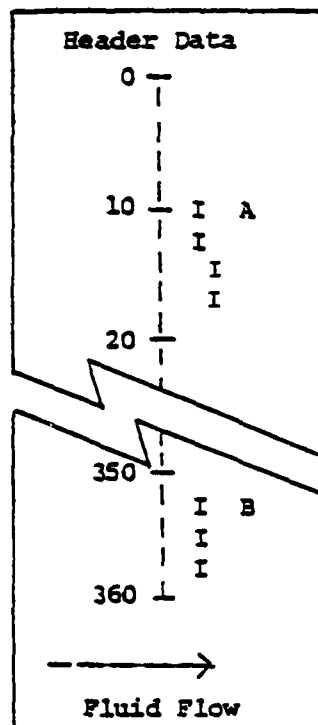
8. DISPLAYS AND OUTPUTS

During the scanning operations (TS, DS, and CS) the composite (i.e., averaged) waveforms are displayed on the oscilloscope as shown in Figure 12a. The rectified waveform, beginning at the metal entry point and extending out to a distance specified by the operator, is shown on the top trace. The window upon which the ALN 4000 is operating is displayed in RF form on the lower trace, with a bar under the upper trace indicating the region being displayed.

At the end of the inspection, a map of those anomalies which were classified as cracks is printed out on the miniprinter as shown in Figure 12b. A designation letter is printed out next to each crack, and the corresponding parameters of the crack are listed below the map.



a) Oscilloscope Display of UT Waveforms



Crack Parameters:

Crack A
 x loc 11 deg
 y loc .19 in.
 length 150 mil
 depth 47 mil

b) Miniprinter Crack Map

FIGURE 12: PIPE SCANNER DISPLAYS AND OUTPUTS

9. CALIBRATION CHECK

Upon completion of the inspection, the inspector verifies that the sensitivity of the ultrasonic instrumentation has not varied appreciably during the inspection process. He places the transducer on the SDH calibration block and obtains a peak response at the four positions used to calibrate the DAC curve. The ALN 4000 detects the peak amplitudes and compares them to the amplitudes obtained during the original calibration. The results must agree within an average of 5% and no point may disagree by more than 10% to determine that the sensitivity remained sufficiently constant.

ATTENDEES AND DISTRIBUTION LIST

Prof. Laszlo Adler
Ohio State University
Dept of Welding Engineering
190 West 19th Avenue
Columbus, OH 43210

Dr. Philip Adler
Hd, Metals Science
Laboratory
Gruman Aerospace
Bethpage, NY 11714

Mr. Melvin Andrasco
NISC 369
Naval Intelligence Support
Center
4301 Suitland Road
Washington, DC 20390

Dr. Om P. Arora
Code 2811
DTNSRDC
Annapolis, MD 21402

Dr. N.K. Batra
Naval Research Laboratory
Code 5834
Washington, D.C. 20375

Mr. J.R. Belt
Code 28
DTNSRDC
Annapolis, MD 21402

Mr. A.S. Birks
Battelle Pacific Northwest
Laboratories
NDT Section
P.O. Box 999
Richland, WA 99352

Dr. Gerry Blessing
National Bureau of
Standards
Ultrasonic Standards Group
Washington, D.C. 20234

Dr. Howard Bomberger
Director, Metallurgy and
Research
RMI Company
P.O. Box 269
1000 Warren Avenue
Niles, Oh 44446

Mr. Thomas J. Bosworth
Boeing Aerospace Company
ORG2-3620
Mail Stop 63-43
P.O. Box 3999
Seattle, WA 98124

Mr. Sanford R. Buxbaum
Johns Hopkins University
Materials Science and
Engineering Dept
Baltimore, MD 21218

Mr. Ivan L. Caplan
David W. Taylor Naval Ship
Research and Development
Center
Annapolis Laboratory
Annapolis, MD 21402

Mr. Steve Cargill
Pratt and Whitney Aircraft
Group-GPD
MS-M30
P.O. Box 2691
West Palm Beach, FL 33402

Mr. J.L. Cavallaro
Code 2830
DTNSRDC
Annapolis, Md 21402

Mr. Henry H. Chaskelis
Naval Research Laboratory
Code 5834
Washington, DC 20375

Dr. James Chestnutt
Rockwell Science Center
1049 Camino Dos Rios
P.O. Box 1085
Thousand Oaks, Ca 91360

Mr. Joe Crisci
Code 282
DTNSRDC
Annapolis, MD 21402

Dr. Vincent A. Del Grosso
Naval Research Laboratory
Code 5831
Washington, D.C. 20375

ATTENDEES AND DISTRIBUTION LIST

Dr. Stan A. David
Metals & Ceramic Division
Oak Ridge National
Laboratory
Oak Ridge, TN 37830

Dr. Glen Edwards
Department of Metallurgical
Engineering
Colorado School of Mines
Golden, Colorado 80401

Mr. Marsh Esler
RMI
Niles, OH 44446

Mr. Gerald Fitzpatrick
Spectron Development
Laboratories, Inc.
3303 Harbor Blvd
(Suite G-3)
Costa Mesa, CA 92626

Prof. Eric S. Furgason
Purdue University
School of Electrical
Engineering
West Lafayette, IN 47907

Mr. Dave Germadnik
RMI Co.
Niles, OH 44446

Mr. Harold Graber
Babcock Wilcox Co.
Nuclear Equipment Division
91 Stirling Ave.
Barberton, OH 44203

Mr. O.D. Graham
Southwest Research
Institute
P.O. Drawer 28510
6220 Culebra Road
San Antonio, TX 78284

Prof. Robert E. Green, Jr.
Johns Hopkins University
Materials Science and
Engineering Dept.
Baltimore, MD 21218

Mr. Alan Greenburg
General Dynamics/
Electric Boat Division
Eastern Point Road
Groton, CT 06340

Mr. R.H. Grills
General Dynamics/
Electric Boat Division
Code 443
Eastern Point Road
Groton, Ct 06340

Mr. John P. Gudas
Code 2814
DTNSRDC
Annapolis, MD 21402

Dr. James Hall
Manager, Henderson
Technical Laboratories
TIMET Division of TMCA
P.O. Box 2128
Henderson, NV 89015

Mr. Amos E. Holt
Babcock and Wilcox Company
Lynchburg Research Center
P.O. Box 1260
Lynchburg, VA 24505

Dr. Duane P. Johnson
Reluxtrol
333 Victory Avenue
South San Francisco, CA
94080

Mr. Francis G. Karchnak
Allis Chalmers
Quality Engineering
Box M-101
York, PA 17405

Mr. James J. Kelly
Office of Naval Technology
MAT 0725
800 N. Quincy St.
Arlington, VA 22217

Mr. James Kennedy
Grumman Aerospace
Plant 26, MS-A01-26
Bethpage, NY 11714

ATTENDEES AND DISTRIBUTION LIST

Mr. Martin Krenzke
Code 1720
DTNSRDC
Bethesda, MD 20084

Dr. Richard Kruger
Los Alamos Scientific
Laboratory
M-5 MS263
Los Alamos, NM 87545

Mr. Joseph La Grotta
Pratt and Whitney Aircraft
Aircraft Road
Middletown, CT 06457

Dr. John Landes
Structural Behavior of
Materials Department
Westinghouse R&D Center
1310 Beulah Road
Pittsburgh, PA 15235

Mr. Richard E. Lewis
Metallurgy and Composites
Laboratory
Lockheed Palo Alto Research
Laboratory
Palo Alto, CA 94304

Mr. W. Lichodziejewski
GARD, Inc./GATX
7449 North Natchez Avenue
Niles, IL 60648

Mr. Frank Lengenfelder
David W. Taylor Naval Ship
Research and Development
Center, Code 2822
Annapolis Laboratory
Annapolis, MD 21402

Dr. Bruce MacDonald
Office of Naval Research
(Code 431)
800 North Quincy Street
Arlington, VA 22217

Prof. Harold Margolin
Department of Metallurgy
Polytechnic Institute of NY
333 Jay Street
Brooklyn, NY 11201X54

Dr. Robert Mehrabian
Chief, Metallurgy Division
Center for Materials
Science
National Bureau of
Standards
Washington, D.C. 20234

Dr. Anthony N. Mucciardi
Adaptronics, Inc.
1750 Old Meadow Road
McLean, VA 22102

Prof. K.N. Mukherjee
Department of Metallurgy,
Mechanics and Material
Science
Michigan State University
East Lansing MI 48827

Prof. P.S. Ong
University of Houston
Dept of Electrical
Engineering
Houston, TX 77004

Dr. Jon L. Opsal
Lawrence Livermore
Laboratory
R&D Group, NDE Section
University of California
P.O. Box 808
Livermore, CA 94550

Dr. Vicki E. Panhuse
AiResearch Manufacturing
Co. of Arizona
M.S. 93-393/503-4Y)
111 South 34th Street
P.O. Box 5217
Phoenix, AZ 85010

Dr. Yoh-Han Pao
Case Western Reserve
University
Electrical Engineering
Dept.
Cleveland, OH 44106

ATTENDEES AND DISTRIBUTION LIST

Mr. Greg Poe
Lawrence Livermore
Laboratory
R&D Group, NDE Section
University of California
P.O. Box 808
Livermore, CA 94550

Dr. Bhakta B. Rath
Naval Research Laboratory
Code 6320
Washington, D. C. 20375

Mr. David Roller
Drexel University Dept of
Mechanical Engineering
32nd and Chestnut Streets
Philadelphia, PA 19104

Prof. Kamel Salama
University of Houston
Dept of Mechanical
Engineering
Houston, TX 77004

Dr. Edward J. Seppi
Corporate Research
Varian
611 Hansen Way
Palo Alto, CA 94303

Prof. Steven Serabian
University of Lowell
Mechanical Engineering Dept
Lowell, MA 01854

Dr. Ramesh Shankar
Tetra Tech, Inc.
1911 North Fort Meyer Drive
Suite 601
Arlington, VA 22209

Dr. A.I. Schindler
Code 6300
Naval Research Laboratory
Washington, D.C. 20375

Prof. Edgar A. Starke
Fracture and Fatigue
Research Laboratory
Georgia Institute of
Technology
Atlanta, GA 30332

Dr. Ronald Strong
Los Alamos Scientific
Laboratory
Group M-5, Mail Stop 912
P.O. Box 1663
Los Alamos, NM 87545

Prof. Robert L. Thomas
Wayne State University
Dept. of Physics
Detroit, MI 48202

Dr. Bernie R. Tittmann
Rockwell International
Science Center
Earth and Planetary
Sciences Group
1049 Camino Dos Rios
P.O. Box 1085
Thousand Oaks, CA 91360

Dr. H.H. Vanderveldt
SEA 05R15
Naval Sea Systems Command
Washington, D.C. 20362

Mr. G.A. Wacker
Code 281
DTNSRDC
Annapolis, MD 21402

Dr. R.M. Waterstrat
American Dental Association
Health Foundation
Research Unit
National Bureau of Standard
Washington, D.C. 20234

Mr. J.K. White
Westinghouse Electric
Corporation
Research and Development
Center
(801-3)
1310 Beulah Road
Pittsburgh, PA 15235

ATTENDEES AND DISTRIBUTION LIST

Dr. Charles R. Whitsett
Solid State Sciences
Department
McDonnell Douglas Research
Laboratories
St. Louis, MO 63166

Prof. James C. Williams
Department of Metallurgy &
Material Science
Carnegie-Mellon University
Pittsburgh, PA 15213

Dr. Richard S. Williams
United Technologies
Research Center
MS86 Acoustic NDE Group
Silver Lane
East Hartford, CT 06108

